New Approaches to Gyroscopic Lasers

A THESIS
SUBMITTED IN PARTIAL FULFILMENT
OF
THE REQUIREMENTS FOR THE DEGREE OF
PHD IN PHYSICS
IN THE
UNIVERSITY OF CANTERBURY

by

Nishanthan Rabeendran

2013

Abstract

This thesis presents a study of two aspects of ring laser gyroscopes: Correction of systematic errors due to optical backscatter, and development of solid-state ring laser gyroscopes.

Backscatter at the optical surfaces of ring laser gyroscopes causes systematic measurement errors. These errors were modelled and corrected for in large ring lasers. The model included backscattering, hole burning and dispersion in the gain medium. The model predictions were used in conjunction with measurements of the intensity modulation of each beam and the phase difference between these modulation to correct the measured Sagnac frequency of the large ring lasers, PR-1 and G-0. Dramatic improvements in the sensitivity of both lasers were achieved.

Most current laser gyroscopes use He-Ne plasma as the gain medium. This makes the devices fragile, the plasma creates UV light that degrades the cavity mirrors and the gas itself degrades over time. As a alternative, solid state materials might be used as the gain medium for the gyroscope. Both neodymium doped and erbium ytterbium co-doped phosphate glass lasers were constructed. Initially linear cavity designs were constructed to test the suitability of the gain media. Both laser systems employed longitudinal laser diode pumping. Thirty six perimeter ring lasers were then developed using both gain media. In both cases successful rotation sensing was achieved on a turntable which provided external rotation. For rotation rates between 0.1 and 0.85 rad/s, the gyroscope built using Er^{3+}-Yb^{3+} and Nd^{3+} phosphate glass are superior to Nd^{3+}:YAG (the only other material known to have been used in a continuous wave solid state gyroscope). This improvement is due to the use of thin heavily doped gain medium, which decreases the detrimental effect caused by gain gratings.

Acknowledgement

Foremost, I would like to express my sincere gratitude to my supervisors: Dr. Bob Hurst, and Assoc Prof. Jon-Paul Wells. I had a wonderful support through Bobs continuous guidance in all aspects of this thesis, and I really appreciate his willingness to share depth of knowledge and experience in laser physics. Assoc Prof. Jon-Paul Wells, also has shown a great support by continuously pushing me to my full potentials, and not taking my 'maybe','but' or 'no' for an answer. He's been a great help in writing up of this thesis.

Besides my supervisor, I would like to thank the other staff in the Department of Physics. Prof. Roger Reeves of University of Canterbury, for various useful discussions and tips on mounting the pump laser on a translation stage; also, Prof. Ulli Schreiber of Technical University of Munich, Germany, for proving a unique opportunity to use the G-gross ring laser and attend courses while I was there. My sincere thanks also go to Mr. Robert Thirkettle, for building the turntable and many mechanical structures needed for this project; Mr. Clive Rowe, for useful discussions on this project, and for being so enthusiastic about physics. I enjoyed hearing all his stories about building the C-I ring laser; Mr. Graeme MacDonald, for the fast and effective support with many electronic requirements for this project, especially for his intricate wiring for the ring to run on the turntable; Mr. Matt Pannell, for his work on the electronics to control the stepper motor used for the turntable; Mrs. Stefanie Daurer, for arranging the courses in Germany, and for the great help with the translation.

Lastly, I offer my regards to all my friends and family who supported me in any respect during the completion of the project; Dr. Richard Graham, for introducing to me to the amazing world of open source software such as Gimp, Inkscape and Latex, which I have used in writing my thesis; Dr. Ewan Orr, who has been always encouraging and supportive throughout the thesis, for providing tips and tricks to manage large quantity of data generated for this thesis; Dawoon who has been a lovely supportive wife, understanding and caring even when my Ph.D. keep me away from doing more things in the weekends and nights; Peter and Micheal, who have been great friends for more than a decade, for making the down periods of the thesis more bearable. Cheers to you all.

Contents

List of Figures

List of Tables

Chapter 1

Ring Laser Gyroscopes

Ring laser gyroscopes (RLGs) are vital navigation aids for many aircraft, ships and space craft. Larger gyroscopes are employed in geodesy to measure polar motion [2], tidal motion, the annual and Chandler wobbles [9], as well as co-seismic rotation caused by earthquakes [10]. The requirements for a rotation sensor are to have high angular resolution, stable input axis, insensitivity to acceleration, linear behaviour with varied rotations, long lifetime, low weight, and low cost [11]. Prior to the development of RLGs , these requirements were needed to be met by mechanical gyroscopes, which are often still in use. However for many applications these have been replaced due to their fundamental limitations. Laser gyroscopes are insensitive to acceleration, have a linear response over 6 orders of magnitude and have fewer moving parts. Large laser gyroscopes used in geodesy do not contain any moving parts at all.

RLGs use the Sagnac effect to measure rotation. This effect was demonstrated in 1913 by George Sagnac [12]. A Sagnac interferometer splits input light into two beams that propagate in opposite directions around a common polygonal path before recombination. When the whole apparatus is rotated, a fringe displacement is observed that is proportional to rotation rate. The phase shift ($\Delta\phi$) between the light beams is given by:

$$\Delta\phi = \frac{8\pi\widehat{\Omega}.\widehat{A}}{\lambda c} \tag{1.1}$$

where A is the area enclosed by the polygonal paths taken by both beams, λ is the wavelength of light, $\widehat{\Omega}$ is the rotation rate experienced perpendicular to the enclosed area A and c is the speed of light.

If a ring laser is constructed, with beams travelling in opposite directions in the cavity, the same Sagnac effect causes there to be an optical frequency difference between the beams when the device is rotated. The frequency difference is termed the Sagnac frequency

(υ) and is given by:

$$\upsilon = \frac{4\widehat{\Omega}.\widehat{A}}{\lambda P} \tag{1.2}$$

where P is the perimeter of the cavity. The first laser-gyroscope employing the Sagnac effect was demonstrated in 1963 by Macek and Davis [13]. This thesis investigates two types of laser gyroscope using the same effect: solid state ring laser gyroscopes (SSRL) and gas ring laser gyroscopes (GRL).

This thesis has two main objectives: (1) to explore novel materials for solid state laser gyroscopes, which have applications in navigation, (2) to improve the performance of large gas gyroscopes by correcting for backscatter effects which cause read out errors in the measurement quantity. the

1.1 Motivation

1.1.1 Solid State Laser Gyroscopes

He-Ne gas lasers have been the most commonly used in laser gyroscopes. This system is extensively in use and is the standard technology in many modern vehicles such as the Boeing 747/767 and the Airbus 310. In an all solid state gyroscope, the He-Ne gain medium is replaced by a solid state material, consequently removing the need for a discharge tube. Helium, being a small molecule, has a tendency to diffuse out of the tube, decreasing the life span of the gyroscope. In a large laser gyroscope such as the 834 m^2 UG-2 at the University of Canterbury the gas needs to be replaced every few months due to hydrogen outgassing from the stainless steel tubes which enclose the beam path [14]. In addition, removing the plasma eliminates UV light from the cavity which damages the dielectric mirrors [15], again this increases the gyroscopes lifetime. In a solid state ring laser pumped by laser diodes the operational lifetime is limited only by the lifetime of the pump laser. the

One of the goals of this thesis is to build and explore various solid state materials as gain media in laser gyroscopes. The project focuses on Nd^{3+}:phosphate glass and Er^{3+}-Yb^{3+}: phosphate glass, because only Nd^{3+}: YAG has been demonstrated as a CW laser gyroscope. Nd^{3+}: phosphate glass is a high gain 4-level laser system which provides a platform to develop the techniques to build an initial solid state gyroscope for the project. On the other hand Er^{3+}-Yb^{3+} co-doped phosphate glass is less forgiving to build due to the lower gain quasi- 3-level system. It provides a long lifetime for the upper lasing level.

This delays the creation of the gain grating which would otherwise hinder the performance of such a gyroscope. Also, layers of the gain grating are formed half a wavelength[1] apart along the crystal, so increasing the wavelength decreases number of layers of grating per unit length. By exploring different types of materials, this project takes a step closer to answering the ultimate question "What is the best material to build a solid state laser gyroscope?"

1.1.2 Large Gas Ring Lasers

Large ring laser gyroscopes have remarkable sensitivity. For example the Gross Ring (G) currently the most stable laser gyroscope in the world has an ability to measure the Earth's rotation with relative precision of 1 part 10^9 [16]. Even with this superb short term performance the G-ring does not compete with the radio-astronomical technique of VLBI (Very Long Base Interferometry), which uses distant galactic objects such as quasars to measure the rotation of the Earth and thus define the international celestial reference frame (ICRF) which has a precision of 1 part 10^{10}. If ring lasers were able to measure Earth rotation with sensitivity comparable to VLBI it could provide continuous data avoiding the delays associated with VLBI. The time varying backscatter coupling between counter propagating laser beams is the major instability which prevents G from reaching the required level of sensitivity. This thesis aims to develop techniques to correct for backscatter coupling which will improve the ring's sensitivity to rotation and therefore be comparable to VLBI. Since backscatter coupling is present in all laser gyroscopes the correction techniques developed in this thesis have wide application.

1.2 Thesis Layout

Chapter 1 presents the motivation for the thesis.

Chapter 2 introduces different types of laser gyroscopes providing the background context for this thesis. Then it is narrowed down to active gas gyroscopes and different measurement errors are discussed. Large ring lasers and their operational parameters are presented to lay the foundations for chapter 3. This is followed by a review of solid state laser gyroscopes, which is background to Chapters 4 and 5.

Chapter 3 briefly describes Adler pulling followed by the formulation of a complete

[1]The wavelength emitted by Er^{3+}-Yb^{3+} and Nd^{3+} lasers are 1.5 μm and 1 μm.

model of backscattering described by three coupled differential equations. The equations include the effects of backscattering from the cavity mirrors, dispersion, self and cross saturation of the gain medium. These equations are solved approximately first. Then a numerical solution is presented and compared with the result obtained by approximation. Successful correction for backscattering for the ring lasers PR-1 and G-0 is presented. Finally, the chapter describes an experiment to back-inject light into a ring laser.

Chapter 4 is devoted to the design, construction, and performance of a Nd^{3+}: phosphate ring laser. The chapter begins by introducing the properties and suitability of Nd^{3+}: phosphate as a laser medium while briefly comparing it with Nd^{3+}: YAG which is currently the most common solid state laser medium. Next the construction of a linear cavity is presented: the cavity construction, pumping scheme, polarisation stability, traverse modes and saturation of the gain medium are discussed. This is followed by an L-cavity, its stability, alignment and performance. Finally, an astigmatism correction for the pump laser is shown, followed by alignment and description of the first ring gyroscope built. Its rotation sensing behaviour and a description of various modulation regimes observed from the ring are presented and discussed.

Chapter 5 presents the construction and operation of an Er^{3+}-Yb^{3+}: phosphate solid state ring laser. The chapter starts with a broad description of erbium-ytterbium lasers. It then focuses specifically on Er^{3+}-Yb^{3+}: phosphate lasers. Spectroscopy of the gain medium was used to calculate the available gain of the lasing medium. As with the Nd laser, a linear and L-cavity has been developed. Relaxation oscillations caused by the pump laser are also discussed. Scattering losses are determined. The development of the laser gyroscope is then presented and an evaluation of its rotation sensing ability is given.

Chapter 6 presents the conclusion, discussion and future work.

Chapter 2

Laser Gyroscope Fundamentals

Rotation (relative to an inertial frame) can be measured by using the propagation of light. In a rotating frame, the travel time of light around a closed path will be different in two directions. This phenomenon was first observed by and named after George Sagnac in 1913, as a shift in a stationary fringe pattern produced by an interferometer, proportional to the rotation rate of a turntable [12].

Michelson and Gale (1925) built a 613 m by 339 m interferometer and used the Sagnac effect to measure the Earth's rotation [17]. They used a carbon arc lamp as a light source and split the light into oppositely directed beams travelling around a closed path. They recombined the beams to produce a constant phase shift from Earth rotation of 0.23 $\pm$ 0.005 fringes. This was a massive technological achievement at that time.

A simple derivation of the Sagnac effect is illustrated in Figure 2.1. The two beams shown are travelling in a clockwise (blue) and anticlockwise (red) direction. When there is no rotation both beams arrive at the beam combiner (B_0) at the same time, with the same distance travelled by both beams. However, when the whole reference frame rotates (anti-clockwise in Figure 2.1), the clockwise beam reaches the beam splitter (B_1) earlier, while the anticlockwise beam reaches the beam splitter (B_2) later than it would if there were no rotation. The times taken by the clockwise and anti-clockwise beams are given by:

$$t_+ = \frac{2\pi r - r\widehat{\Omega}t_+}{c} \qquad t_- = \frac{2\pi r + r\widehat{\Omega}t_-}{c} \tag{2.1}$$

where r is the radius of the circle, $\widehat{\Omega}$ is the rotation rate and c is the speed of light. The difference in arrival time between the beams (Δt) is given by:

$$\Delta t = t_- - t_+ = \frac{4\pi r^2\widehat{\Omega}}{c^2(1-\frac{\widehat{\Omega}^2 r^2}{c^2})} \approx \frac{4\pi r^2\widehat{\Omega}}{c^2} = \frac{4\widehat{A}\widehat{\Omega}}{c^2} \tag{2.2}$$

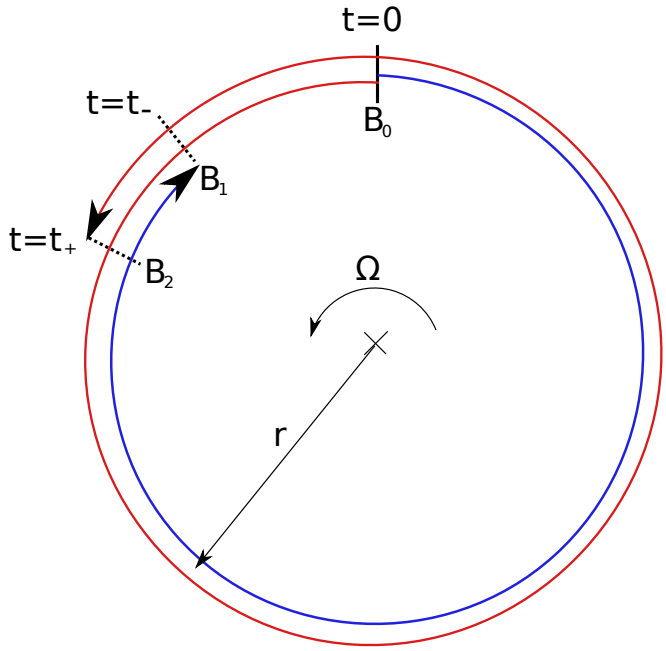

Figure 2.1: Diagram of the Sagnac effect. The red arrow represents a counter-clockwise beam and the blue arrow an anti-clockwise beam. The rotation rate is $\widehat{\Omega}$. The beam combiner position is shifted from B_0 to B_1, B_2 due to rotation. Diagram modified from [1]

where $\frac{\widehat{\Omega}^2 r^2}{c^2}$ is approximately equal to zero since $\widehat{\Omega}^2 r^2 << c^2$ and $A = \pi r^2$. The phase difference ($\Delta\phi$) between the beams is given by:

$$\Delta\phi = \omega\Delta t = \frac{2\pi c}{\lambda}\Delta t = \frac{8\pi\widehat{A}\widehat{\Omega}}{\lambda c} \tag{2.3}$$

where ω is the angular frequency and $\lambda = \frac{2\pi c}{\widehat{\Omega}}$ is the wavelength of the light. Thus the phase shift $\Delta\phi$ is proportional to the rotation rate $\widehat{\Omega}$. From equation 2.4, the phase difference increases with area, which explains the need for Michelson to build a large interferometer to measure the Earth's rotation. In the laser era it is also possible to build laser based passive gyroscopes known as fibre optic gyroscopes. These use coils of optical fibre to increase the area enclosed by the beams. Figure 2.2 shows an example of this kind of device. Fibre optic gyroscopes were first built in 1976 by Vali and Shorthill [18]. Even though the first fibre gyroscope was not sensitive enough to measure the Earth's rotation, with further development over the years this type of gyroscope has evolved to easily measure Earth's rotation [19]. The phase shift ($\Delta\phi$) in a fibre gyroscope is obtained by modifying equation 2.4 to [19]:

$$\Delta\phi = \frac{2\pi LD\widehat{\Omega}}{\lambda c} \tag{2.4}$$

where L is the length of the fibre and D is the diameter of the coil. As the length and the diameter of the coil increases, the sensitivity increases. The advantage of the fibre optic

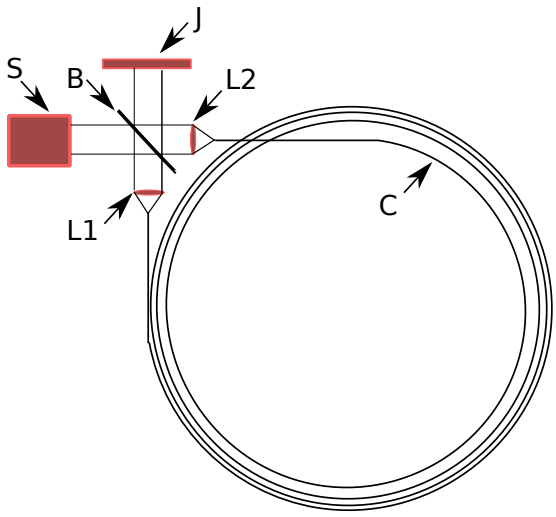

Figure 2.2: Diagram of a fibre optic gyroscope (FOG). L1 and L2 are lenses that are required to focus the light into the fibre. S is the laser light source (usually a semiconductor laser diode), B is the beam splitter, J is the detector where the fringe pattern is observed and C is the coil of optical fibre.

gyroscope is that it can be made small by having tightly wound coils; they are robust, have low power consumption and can be transported easily. This is ideal for monitoring buildings for example.

2.1 Active Laser Gyroscopes

Active laser gyroscopes have the advantage of measuring a frequency difference as opposed to a phase shift. The improvement in rotation sensitivity can be seen by comparing equations 1.1 and 1.2. The inclusion of speed of light c in the denominator of equation 1.1 decreases the response to rotation. Also, frequency difference can be measured[1] with greater precision than the phase shift. An active laser gyroscope was demonstrated by Marcek and Davis in 1963 [13]. Figure 2.3 shows a schematic diagram of an active laser gyroscope which works using the same principle as Marcek and Davis' device. The device is composed of four cavity mirrors; M1, M2, M3 and M4. The cavity supports an integer number of wavelengths. Unlike a linear laser cavity where standing waves are formed, in a ring cavity two travelling waves are formed which are ideally independent of each other. For a non-rotating cavity the wavelength of both beams is the same. However under the

[1]The counter-propagating beams are combine to achieve a beat signal. Beat signal is proportional to the rotation rate, which can be more precisely measured.

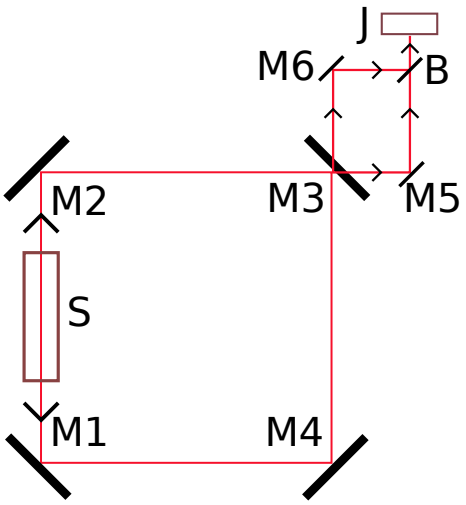

Figure 2.3: Diagram of an active laser gyroscope. M1, M2, M3 and M4 are laser cavity mirrors. M5 and M6 are planar fold mirrors, B is a beam-splitter, S is the gain medium and J is a detector.

influence of a rotation, the wavelength of the beams becomes either red or blue shifted in order to fit into the cavity. Once the beams are combined at (B), a beat of the two superimposed waves is measured by the detector (J). The beat frequency (υ) between the two beams is given by :

$$\upsilon = \frac{4\widehat{\Omega}.\widehat{A}}{\lambda P} \tag{2.5}$$

where P is the perimeter of the cavity. The term $\frac{4.\widehat{A}}{\lambda P}$=$S$ is called the scale factor. Significant efforts have been taken in ring laser construction to maintain a stable scale factor. This formula has been proven both semi classically [20] and using general relativity [21]. Using this relationship active gyroscopes have become versatile devices for the measurement of physical rotations. Generally, as the area of the device increases the sensitivity to rotation also increases. This has led to a wide variety of devices with different sizes. The size of a given gyroscope varies depending on the application as the sensitivity increases with perimeter. Typically perimeters of up to 60 cm are used in advanced navigational systems, while a few cm is all that is required for missile guidance systems [11]. Very large ring lasers have perimeters up to 121 m [14]. Many commercial aircraft have gyroscopes with perimeter close to 30 cm. The properties of these gyroscopes are extensively reviewed by Chow et al. [21], Wilkinson [1] and Aronowitz [22]. More recently, the geodetic capabilities of large laser gyroscopes have been reviewed by Schreiber and Wells [7].

Solid state ring lasers (SSRLs) and gas ring lasers (GRLs) are active gyroscopes and are the focus of this thesis. The GRL is commercially available and is widely used, while

SSRL are not commercially available. In this section GRLs will be covered first, while SSRLs will be dealt with at the end of the chapter.

All GRLs are built using He-Ne gas to produce the counter propagating laser beams. Gain for both of the beams is provided by the He-Ne plasma discharge. Figure 2.4 shows the excitation processes involved in any 632.8 nm He-Ne laser. The electrons present in the plasma collide with the helium atoms causing excitation into the metastable $1s2s$ state. The $5s$ energy level of neon is close to the metastable state of the excited helium atom. Through non-radiative inelastic collision energy is transferred to the neon $5s$ state. The excited neon $5s$ state has a 6 times longer decay time than the neon $3p$ state. This allows for the required population inversion to build up between these states for lasing to occur. Spontaneous emission causes the neon $3p$ state to decay to neon $3s$ state. The ground state is reached through wall collisions. An example of a navigational GRL is

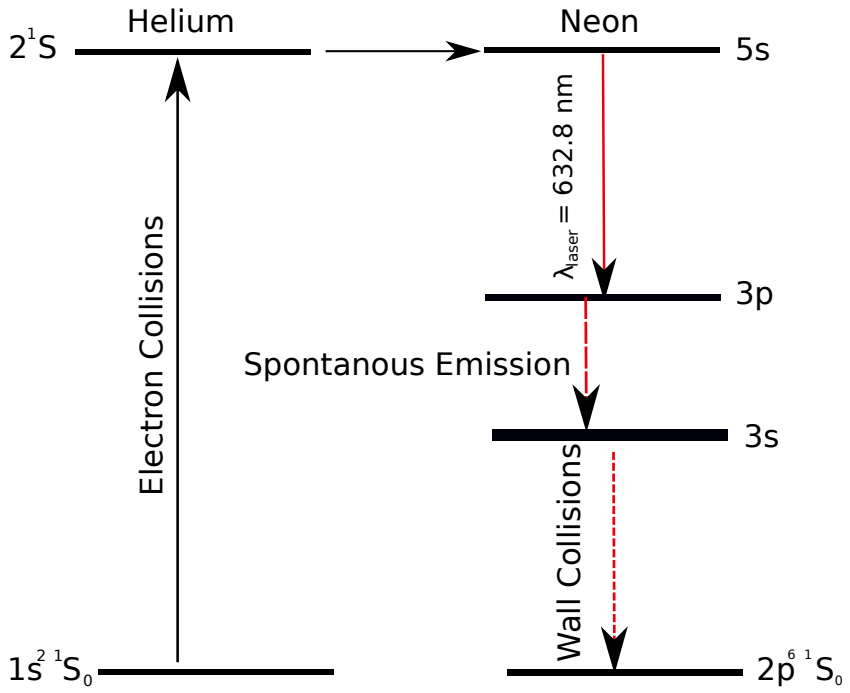

Figure 2.4: Schematic energy level structure of the excitation processes in a He-Ne lasers operating at 632.8 nm.

shown in Figure 2.5. The highlighted area in red between the anode (A) and cathode (C) is to depict the glow of the discharge tube filled with He-Ne gas.

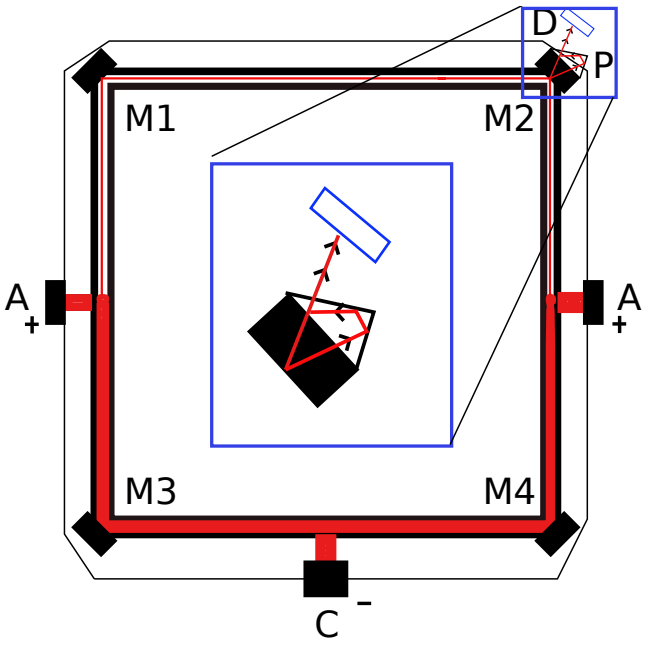

Figure 2.5: Typical navigational He-Ne laser gyroscope. M1, M2, M3 and M4 are cavity mirrors. The He-Ne discharge is between the anodes (A) and the cathode (C). (P) is a prism, where the clockwise and counter clockwise beams are combined. (D) is a photo-detector. Piezos are attached to the cavity mirrors. The cavity is created by hollowing into a low-expansion material such as Zerodur or Cervit.

2.2 Measurement Errors in Active Gyroscopes

An ideal rotation sensor follows equation 2.5, but in reality there are deviations from ideal rotation sensing behaviour. Figure 2.6 shows the errors that can occur in a laser gyroscope. The blue line in the figure is the ideal behaviour and the red line is the deviation caused by the errors involved. Many techniques have been developed to circumvent theses errors.

1. Effect of variation in scale factor

The output of the ring laser when the scale factor (S) changes is shown as the red plot in the first graph in Figure 2.6. This is typically caused by the changes in the geometry of the cavity. To minimise this, many navigational ring gyroscopes are constructed with holes drilled through a low expansion ceramic such as Zerodur or CerVit (Figure 2.5). Piezos are also attached to the cavity mirrors which are servo controlled to the maximum laser intensity or the output from a Fabry-Perot interferometer. By maintaining the maximum power to a single longitudinal mode the laser is stabilised. Alternately, the laser frequency can be monitored with a Fabry-Perot interferometer, with adjustments to

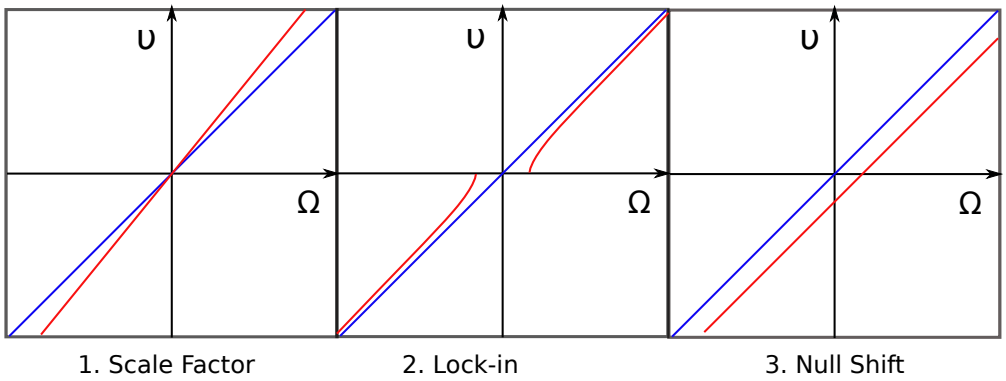

Figure 2.6: Various errors in the ideal relationship described by equation 2.5 in laser gyroscopes. υ is the beat signal and Ω is the rotation rate the ring laser experiences. The blue line is the ideal behaviour and red line is the laser output in the presence of the readout error involved.

the mirrors maintaining a constant perimeter.

Another factor that changes the scale factor is dispersion. The peak in the gain curve pulls the neighbouring modes close together (line pulling [23]). Self saturation and cross saturation (hole burning) of the gain medium also causes variation in the scale factor. These effects will be explained in more detail in Chapter 3.

2. Lock in behaviour in the laser gyroscope

For an ideal ring laser the clockwise and counter clockwise beams need to be independent of each other. However, backscattering of the beams by cavity mirrors causes coupling between the beams. When the coupling becomes large the frequency of both beams becomes degenerate. This is called "lock in". This creates a region where the ring laser is insensitive to rotation (also called the dead band). The dead band is given by the equation below [24]:

$$\Omega_L = \frac{c\lambda^2 r_s}{32\pi A d} \tag{2.6}$$

where Ω_L is the lock in region, c is the speed of light, λ is the wavelengh of the laser, A is the area enclosed by the ring, d is the diameter of the beam and r_s is the backscatter contribution from the cavity mirrors. To minimise the dead band, high reflectivity mirrors have been developed which lower the backscattering contribution r_s. Increasing the area of the ring laser also decreases the dead band.

Another approach that has been successfully developed is dithering of the ring away from the dead band. Mechanical dithering introduces a rotation in the clockwise and an-

ticlockwise directions, moving the measurements away from the dead band. The induced rotation is later removed from the measurements to obtain the actual external rotational signal.

3. Null shift in the Sagnac Frequency

Null shift is mainly caused by the Langmuir flow in the discharge tube. When the discharge is formed, the ions and electrons in the plasma travel towards the anode and cathode. This causes a shift in gain and the dispersion curve for the opposite beam [25]. It adds an extra term to equation 2.5.

To minimise this effect navigational gyroscopes have two anodes. This can be seen in Figure 2.5 where there is two anodes and one cathode. The null shift caused by one side is cancelled by the other side.

2.3 Large Ring Laser Gyroscopes

To increase the sensitivity, gyroscopes were built having a much larger perimeter than navigational lasers. As the factor A/P in equation 2.5 increases, the laser's ability to measure rotation also increases (given all other factors remain the same). A larger size also means that the ring laser is biased away from the dead band by Earth rotation. This led to the construction of C-I the first laser to unlock under Earth rotation. Then a slightly larger device named C-II was built which was a monolithic ring laser [26]. Rather than using glass tubes like C-I, it was built with a Zerodur block which was drilled to accommodate the laser cavity, similar to the navigational gyroscope in Figure 2.5, only much larger. The low expansion property of the material reduces the unwanted scale factor changes. C-II was also placed in an abandoned World War-II bunker in Cashmere, New Zealand. This environment provided a stable location for the ring. Over time, many larger rings were built. Table 2.1 shows the ring lasers that have been built in New Zealand and Germany. The sensor resolution generally improves with size. Due to the high cost of low expansion materials such as Zerodur, all rings expect C-II and G were built using stainless steel. The G-ring in Wettzell, Germany is currently the most sensitive laser gyroscope in the world with the ability to measure the Earth's rotation with a relative precision of 1 part in 10^9 [16]. To achieve this performance, the scale factor needs to be maintained at 1 part in 10^{10} and G is housed in an underground laboratory with thermal variations around 5 mK per day. With a larger scale factor the large rings were able to

Ring Laser	Area (m^2)	Perimeter (m)	Sagnac Frequency (Hz)	Sensor Resolution (prad/s $\sqrt{Hz}$)
C-I	0.748	3.48	76.12	N/A
C-II	1	4	79.4	146.2
PR-1	2.56	6.4	113.5	N/A
GEOsensor	2.56	6.4	102.6	108.1
G-0	12.25	14	288.2	11.6
G	16	16	348.6	12
UG-1	366.83	76.93	1512.8	17.1
UG-2	834.34	121.435	2177.1	7.8

Table 2.1: Summary of some physical parameters of the ring lasers. Most of the data is obtained from review paper [7].

be used to measure small geodetic effects such as polar motion (the Oppolzer modes) [2], tidal motion and the Chandler wobble [9]. These ring lasers also give unique information about co-seismic rotations [10] caused by earthquakes, which are not able to be measured with traditional seismic instruments.

The most sensitive measurement (performed at the time of writing) by the large ring laser is the Chandler wobble, followed by daily polar motion. The Chandler wobble is a free body motion of the earth with period about 430 days, which is independent of external gravitation pull. The amplitude of this wobble is around 4-6 m at the pole. On top of this wobble there a small diurnal periodic oscillation caused by the gravitational pull of the moon and sun. The measurement of polar motion is shown in Figure 2.8. Out of three lasers only G was able to resolve the two components of the polar motion. This is due to the monolithic construction which allows for a long time series to be obtained.

Other effects such as solid Earth tide signals are larger in C-II and UG-1 due to the location in Christchurch, NZ where ocean loading is large.

2.3.1 Operational Specifications for Large Ring Lasers

This section outlines the operational details for the large ring lasers used in Chapter 3 of this thesis.

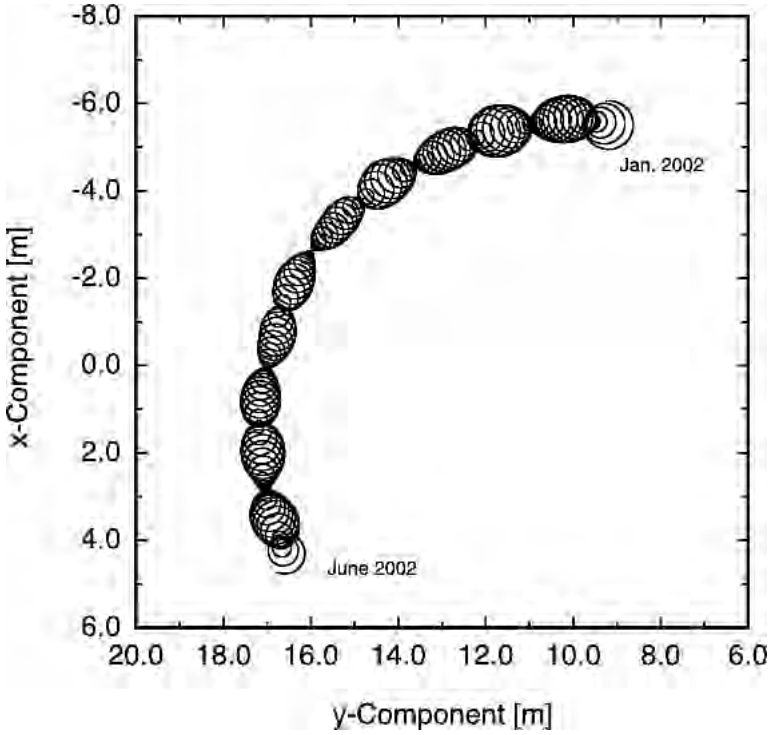

Figure 2.7: Motion of the Earth's rotation axis (at the pole). The large circle is the Chandler wobble. The small circles are motions caused by gravitational pull from the moon and the sun. The figure is obtained from [2].

Single Mode Operation

All of the large ring lasers in Canterbury and Germany use He-Ne gas as a gain medium. In fact, most laser gyroscopes including the navigational gyroscopes use He-Ne gas. The He-Ne gain curve is predominantly inhomogeneously broadened due to Doppler effects and isotope shift between ^{20}Ne and ^{22}Ne. The linewidth of the gain curve is around 1.5 GHz. The homogeneous part of the gain curve is pressure dependent and is given by [27]:

$$\Delta\nu_h = \Delta\nu_r + \Delta\nu_c \approx 12 + 46p \tag{2.7}$$

where $\Delta\nu_h$ is in MHz, $\Delta\nu_r$ is radiative broadening and $\Delta\nu_c$ is the collision broadening and the total pressure is p, given in millibars. In large ring lasers the typical neon pressure is $\sim$0.2 millibar. The total pressure of neon and helium is in the range of 4-10 millibar. This gives a $\Delta\nu_h$ broadening in the range of 196 MHz to 472 MHz. The longitudinal mode spacing for the cavity is given by c/P, where c is speed of light and P is the perimeter of the ring. For the G ring laser the mode spacing is 18.75 MHz. Since $\Delta\nu_h$ is much larger than the mode spacing, when a single mode lases it diminishes the gain for other modes around it. This effect increases as the pressure increases due to increased homogeneous

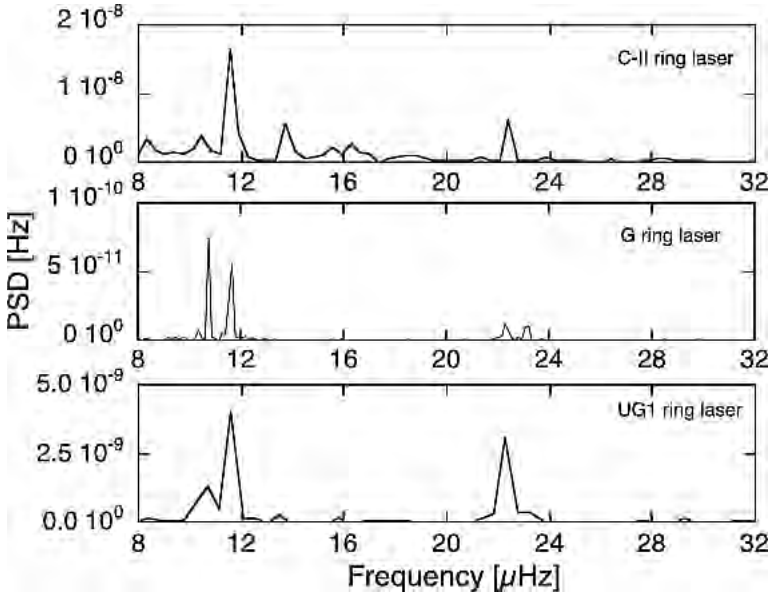

Figure 2.8: Power spectrum of three large ring lasers (C-II, G and UG-1). The two frequencies at 11.606 and 10.758 μHz are due to polar motion. The high frequencies are due to solid Earth tides [2].

broadening. Also, the laser is typically run just above the lasing threshold, so the gain available is just enough for one mode.

Gas Composition

Neon gas is available having two naturally occurring Ne isotopes, ^{22}Ne and ^{20}Ne. The ratio of the two isotopes is 90 % ^{22}Ne and 10 % ^{20}Ne. The overall gain curve is a superposition of two gain curves of the individual isotopes, which are spaced apart by 889 MHz, the mean of the three most precisely reported values mentioned in [28]. Even though it is possible to run the lasers using the naturally occurring isotope ratio, it is better to run them on a 1:1 ratio of isotopes to minimise mode competition between the clockwise and counter clockwise beams [24]. In fact, if only one isotope is used the laser will run unidirectional, as one beam will deplete the gain available for the oppositely travelling beam.

At a 1:1 ratio the lasing position is away from the centre of the gain curve of each isotope. The population of atoms used by the clockwise beam is different than that used by the counter clockwise beam as they interact with different velocity packets due to the Doppler effect.

Measured Parameters

The clockwise and counter-clockwise beams produced by the ring are individually monitored by photo-diodes. Throughout the thesis the term monobeam is used to refer to a single laser beam. This output will have a DC signal contribution with an AC modulation superimposed due to backscatter. The Sagnac frequency is measured by combining the two counter propagating beams using a beam splitter (Figure 2.3) or a prism (Figure 2.5). If the backscattered light from one beam is large enough it will combine with the counter propagating beam, causing it to be modulated at the Sagnac frequency. In this situation it is sufficient to monitor a monobeam alone to obtain the Sagnac frequency.

2.4 Solid State Gyroscopes

Solid state gyroscopes offer an alternative to the He-Ne gas gyroscopes that have been used extensively as navigational and large gyroscopes. The solid state gyroscope still utilises the Sagnac effect, but the gain medium that generates the clock-wise and counter-clockwise beams is a solid state material rather than a gas. This eliminates the need for a discharge tube potentially increasing the robustness of the device. It also removes the high voltage required to ignite and maintain the He-Ne plasma. Additionally, UV light from the plasmas accelerates the degradation of cavity mirrors, so it is beneficial to remove this.

The earliest published account of solid state ring lasers (SSRL) was by Walsh, et al. [29] and Tang, et al. in 1963 [30]. The demonstration of a rotating sensing SSRL was shown in 1974 by Klochan, et al. [31, 32]. A comprehensive review paper covering the development of the SSRL up to 1992 was written by Kravtsov, et al. [33]. Most of the work occurred in the former Soviet Union.

One of the main operational differences between the gas and solid state rings is the formation of a gain grating in the lasing medium which causes additional coupling between the clockwise and counter-clockwise beams. Gratings are formed by the standing wave created by counter propagating beams in the gain medium. A grating reflects a small fraction of one beam back into the other beam, causing coupling between the beams. The gain gratings are formed with a periodicity of half a wavelength along the length of the gain medium. It is preferable to have a thinner gain medium to decease the number of layers of the grating. This does not occur in gas lasers because of thermal motion which averages out the gain grating. Another difference is the presence of mode competition

between the counter propagating beams because of the homogeneous broadening of the laser line. In a gas laser this can be minimised using equal ratio of Ne^{22} and Ne^{20}. To solve this for SSRL, Dotsenko, et al. [3] devised a servo system which varies the losses on each beam to minimise the intensity difference which occurs due to mode competition. Figure 2.9 illustrates the method used by Dotsenko et al. The intensity of the clockwise

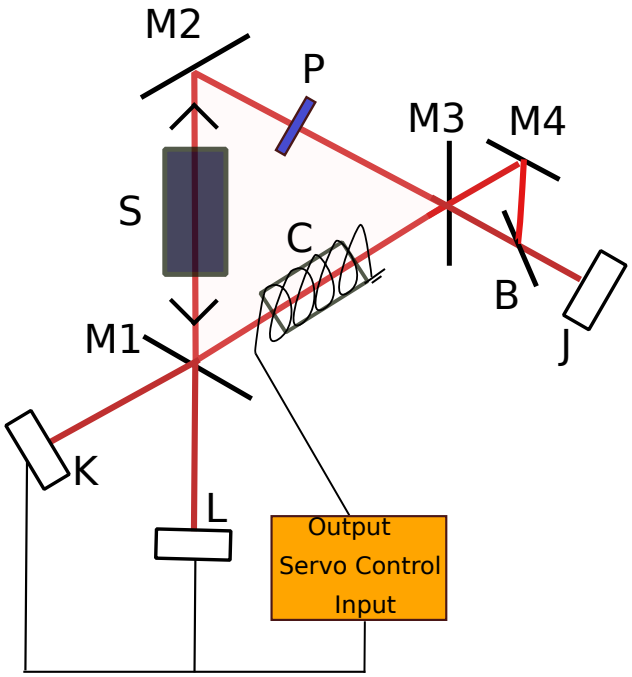

Figure 2.9: System demonstrated by Dotsenko et al. [3] to minimise competition between the beams. M1, M2 and M3 are cavity mirrors. M4 is fold mirror. B is beam splitter. P is linear polariser. S is solid state gain medium (Nd^{3+}:YAG). C is Faraday rotator. L, K and J are photo detectors.

and counter-clockwise beams are monitored by photo detectors K and L. When the beam intensity changes, the current applied to a Faraday rotator is activated so the beam with higher intensity will have a polarisation rotation leading to an increase in loss for that beam. This servo control maintains equal power for both beams. This technique was not applied to the SSRL work in this thesis, as it was possible to accurately measure rotation without it.

Research into SSRLs ceased after the collapse of the Soviet Union. Recently however, interest has been renewed [34, 35]. This development was aided by the advent of reliable laser diode pumping [36] methods rather than arc lamp pumping used by the earlier researchers in SSRLs.

Schwartz, et al. have also vibrated the gain medium itself which decreases the gain

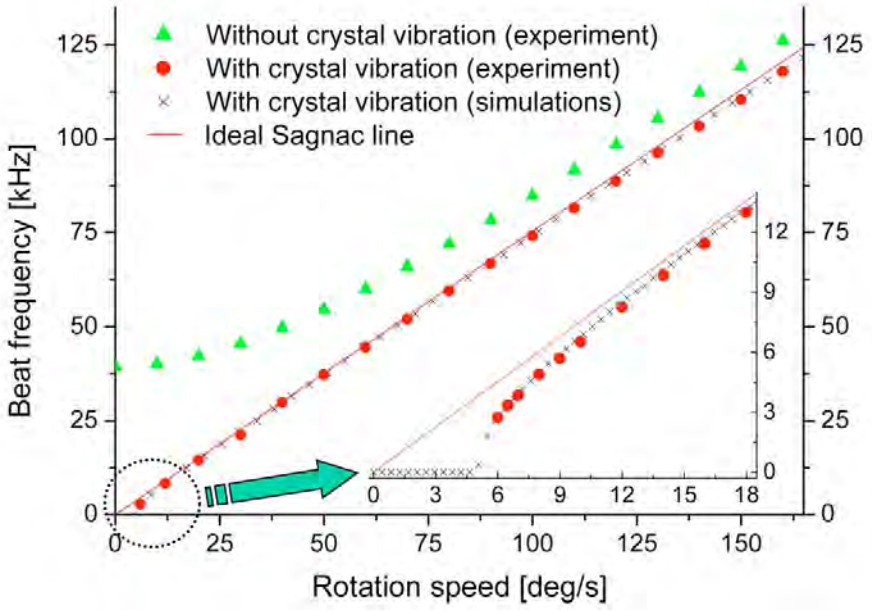

Figure 2.10: Sagnac frequencies for Nd^{3+}:YAG ring gyroscope with a 3 mm gain medium and a perimeter of 22 cm. It was obtained from the [4].

grating hence decreasing the coupling between the beams [37]. This technique of vibrating the crystal was shown by Danielmeyer et al. [38] in 1969 to achieve single mode operation in a linear laser. With this technique Schwartz, et al. were able to show that the SSRL rotation-sensing behaviour improved. Figure 2.10 demonstrates behaviour of the Nd^{3+}:YAG ring laser without and with crystal vibration. The crystal was vibrated with a frequency of 168 KHz. This vibration frequency depends on the upper lasing level lifetime, if the Er^{3+}-Yb^{3+}: phosphate[2], gain medium was used it will have lower vibration frequency to decrease the gain gratings. Furthermore, gain gratings cause SSRLs to have two extra modulation regimes compared to gas ring laser, periodic switching of intensity between the beams and chaotic intensity modulation [39].

For all the research mentioned above the Nd^{3+}:YAG gain medium was used. The work in Chapters 4 and 5 looks at different types of gain media, specifically Nd^{3+}:phosphate (Chapter 4) and Er^{3+}-Yb^{3+}:phosphate glass (Chapter 5).

[2]Upper lasing level life time of Er^{3+}-Yb^{3+} is 35 times larger than Nd^{3+}:YAG.

Chapter 3

Backscatter Coupling

3.1 Introduction

Coupling between two oscillators was first noticed by Christian Huygens when observing two pendulum clocks. When two clocks whose pendulums had nearly identical period were hung on the same wall the oscillations between them became coupled by the wall. Eventually, the pendulums oscillated at precisely the same frequency. The same principle applies to ring lasers. The clockwise and counter clockwise beams in a ring laser can be considered as two oscillators. Instead of the wall coupling the two oscillators the backscattered light from defects or dust on the mirrors couples them together. In effect, backscatter coupling induces a change in frequency independent of the rotation experienced by the laser. In the earlier stage of laser gyroscope development, the coupling was large enough to cause frequency of the beams to be the same (the effect became known as "lock-in"). This problem was solved by applying a rotational bias. In small navigational gyroscopes, bias was applied by mechanical dithering, while large gyroscopes such as those at the University of Canterbury use the rotation of the Earth. Even with the bias, however the Sagnac frequency is still affected by backscatter. As the size of the ring laser gets larger, the Sagnac frequency due to a constant rotation rate (i.e. Earth rotation) gets larger, and the systematic error due to backscatter becomes proportionally less, but still not negligible. The aim of this chapter is to develop a method to correct the changes in Sagnac frequency due to backscatter. Initially, we will look at the Alder pulling mechanism, pulling of the two laser frequencies closer together. Then we will move to a more complete model which contains frequency pulling and pushing. Finally, this model will be used to correct measured values from the ring lasers, G-0 and PR-1.

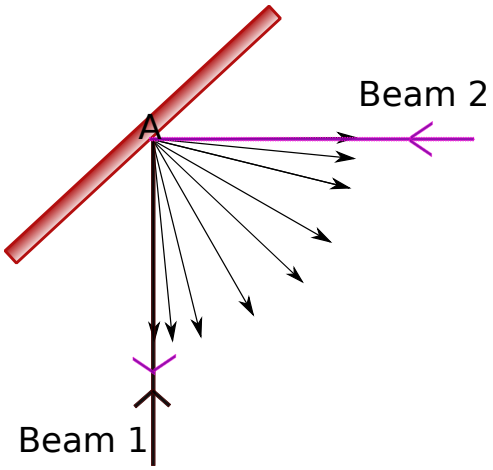

Figure 3.1: Beam 1 hits the surface at point A and scatters. Some of the scattered beam couples into beam 2. Beam 2 also scatters and couples into beam 1 but it is not shown on the diagram.

3.1.1 Alder Pulling.

Alder pulling was first investigated in oscillatory electrical circuits by Robert Alder in 1946 [40]. Here we apply this theory to two laser beams within a common ring cavity. When one beam interacts with the mirror surface some of the light from it is scattered back into the other beam. The process is shown in Figure 3.1. Two beams can be described by two phasors E_1 and E_2 as shown in Figure 3.2. The fractional amplitude of each beam that contributes to the opposite beam is denoted as r_1 and r_2. The contribution of r_1 and r_2 is causes less than 5 % modulation in large ring lasers. Assuming there is no backscattering the angular frequency $\omega_{1,2}$ of each phasor rotation can be represented as following:

$$\frac{d\phi_{1,2}}{dt} = \omega_{1,2} \tag{3.1}$$

The Sagnac frequency (ω_s) is defined to be the difference in angular frequency of beam 1 and 2:

$$\frac{d(\phi_1 - \phi_2)}{dt} = \omega_1 - \omega_2 = \omega_s \tag{3.2}$$

where ω_1, ω_2 are the unperturbed frequencies. If the ring laser were to follow equation 3.1 it would be a perfect rotational sensor as there is no coupling effect. To incorporate coupling, a backscatter term is added to equation 3.1:

$$\frac{d\phi_1}{dt} = \omega_1 + r_2 \cos(\phi_1(t) - \phi_2(t)) \tag{3.3}$$

$$\frac{d\phi_2}{dt} = \omega_2 - r_1 \cos(\phi_1(t) - \phi_2(t)) \tag{3.4}$$

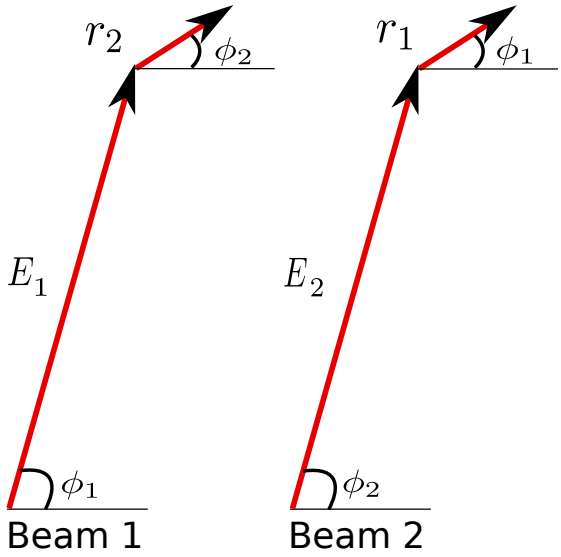

Figure 3.2: The large phasors E_1, E_2 shown are due to the primary beams, while the smaller ones on the top are due to scattered light from the opposite beam.

Equations 3.3 and 3.4 correspond to beams 1 and 2 respectively. If the perturbation shown in the above equations is incorporated into equation 3.2 it becomes:

$$\frac{d\phi_s}{dt} = \frac{d\phi_1}{dt} - \frac{d\phi_2}{dt} = \omega_1 - \omega_2 + (r_2 + r_1)\cos(\phi_1(t) - \phi_2(t)) \tag{3.5}$$

Separating variables and integrating over one cycle gives:

$$\int_0^{2\pi} dt = \int_0^{2\pi} \frac{d\phi_s}{\omega_1 - \omega_2 + (r_1 + r_2)\cos(\phi_1 - \phi_2)} \tag{3.6}$$

Equation 3.6 has the exact solution:

$$\omega_s^2 = (\omega_1 - \omega_2)^2 - (r_2 + r_1)^2 \cos^2(\phi_1 - \phi_2) \tag{3.7}$$

Hence the Sagnac frequency is pulled by the term $(r_2+r_1)^2\cos^2(\phi_1-\phi_2)$ by backscatter. In reality the theory described here is insufficient to describe the actual behaviour observed in ring lasers. This model assumes that the backscatter phase difference between the beams is zero which is not necessarily true. Furthermore, it does not take into account the effect of backscatter on the gain of each beam, and gain saturation. A complete theory of the ring laser will be further elaborated in the following sections.

3.2 Complete Model of Backscatter

To provide a complete picture of the backscatter dynamics, a set of differential equations were used. These equations have been developed by Lamb et al [41] for a linear laser then

extended by Aronowitz [22] and Stedman [42] to ring laser gyroscopes. The following subsections investigates these equations in the context of the gas ring laser. The first part considers the effect of saturation, then the backscatter component is introduced.

3.2.1 Saturation Effects

A steady state condition where the cavity loss (ring cavity finesse is around 5×10^5) is equal to the gain is used to describe the additional modulation that affects the Sagnac frequency. The gain of the laser is shown in equation 3.8

$$g = g_0(1 + \frac{I}{I_{sat}})^{\alpha} \tag{3.8}$$

where g_0 is the unsaturated fractional gain, I is the beam intensity, and I_{sat} is the saturation intensity. α ranges between -0.5 and -1. This expression is well known [23] for homogeneous broadening (where $\alpha = -1$) and for the limit of inhomogeneous broadening ($\alpha = -0.5$). In the He-Ne case the situation is intermediate, and an intermediate value for α is plausible. Ultimately the justification for equation 3.8 comes from gain calculation, as described in Appendix A. In the He-Ne system the value of α depends on the ratio of Ne^{22} and Ne^{20}, the plasma temperature, gas pressure, and spontaneous decay rate for the higher and lower lasing transitions. At this stage it is worth looking at the two broadening mechanisms separately. In reality both processes are intertwined.

The losses in the cavity can be calculated by using the ring down time (τ) which describes the exponential decay of the cavity intensity when the gain is removed. Even with super mirrors with reflectivity of 99.9997 [43] ring lasers have a measurable ring down time. For example the comparatively small PR-1 ring laser has a ring down time of 97.4 μs while larger ring lasers have times in the millisecond range. The round trip loss in the cavity is the inverse of the product of the ring down and free spectral range (ζ). If we equate this with gain in equation 3.8 we get

$$g_0(1 + \frac{I_0}{I_{sat}})^{\alpha} = \frac{1}{\zeta\tau} \tag{3.9}$$

If a beam is running with an intensity I_1 and evolves in a way such that it reaches a steady state, the rate equation for the beam becomes:

$$\frac{dI_1}{dt} = I_1(g\zeta - \frac{1}{\tau}) \tag{3.10}$$

Where $g\zeta$ is the gain per unit time and $\frac{1}{\tau}$ is loss per unit time. Then equation 3.8 can be substituted into equation 3.10. This equation will contain g_0 as one of the variables.

Then equation 3.9 is substituted again for g_0. This leads to the following equation:

$$\frac{d\rho_1}{dt} = \rho_1[(\frac{1+\rho_1}{1+\rho_0})^{\alpha} - 1]\tau^{-1} \tag{3.11}$$

For convenience $\frac{I_1}{I_{sat}}$ and $\frac{I_0}{I_{sat}}$ are denoted as ρ_1 and ρ_0. Equation 3.11 only describes the effect of one beam. To include the saturation effect of the beam travelling from opposite direction, equation 3.11 is modified as following:

$$\frac{d\rho_1}{dt} = \rho_1[(\frac{1+\rho_1}{1+\rho_0})^{\alpha}(\frac{1+\rho_2}{1+\rho_0})^{\beta} - 1]\tau^{-1} \tag{3.12}$$

where α is the cross saturation coefficient and β is the self saturation coefficient. Figure 3.3 shows the ^{20}Ne and ^{22}Ne gain curves seen by one of the laser beams. The overall curve is the sum of these. The gain curve is predominantly inhomogeneously broadened due to the movement of helium and neon atoms travelling with different velocities in the direction of the beam. Self saturation causes a hole to be burned in the middle (b) of the gain curve while cross saturation occurs at the ends of the gain curve (a). When the beam travels through the gain medium it burns a hole at (b) which is in resonance with the group of gas atoms. It also sees the hole (a) burned in the side of the gain curves by the opposite beam, which is resonant with the molecule at point (a).

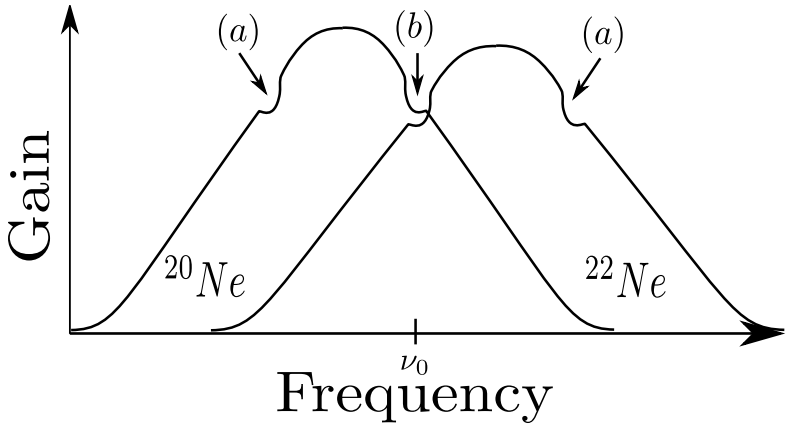

Figure 3.3: Ne^{22} and Ne^{20} gain curves and the hole burning process seen through the perspective of one beam.

3.2.2 Backscattering Component

In addition to gain saturation, the backscatter effects need to be included. Using a similar argument to the one used in Adler pulling the electric field for each beam can be described as shown in the phasor diagram of Figure 3.4. The reference point and time origin were

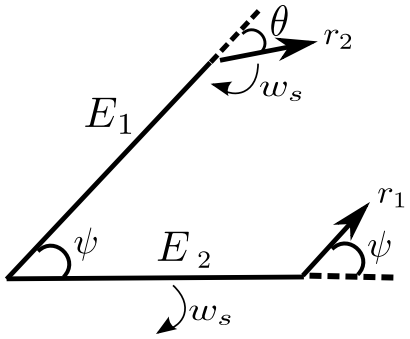

Figure 3.4: Phasor diagram illustrating the process of backscatter coupling. (The magnitudes of r_1 and r_2 are greatly exaggerated.) The vectors E_1 and r_1 are fixed, causing vectors E_2 and r_2 to spin at the Sagnac frequency (w_s).

taken so that the backscatter amplitude of beam 1 (E_1) is in phase ψ with beam 2 (E_2) and r_1 is parallel to E_1. Furthermore, r_2 has the phase angle θ. The interaction of these vectors can be observed by monitoring individual beams though a photo detector. As the backscatter vectors r_1 and r_2 rotate, the intensity of the ring laser gets modulated. The magnitude of the vectors depends on the strength of backscattering from the other beam. Vectors r_1 and r_2 are the sum of the scattering occurring on all the mirrors. For our case this is the sum of four vectors caused by having four mirrors in the cavity. In a perfectly stable cavity the magnitudes of r_1 and r_2 would not change, but in practice there are small drifts in arm lengths, for instance associated with variation in temperature or perhaps change in barometric pressure. This causes the relative phases of the backscattering from the mirrors to change, causing changes in the resultant total backscatter. In worst cases, mode hops cause discontinuities. It is expected that a more dimensionally stable laser such as the German G-ring would have lower variation compared to a less stable laser such as PR-1.

Finally, the backscatter component in this section was added to equation 3.12. This is obtained from Figure 3.4. We allow the beams to have different intensities ρ_1 and ρ_2. r_1 and r_2 are scattered *amplitude* fractions, therefore to describe their effects on the *intensities*, we must multiply by $\rho_1^{\frac{1}{2}}$, $\rho_2^{\frac{1}{2}}$.

$$\frac{d\rho_1}{dt} = \rho_1[(\frac{1+\rho_1}{1+\rho_0})^{\alpha}](\frac{1+\rho_2}{1+\rho_0})^{\beta} - 1]\tau^{-1} + 2r_2 f_L(\frac{\rho_2}{\rho_1})^{\frac{1}{2}}\cos(\psi) \tag{3.13}$$

$$\frac{d\rho_2}{dt} = \rho_2[(\frac{1+\rho_2}{1+\rho_0})^{\alpha}](\frac{1+\rho_1}{1+\rho_0})^{\beta} - 1]\tau^{-1} + 2r_1 f_L(\frac{\rho_1}{\rho_2})^{\frac{1}{2}}\cos(\psi+\theta) \tag{3.14}$$

The phase difference between beams 1 and 2 is subtracted to give the equation:

$$\frac{d\psi}{dt} = w_s - f_L[r_2(\frac{\rho_2}{\rho_1})^{\frac{1}{2}}\sin(\psi+\theta) + r_1(\frac{\rho_1}{\rho_2})^{\frac{1}{2}}\sin(\psi)] \tag{3.15}$$

Finally, dispersion effects are added. This is because whenever gain varies with frequency, refractive index also changes with frequency. This leads to small changes in the resonant frequency. So a peak in the gain curve pulls a neighbouring resonance frequency towards it. This is referred to as *line pulling* by Siegman [23]. Conversely a hole nearby pushes the resonance frequency further away (mode pushing). Figure 3.5 shows the gain curve seen by one laser beam. The hole burned at (b) is by the beam itself. The two holes on each side (a) are burned by the other beam. The two holes (a) are almost symmetric. So the pulling of hole (a) is nearly cancelled out by the pulling of hole (b). However, the gain curves are not perfectly symmetric due to the difference in the widths of the Doppler broadening for Ne^{22} and Ne^{20}. The difference in broadening is caused by higher mass Ne^{22} having slower thermal motion. If both curves had the same width and the beams had the same power the dispersion would be zero.

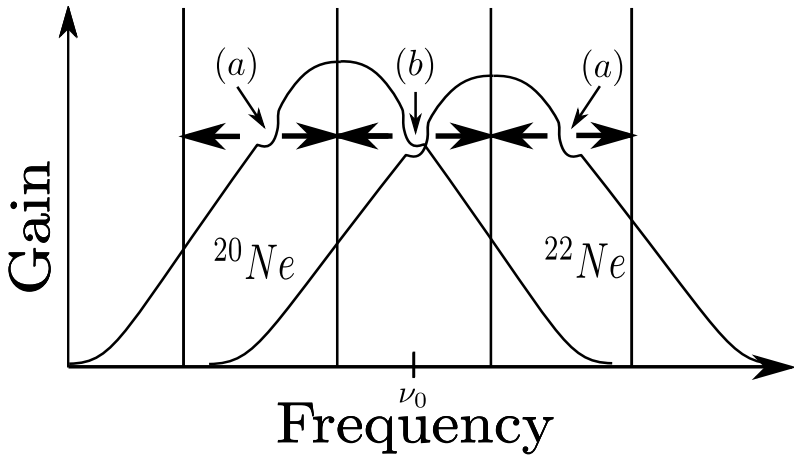

Figure 3.5: Ne^{22} and Ne^{20} gain curve. The hole burning process seen through the perspective of one beam, when the beam powers are equal.

In Figures 3.6 and 3.7 the beam powers are unequal. The beam with higher power burns a deeper hole than the lower power beam. This creates two scenarios depending on the perspective of each beam. In Figure 3.6 the hole (b) is the deepest causing more pushing away from resonance compared to holes (a) on each side. While in Figure 3.7 holes (a) is the deepest thus it causes more pushing than hole (b). These dispersion effects are added to the final equation below:

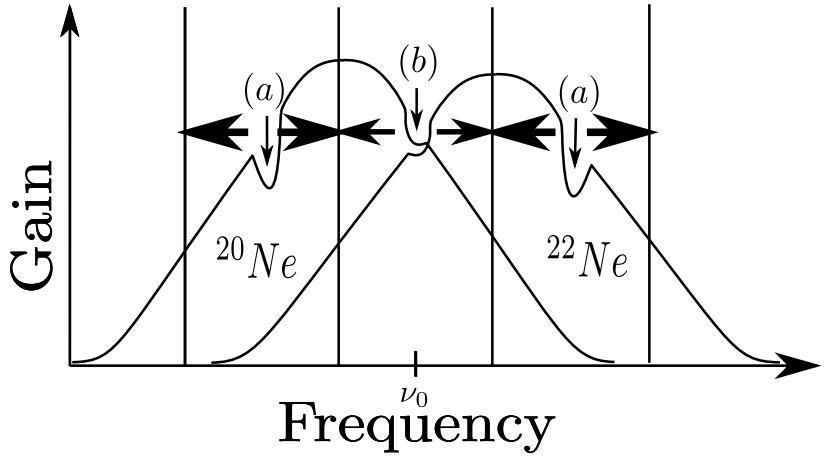

Figure 3.6: Ne^{22} and Ne^{20} gain curve. The hole burning process seen through the perspective of one beam, when the beam powers are different.

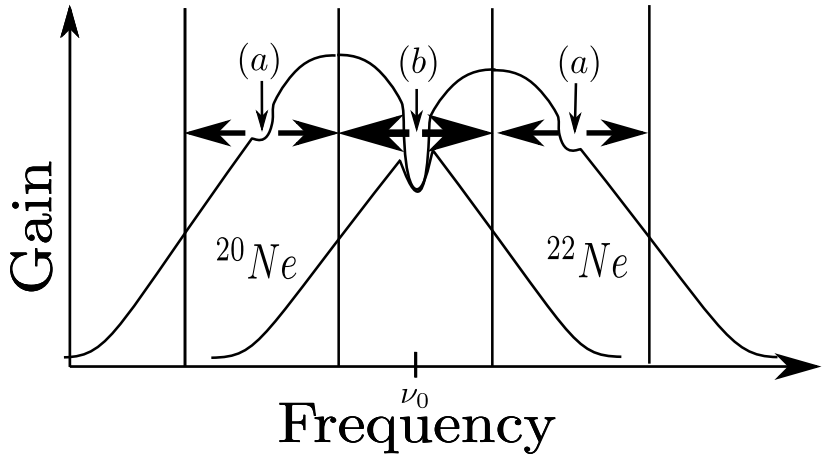

Figure 3.7: Ne^{22} and Ne^{20} gain curve. The hole burning process seen through the perspective of one beam, when the beam powers are different.

$$\frac{d\psi}{dt} = w_s - f_L[r_2(\frac{\rho_2}{\rho_1})^{\frac{1}{2}}\sin(\psi+\theta) + r_1(\frac{\rho_1}{\rho_2})^{\frac{1}{2}}\sin(\psi)] + 2\pi\eta(\frac{\rho_2}{\rho_1}-1)\tau^{-1} \tag{3.16}$$

where η is the coefficient associated with the shift in Sagnac frequency and $(\frac{\rho_2}{\rho_1}-1)$ is the fractional imbalance in beam intensity. The equations 3.13, 3.14 and 3.16 are the main equations describing the behaviour of the laser and will be explored further throughout this chapter. The three equations were solved numerically using a fourth order Runge-Kutta method.

3.3 Approximate Solutions

To physically understand the three equations mentioned in the previous section we look at approximations of them. But our main eventual aim is to provide numerical solutions which do not have any approximations.

If we assume the laser is running just above the lasing threshold, the saturation effects can be ignored as the cross saturation and self saturation coefficients in the equation 3.13, 3.14 will be approximated to zero. In other words, the gain is equal to the losses in the cavity. Also, ρ_1 and ρ_2 average to be ρ_0, implying the mean intensity of the two beams are the same. Finally, we ignore the small frequency modulation and make ψ equal to $w_0 t$. With these approximations the equations are integrated to give:

$$\rho_1 = \rho_0(1 + \frac{2r_1 f_L}{w_s t}\sin(w_s t)) \tag{3.17}$$

$$\rho_2 = \rho_0(1 + \frac{2r_2 f_L}{w_s t}\sin(w_s t + \theta)) \tag{3.18}$$

The parameter θ in the differential equation shows up as the phase difference between the monobeam modulations. The fractional intensity modulations (m_1,m_2) that will be used later on to determine r from the output of the laser are defined from the equation below.

$$m_1 = \frac{2r_2 f_L}{w_s}, m_2 = \frac{2r_1 f_L}{w_s} \tag{3.19}$$

Using these expressions above, there are two special cases, one causing an increase and the other a decrease in the Sagnac frequency.

3.4 Special Solutions

Two special solutions for the differential equations are the cases where the monobeam modulations are equal, and either in phase or anti phase. We describe these as pure common-mode and pure differential mode cases. In reality they do not usually occur separately but in combination with each other.

3.4.1 Pure Common Mode Modulation

The pure common mode occurs when the phase angle θ equals zero and $r_1 = r_2$. The intensities of the beams are equal to each other. Furthermore, m_1 and m_2 are also equal.

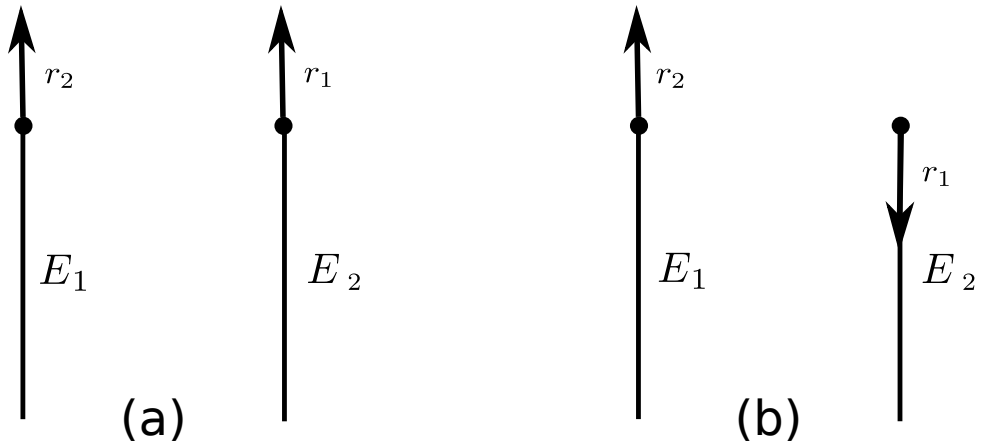

Figure 3.8: (a) Common mode, (b) differential mode.

We denote the common mode fractional modulation as m_c. When these conditions are imposed equation 3.16 becomes:

$$\frac{d\psi}{dt} = w(1 - m_c \sin\psi) \tag{3.20}$$

Solving this exact equation using separation of variables gives:

$$\int_0^{2\pi} \frac{d\psi}{1 - m_c \sin(\psi)} = \int_0^T w dt \tag{3.21}$$

Where T is the period.

$$\frac{2\pi}{\sqrt{1 - m_c^2}} = wT \tag{3.22}$$

Since m_c<1 a binomial approximation ($\frac{1}{\sqrt{1-m_c^2}} = 1 - \frac{1}{2}m_c^2$) is used to give:

$$w = w_s - \frac{1}{2} w_s m_c^2 \tag{3.23}$$

The term m_c^2 always will be positive, thus in this case there is always a decrease in Sagnac frequency.

3.4.2 Differential Mode Modulation

Unlike the common mode, this mode requires that the power of both beams are unequal. Other conditions of this mode are that θ is assumed to equal to π, while m_1 and m_2 are equal. The equations 3.17 and 3.18 are used to evaluate the expression $(\frac{I_1}{I_2})^{\frac{1}{2}}$ and $(\frac{I_2}{I_1})^{\frac{1}{2}}$

$$\frac{I_1}{I_2} \simeq \frac{1 + m\sin\psi}{1 - m\sin\psi} \qquad \frac{I_2}{I_1} \simeq \frac{1 - m\sin\psi}{1 + m\sin\psi} \tag{3.24}$$

Using a binomial approximation since $m << 1$:

$$\frac{I_1}{I_2} = 1 + 2m\sin\psi \qquad \frac{I_2}{I_1} = 1 - 2m\sin\psi \tag{3.25}$$

Again, use a binomial approximation to get:

$$(\frac{I_1}{I_2})^{\frac{1}{2}} = 1 + m\sin\psi \qquad (\frac{I_2}{I_1})^{\frac{1}{2}} = 1 - m\sin\psi \tag{3.26}$$

Substituting the above equations into equation 3.15, followed by insertion of equation 3.19 gives:

$$\frac{d\psi}{dt} = w(1 + m_D^2\sin^2\psi) \tag{3.27}$$

Integrating for a whole cycle gives:

$$\int_0^{2\pi} \frac{d\psi}{1 - m_D^2\sin^2\psi} = \int_0^T w_D dt \tag{3.28}$$

Where T is the period.

$$\frac{2\pi}{\sqrt{1 + m_D^2}} = wT \tag{3.29}$$

Since m_D<1 a binomial approximation ($\frac{1}{\sqrt{1-m_c^2}} = 1 - \frac{1}{2}m_c^2$) is used to give:

$$w = w_s + \frac{1}{2}w_s m_D^2 \tag{3.30}$$

The term m_D^2 will be always positive, so the Sagnac frequency always increases in this case.

3.5 Numerical Solutions

There were a number of approximations made to get these results. The Runge-Kutta numerical integration that was used to solve the three equations 3.16, 3.13 and 3.14 eliminates the need for the approximations that are used in the section. In this section equations 3.16, 3.13 and 3.14 are numerically solved using the fourth order Runga Kutta method. This will show that the approximation that are made on the previous section are valid. The parameters used for a square ring laser with 3.5 m sides (the G-0 laser). Its unperturbed Sagnac frequency is 288.3 Hz. The laser was filled with 0.2 millibar of 50:50 isotope ^{22}Ne and ^{20}Ne and 5.2 millibar of helium. It was operated at 60 % of multimode threshold. Inputting these parameters into the gain curve calculation spread sheet developed by Dr. Bob Hurst gives $\alpha = -0.585$ $\beta = -0.098$ (Appendix A). The

power it was run was at fraction of the multi-mode threshold[1] ($\rho_0 = 0.1$). The multi-mode threshold corresponds to $\rho = 0.18$ (from the gain curve calculation). The operating power needs to be less than this to achieve single mode operation. The backscatter coefficients r_1 and r_2 are calculated to be 0.981 ppm and 0.839 ppm using the ratio of AC/DC signal from the monobeam using equation 3.19. The free spectral range (f_L) of the laser was 21413 kHz. The dispersion coefficient ν is 0.0001023 [44] (Appendix A). Finally, the measured ring down time was 530 μs. All the parameters mentioned here are substituted into equations 3.16, 3.13 and 3.14 and then the equations are numerically solved using the Runga Kutta method. The step size used was 0.0001 second. The initial conditions for the equations were $\rho_1 = \rho_2 = 0.1, \psi = 0$ for beams 1 and 2.

3.5.1 Outputs From the Numerical Integration

The integration was done for 10 seconds for a number of θ values. Figure 3.9 shows the output of the two monobeams late in the 10 s integration period. This integration time allows for any initial transients to die away. In this particular example θ is chosen to be equal to zero. Hence the overlap of the two beams in the figure. Also, the r value entered

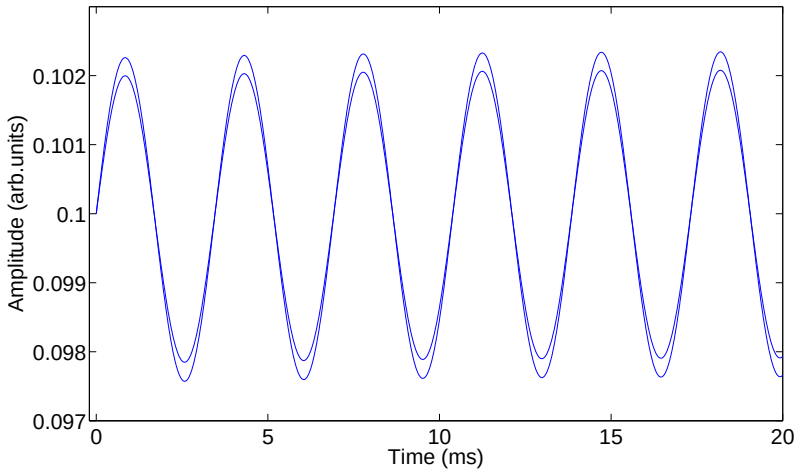

Figure 3.9: Waveform of two monobeams (ρ_1 and ρ_2).

into the equation for one of the monobeams is larger leading to the larger amplitude apparent in Figure 3.9. Both waves start at the set initial condition of 0.1. If the initial value is far away from the steady state beam amplitude it will take longer time to settle to a steady oscillation.

[1]Multi-mode threshold is when the power of the laser is just high enough to have more than one longitudinal mode oscillating in the cavity.

The third output from the integration is phase. It is shown in Figure 3.10 as a function of time. If there is no perturbation due to backscattering it will be a straight line with a gradient of $2\pi f_s$ where f_s is the Sagnac frequency of the laser. The line contains

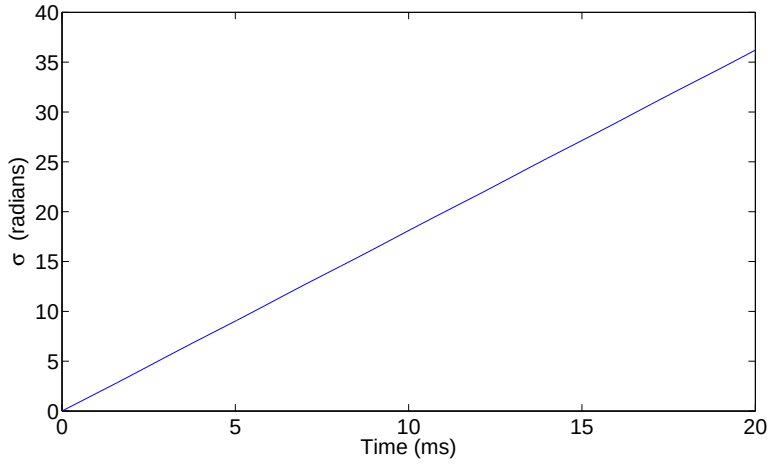

Figure 3.10: Phase of the perturbed modulation.

perturbations which can be observed by fitted a straight line through Figure 3.10 and taking it away to produce Figure 3.11. It contains modulation that is equal in frequency to the modulation from beams 1 and 2.

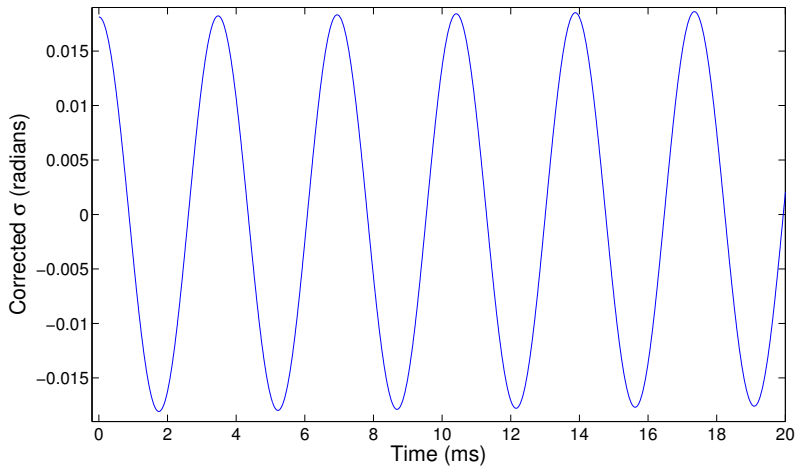

Figure 3.11: Close up of the perturbed modulation.

3.5.2 Measuring Perturbation

The output waveform from the Runge-Kutta solver was collected for 10 seconds at a step size (h) of 0.0001 s. The measured frequency remained the same regardless of the length of the collection time. It takes a modern desktop (pentium i7) 11.73 seconds to do this task. The solver was run for fixed values of r_1 and r_2 and a range of values of θ. The output was put through the Labview code shown in Figure 3.12. The output from the Labview

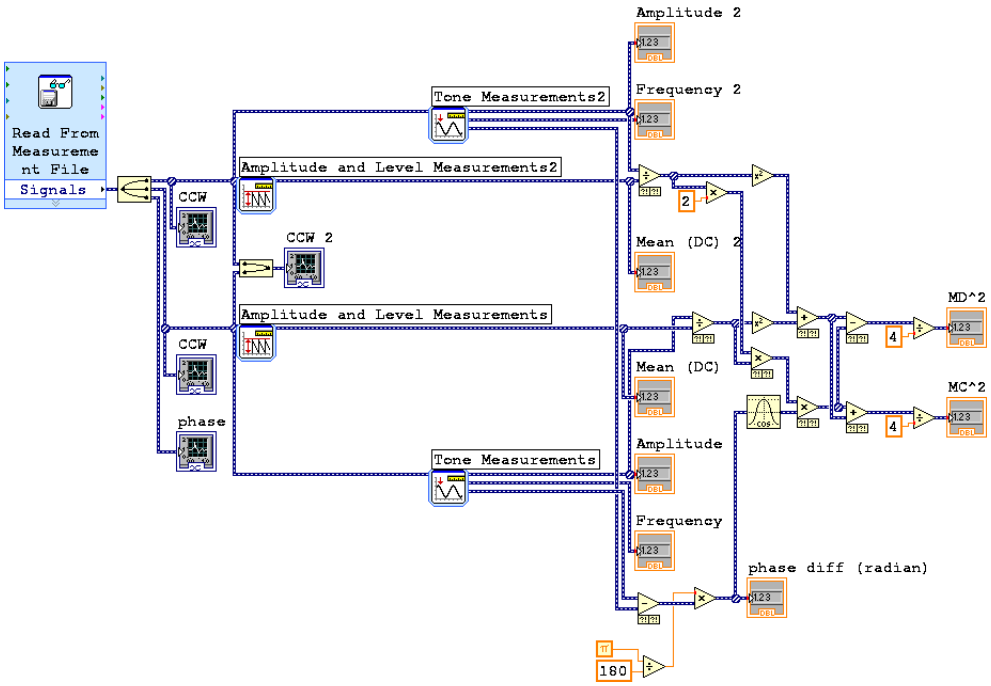

Figure 3.12: Measuring frequency and calculating common and differential modes.

programme is shown in Table 3.1. The m_d^2 causes an increase in Sagnac frequency and m_c^2 decreases the frequency. When the two values are equal the Sagnac frequency does not change. If one is larger than the other, the frequency shifts towards the largest side. This effect is clearly visible in Table 3.1. For example, in the first row of the table m_d^2 is smaller than m_c^2 so the Sagnac frequency decreases. In the fourth row the m_d^2 is larger so the frequency increases.

3.5.3 Common and Differential Mode Coefficients

In subsection 3.4.2 the coefficients for common and differential modes were found to be equal to half the unperturbed Sagnac frequency. In this section we take an extra logical step, assuming that the same coefficients for common and differential mode apply to the

θ	m_c^2	m_d^2	Frequency (Hz)
$\pi/4$	0.000420888	0.0000735882	288.247632
$\pi/3$	0.000370019	0.000124454	288.262039
$\pi/2$	0.000247232	0.000247368	288.297396
π	0.00000181762	0.000493723	288.371045
0	0.000492952	0.0000018224	288.228378

Table 3.1: Common and differential mode squared and corresponding frequencies.

mixture of common and differential modes. This is then verified by experiment. Values from Table 3.1 are fitted to an equation:

$$f = 288.3 - Am_c^2 + Bm_d^2 \tag{3.31}$$

Where f is the perturbed Sagnac frequency, while A and B are determined by fitting a plane. The A and B values for the plane in Figure 3.13 are 149 and 143. These values are

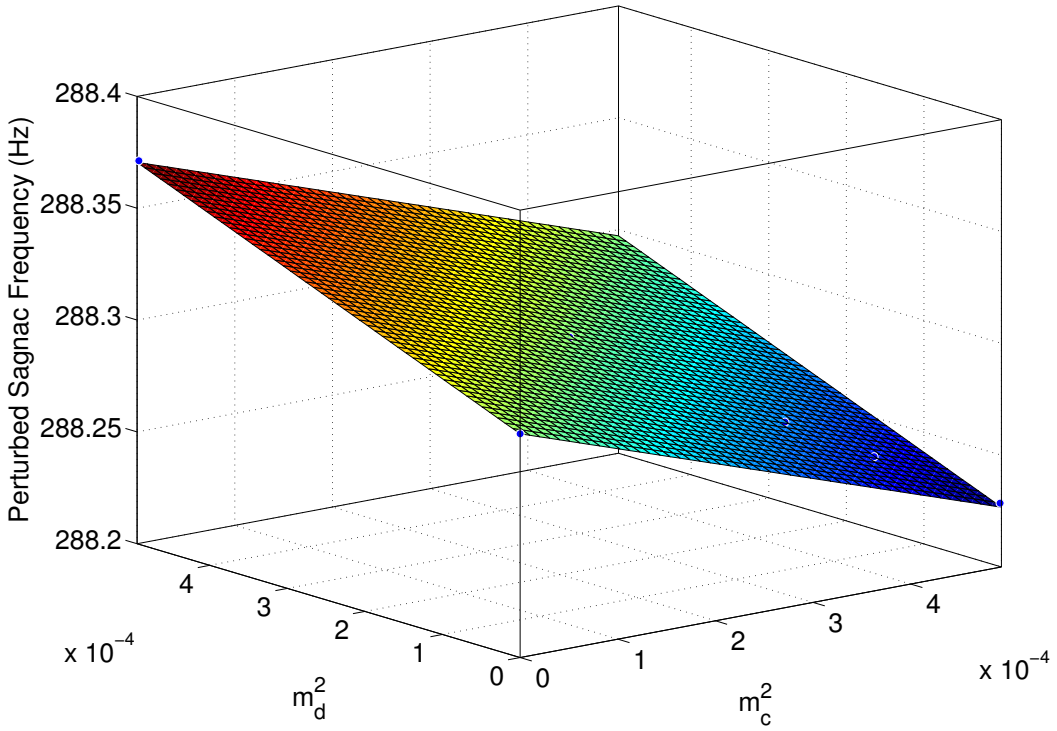

Figure 3.13: Fitting for equation 3.31. The A and B coefficients are determined from this plane.

close to the value of 144 (288/2) shown in section 3.4.2. The difference is due to saturation

and cross saturation effects that are not taken into account by the approximation. If the backscattering effect gets larger (to give intensity modulations > 5%) these effects become more important. Even though Figure 3.13 is a plane, for large backscatter modulation it takes more complex shapes. Fortunately, it is unusual for the large gas lasers that are being investigated here to have monobeam modulation greater than 5%.

3.5.4 Applying Correction to the Output from the Laser

Using the values for A and B from the previous section and equation 3.31 a correction for the backscatter can be determined. Fortunately, m_c^2 and m_d^2 in equation 3.31 can be measured from the monobeam modulation and the phase difference between the beams (ψ). If the m_1 and m_2 are taken as complex amplitudes, then m_c and m_d each become:

$$m_c = (m_1 + m_2)/2 \quad m_d = (m_1 - m_2)/2 \tag{3.32}$$

The equation above can be represented using the cosine rule as:

$$m_c^2 = (m_1^2 + m_2^2 + 2m_1m_1cos\Phi)/4 \quad m_d^2 = (m_1^2 - m_2^2 - 2m_1m_1cos\Phi)/4 \tag{3.33}$$

The value of m_1 and m_2 is the AC divided by the DC amplitude of the respective monobeams. The phase difference ψ can be measured directly. Applying the A and B coefficients and m_c^2 and m_d^2 it is possible to correct for the perturbations using equation 3.31.

Correction for the G-0 Laser

G-0 is a 3.5 m by 3.5 m laser located in the Cashmere cavern, Christchurch, New Zealand. Its unperturbed Sagnac frequency is 288.3 Hz. The parameters used in section 3.5 directly apply to this laser. The A and B coefficients are 149 and 143. The measured m_1 and m_2 values are shown in Figure 3.14. This is obtained from the two photomultiplier tubes on the clockwise and counter clockwise beams. Using equation 3.33 and the phase difference (ψ) measured from the photo diodes (see Figure 3.15), m_c^2 and m_d^2 are calculated as shown in Figure 3.16. From the figure the common mode is usually larger, so there is more contribution from the backscatter phasors which are in phase with each other than the anti-phase. When the correction is applied, the Sagnac frequency for common mode is usually increased. It should also be noted that there is a sharp drop close to 187.4 days caused by a mode hop. There are three mode hops shown in the G-0 data. The frequency of the mode hops are dictated by the change in environmental conditions such

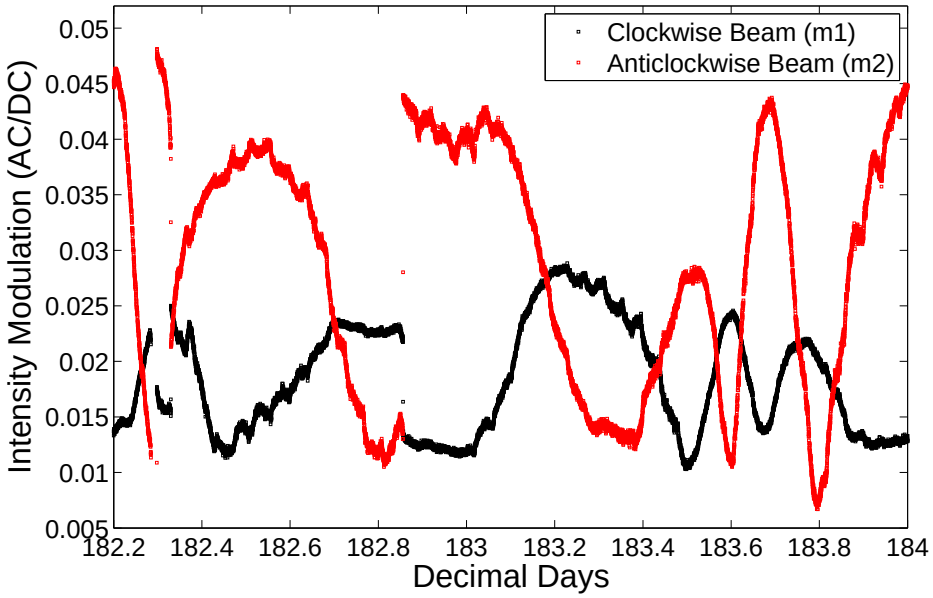

Figure 3.14: Fractional intensity modulation of the CW and CCW beams for G-0.

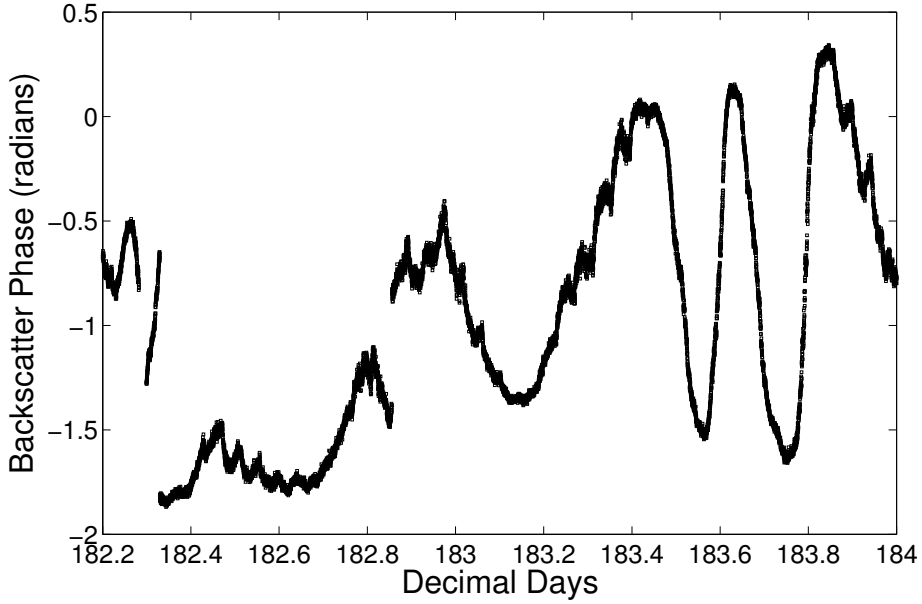

Figure 3.15: Phase difference between the clockwise and counterclockwise beams for G-0.

as temperature. Mode hops could be avoided by careful control of the cavity parameters using piezo control, which is not implemented in our ring cavity. With active stabilisation the performance of the gyroscope will greatly improve. Overall, the improvement of the Sagnac signal is evident in Figure 3.17.

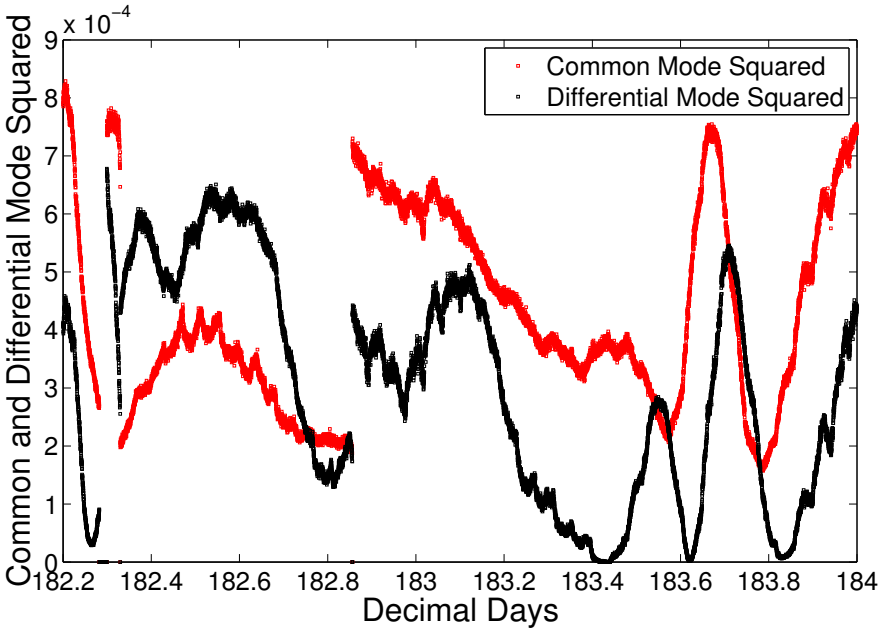

Figure 3.16: Common and differential mode beam modulation for G-0.

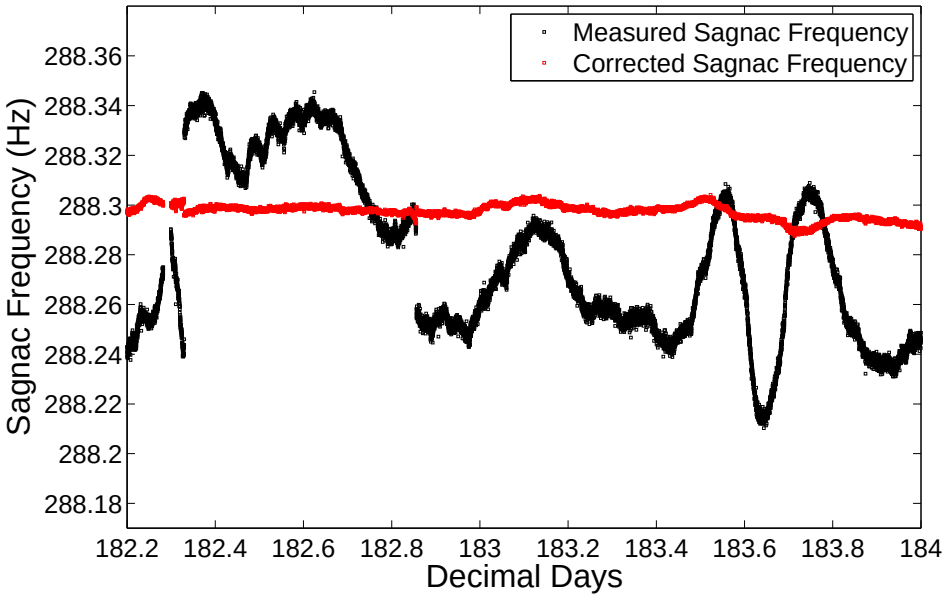

Figure 3.17: Raw Sagnac output from the G-0 laser and the corrected frequency.

Correction for the PR-1 Laser.

This is a smaller laser with arms of 1.6 m by 1.6 m. It is located inside an optical laboratory in the Rutherford building of the University of Canterbury.

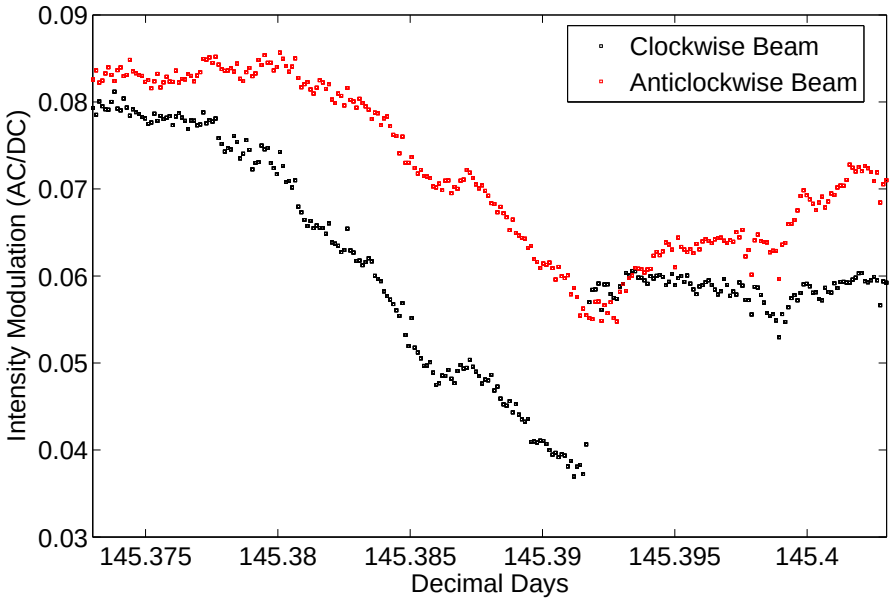

Figure 3.18: Fractional intensity of the CW and CCW beams for PR-1.

To calculate backscatter we used the same method as before. The A and B coefficient is $f_s/2$=56.75. Figure 3.18 shows the AC/DC ratio measured for PR-1. The measured phase difference (ψ) between the beams is shown in Figure 3.19. The m_c^2 and m_d^2 modes calculated from measured phase difference and AC/DC ratio is shown in Figure 3.20. Using the modes correction is applied to the raw Sagnac frequency as seen in Figure 3.21.

For PR-1 m_c^2 is less than m_d^2 so the overall effect is pulling (a decrease in the Sagnac frequency). The break in the data seen in all PR1 and G-0 figures are due to mode hops (where the laser changes to a different mode) or split mode operation where the laser is running on different mode numbers. The improvement in the Sagnac frequency due to correction is shown in Figure 3.21.

Performance Comparison

To compare the performance of the ring lasers Allan variance is calculated before and after the backscatter correction was applied. Allan variance σ_A is defined as [45]

$$\sigma_A^2 = \frac{1}{2(n-1)} \sum_{p=1}^{n-1} (\nu_{p+1} - \nu_p)^2 \tag{3.34}$$

where $\Delta\nu = \nu_{p+1} - \nu_p$ is change in frequency, and n is number of measurements. The data from the ring laser is collected in the measurement time interval τ. Figure 3.34 shows

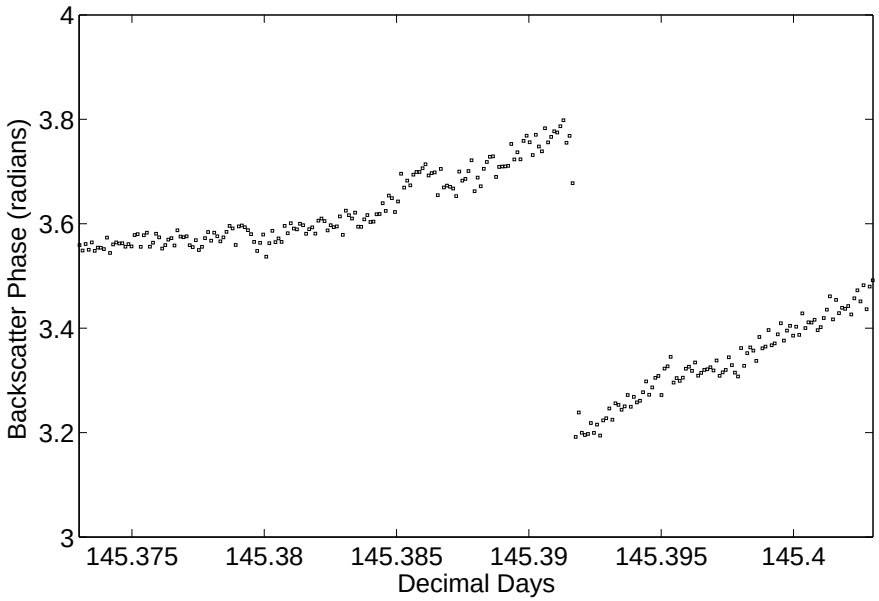

Figure 3.19: Phase difference between the clockwise and counterclockwise beams for PR-1.

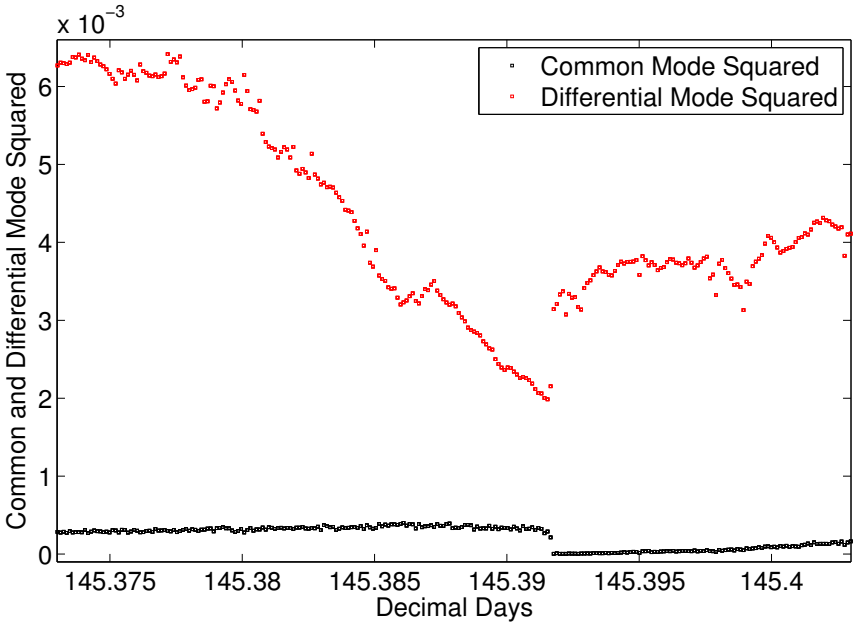

Figure 3.20: Common and differential mode for PR-1.

improvement in stability of both ring lasers after the correction has been applied. This stability improvement could be further increased with a longer mode-hop free time series.

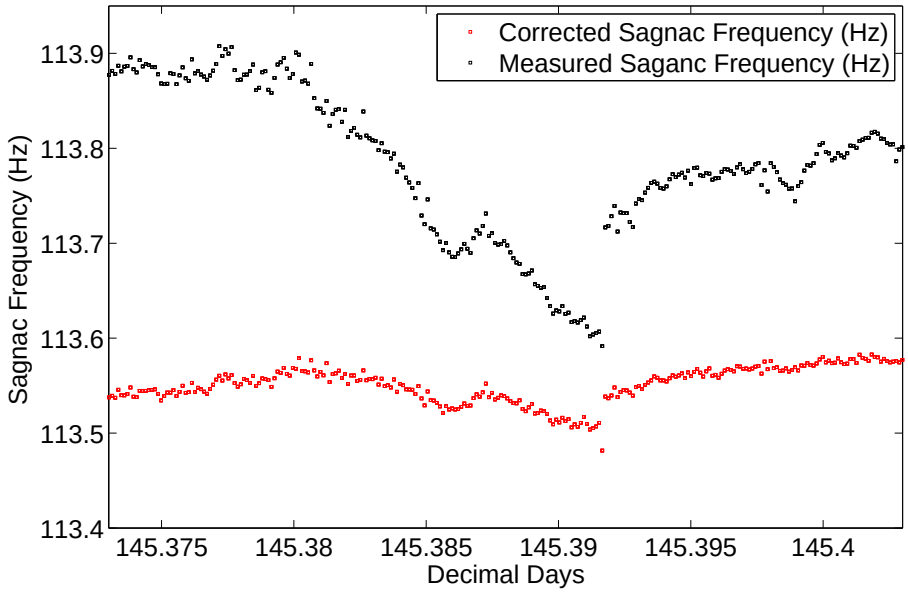

Figure 3.21: Raw Sagnac output from the PR-1 laser and the corrected frequency.

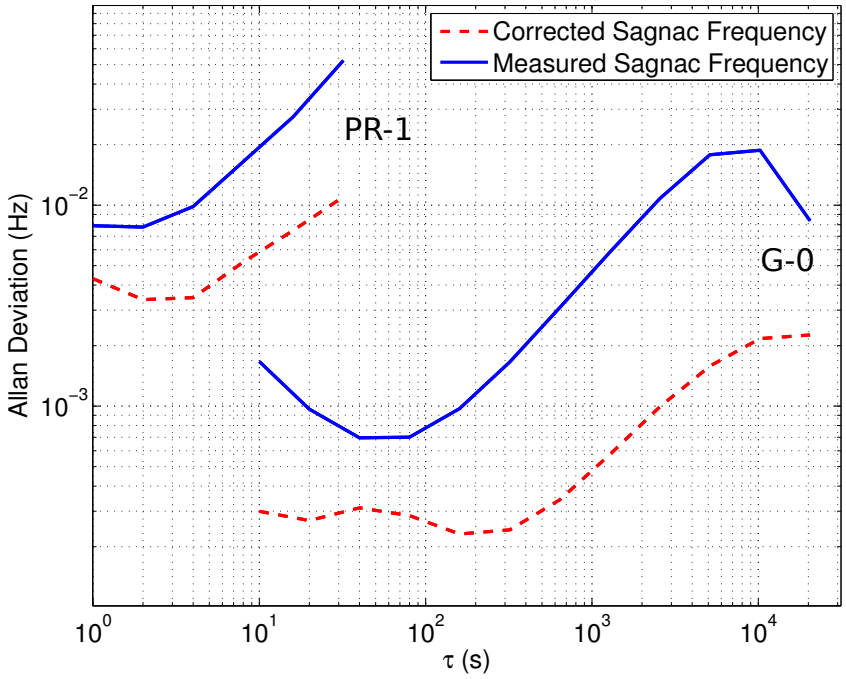

Figure 3.22: Allan variance of measured and corrected Sagnac frequency for G-0 and PR-1. The data used in the longest time period before a mode hop.

3.6 Inducing Backscatter

The backscatter effects seen in PR-1 and G-0 are due to back reflection from the ring laser mirrors. To introduce backscatter in a controlled manner a mono-beam was reflected back into the laser. Thus the back reflected clockwise beam combines with the anti clockwise beam, and visa versa.

The ring laser chosen for the experiment was the Gross-ring (G) in Wetzell Germany (Figure 3.23). It is a square ring with 16 m arms (Table 2.1). In terms of long term stability the G ring laser is far superior to any other large ring laser built due to its monolithic construction. Having this stability means once the correction is applied it does not need to be continually updated as with the other ring lasers.

For the back injection to be measurable it needs to be significantly larger than the back scattering from the cavity mirrors. Fortunately, G has lower backscattering compared to PR-1 and G-0.

3.6.1 Experimental Setup.

For the back reflected beam the corner with the largest transmission (C2) was used (see Figure 3.24). The mirrors (M1) and (M2) are placed in such a way that they reflect back the beams coming from the ring (B1, B2). Each beam is directed through lenses (L1) and (L2). These lenses are placed a focal length distance from the mirrors, so the light is retro reflected back along the exact path. (This configuration is commonly called a 'cats-eye retro reflector'.) The shutters (A1) and (A2) are placed between the lens and the mirror so they can be opened and closed with instruction from the computer. Notice in Figure 3.24 that insulation is attached to the shutters to minimise heat from the laser affecting the measurement. During the experiment it was discovered that the filters (GF1, GF2) were back reflecting some of the mono beam themselves so they were tilted.

3.7 Effect of Injection of the Monobeam into the Laser

When the mono beam is injected back into the laser it caused a similar effect as backscattering from a mirror but to a larger extent. The effect of shutters controlling the input into the ring laser is shown in Figures 3.26 and 3.27. At point (A) the shutter blocking

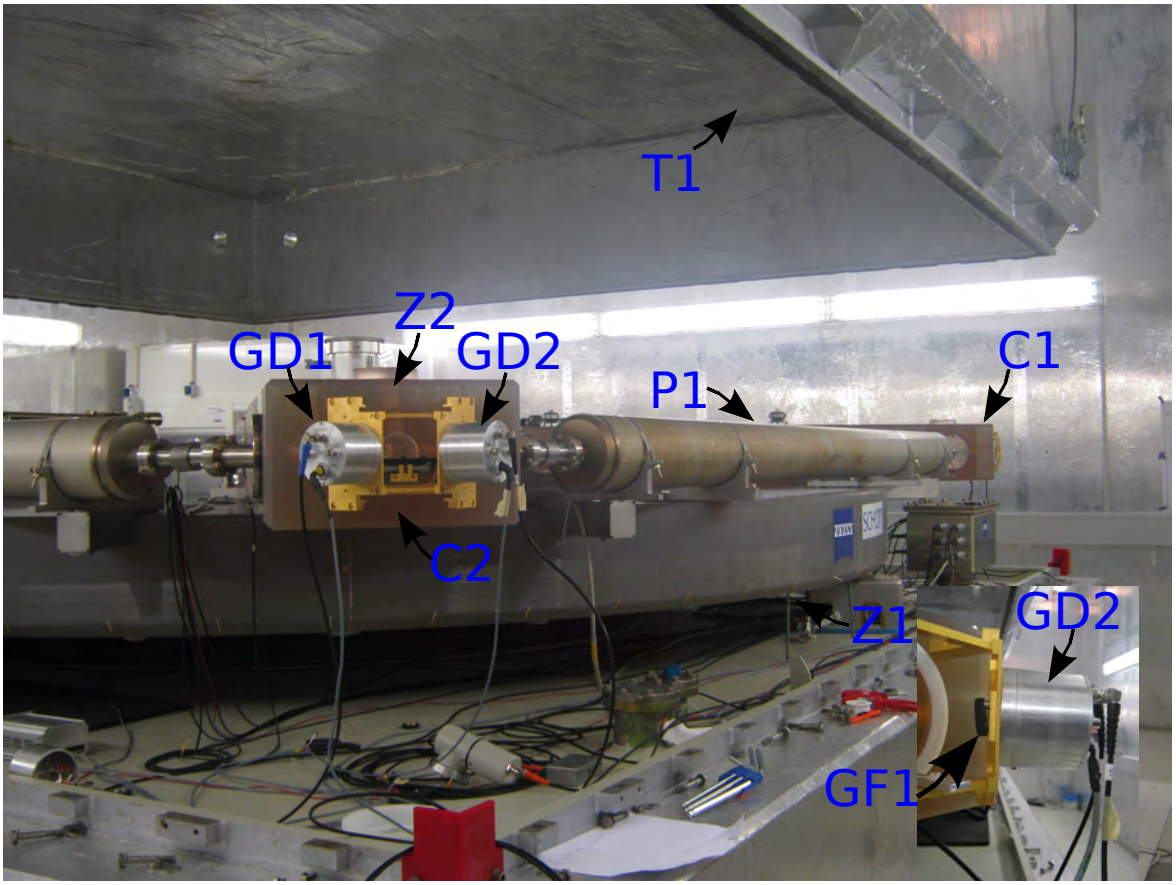

Figure 3.23: Experimental set-up for the G ring laser. GD1, GD2 are photo diodes. Z2 is a Zerodur block holding a corner box. Z1 is a large Zerodur plate the ring laser is mounted on. P1 is the arm of the ring laser surrounded by the gas getters to remove impurities in the He-Ne gas. GF1 is an a angled laser line filter. C2 is the corner of the ring laser the diodes are mounted on, while C1 is the corner where the monobeams are back reflected. T1 is a cover which decreases the effect of pressure on the ring.

the anticlockwise beam is opened while the other shutter is closed. At point (B), the shutter blocking the clockwise beam is opened while the other shutter is closed. It should be noted that back reflecting the clockwise beam has an effect on the anticlockise beam, and vice versa. The large modulation on the Sagnac frequency and intensity are due to a change in phase of the back reflection because of refractive index changes in the air path caused by heat from the electrical shutters. Some attempt was made to minimise this effect by adding foam near the shutter as shown in Figure 3.25.

When corrections similar to those applied to PR-1 and G-0 are applied the coefficients for A and B did not equal half the Sagnac frequency. This was probably due to incorrect measurement of the phase difference by the photodiodes (GD1, GD2 in Figure 3.24).

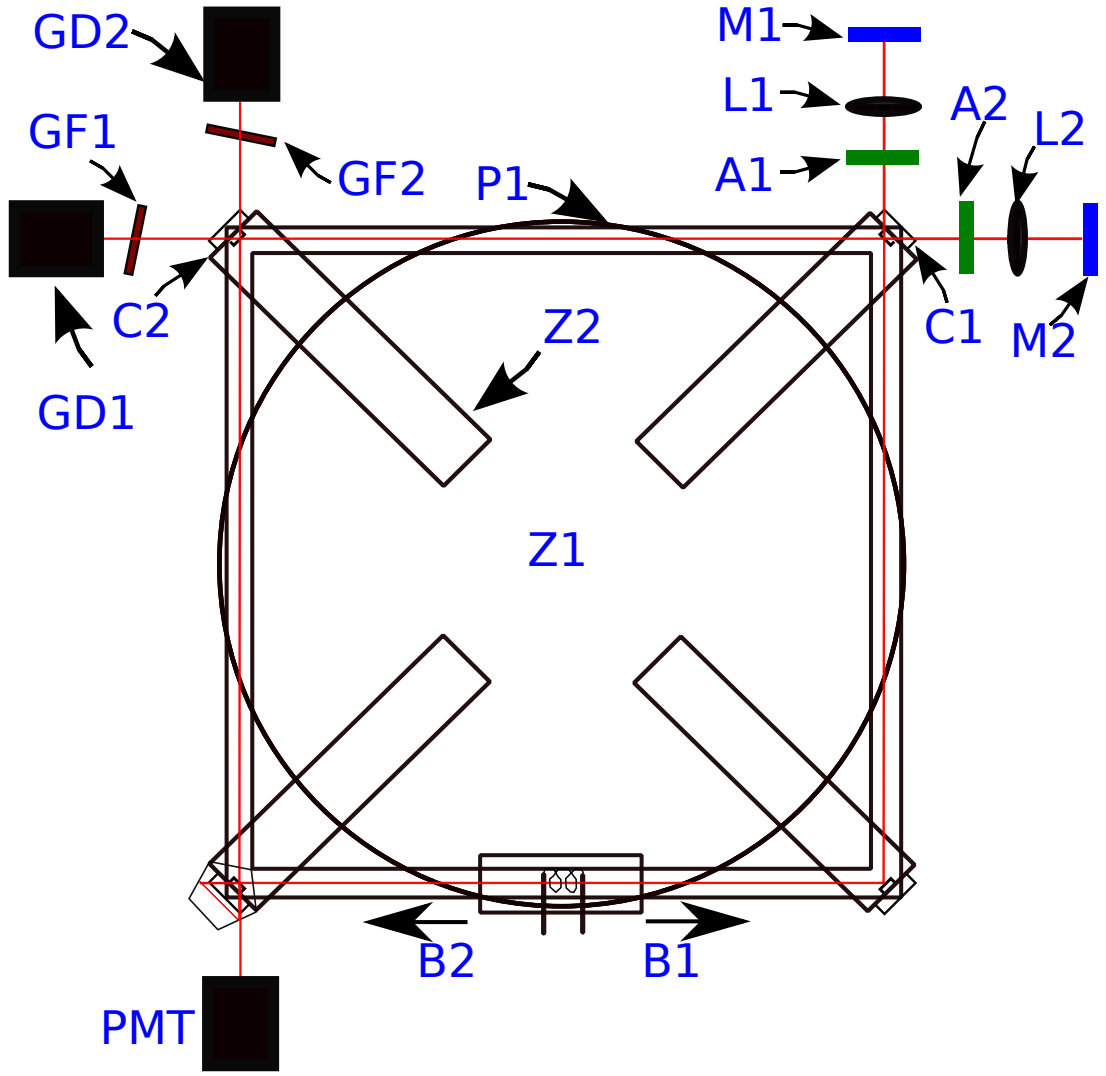

Figure 3.24: Experimental set-up for the G ring laser. GD1 and GD2 are photo diodes. Z2 is a Zerodur block holding a corner box. Z1 is a large Zerodur plate the ring laser is mounted on. P1 is arm of the ring laser surrounded by gas getter to remove impurities in the He-Ne gas. GF1 and GF2 are angled laser line filters. C2 is the corner of the ring laser the diodes are mounted, while C1 is the corner were the monobeams are back reflected. A1 and A2 are beam shutters. L1 and L2 are lenses. M1 and M2 are back reflecting planar mirrors. PMT is a photomultiplier tube. B1 and B2 are the anti clockwise and clockwise laser beams.

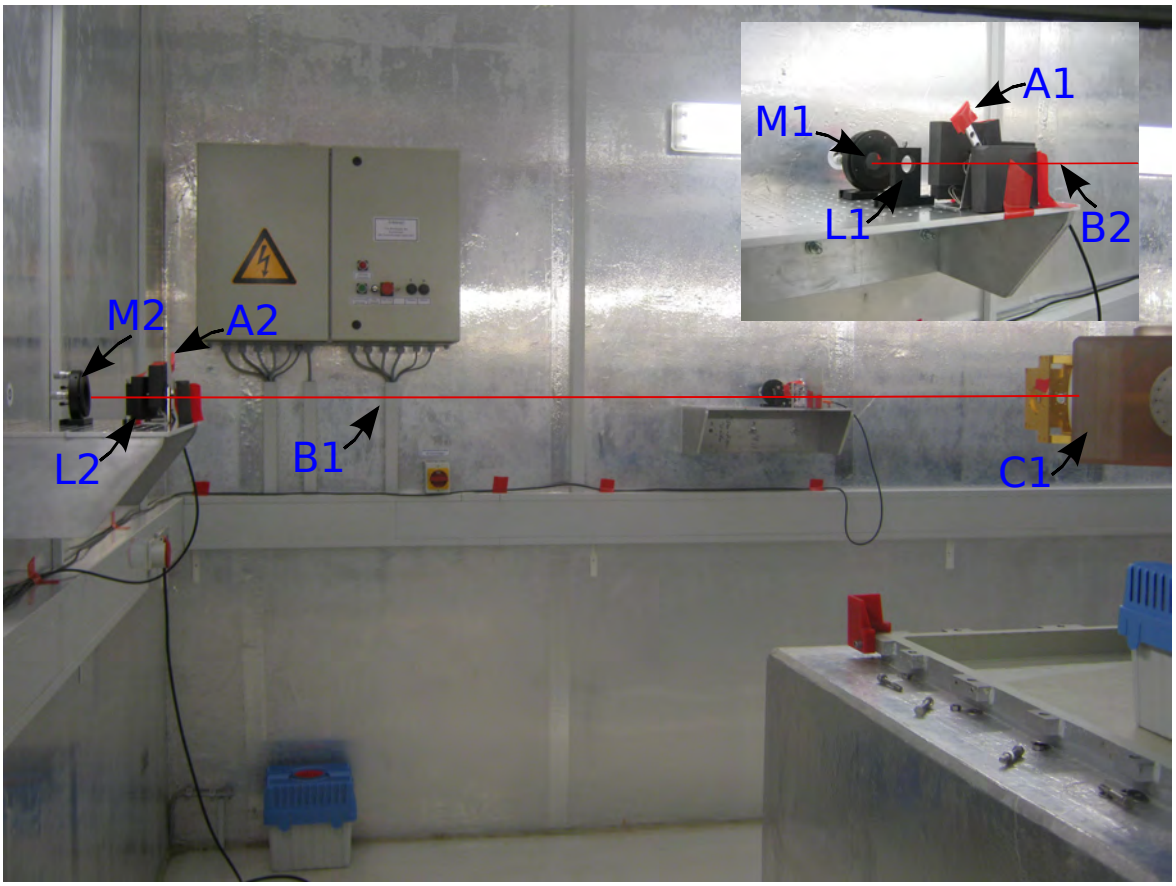

Figure 3.25: Experimental set-up for the G ring. A1 and A2 are beam shutters. L1 and L2 are lenses. M1 and M2 are back reflecting planar mirrors. B1 and B2 are the anti clockwise and clockwise laser beams.

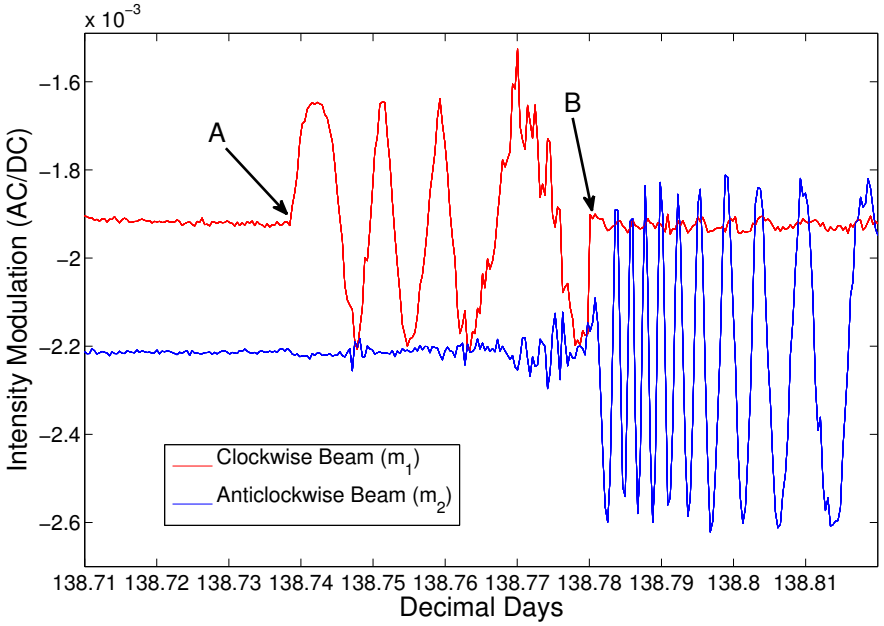

Figure 3.26: Fractional intensity modulation when one shutter is opened while the other is closed. Point A is when one shutter is opened while the other is closed. B is the opposite situation.

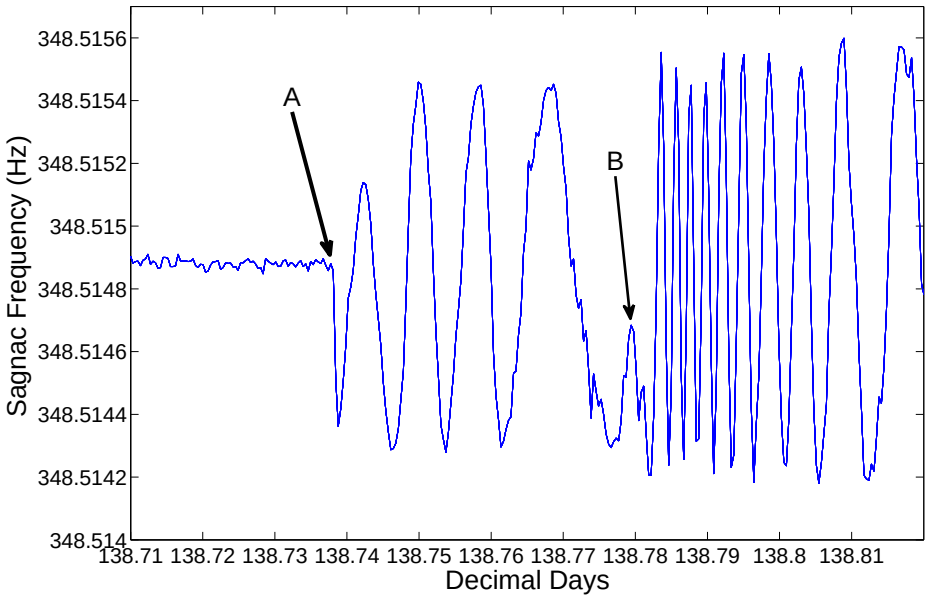

Figure 3.27: The effect on the Sagnac frequency when the shutters are opened and closed. Point A is when one shutter is opened while the other is closed. B is the opposite situation.

Fortunately, the experiment did clearly demonstrate the pushing and pulling effect of the Sagnac frequency which was monitored by the photomultiplier tube (PMT). This has never been experimentally demonstrated directly. Since the PMT is independent from the photodiodes used to measure the monobeams it is not affected by incorrect phase measurement. In hindsight a PMT would be better suited to measure the monobeam modulation. Furthermore, small amounts of cross saturation can be seen on the opposite beams in Figure 3.26. This is the direct experimental evidence that cross saturation exists and cannot be ignored.

3.8 Conclusion

It has been shown that the backscatter processes can be modelled and corrected for in a large ring laser to improve its absolute accuracy. This was successfully demonstrated on the PR-1 and G-0 ring lasers. Since backscatter will always be present in all large gas laser gyroscopes the need for this correction will always exist and this technique can be used to correct for backscatter if the required parameters are experimentally measured. It has been shown theoretically, pushing of the Sagnac frequency is caused by backscatter vectors that are opposite to each other, while pulling is caused by vectors that are parallel to each other. Appropriate differential equations are used to demonstrate the behaviour of the large ring gyroscopes. These equations were solved using integration by parts to produce backscatter coefficients for pulling and pushing that are half the Sagnac frequency. In order to integrate these equations, approximations were required. To confirm this result, numerical integration using a fourth order Runge-Kutta method was used without any approximations. The coefficients obtained from this method agreed with the result obtained with the approximation. Deliberate back reflection of a G-ring monobeam was performed to externally control the amount of backscatter. This was successful in experimentally demonstrating both pushing and pulling of the Sagnac frequency. It also experimentally demonstrated cross saturation. But the backscatter correction did not succeed possibly due to incorrect measurement of the monobeam phase.

Chapter 4

Solid State Laser Gyroscopes. Part 1: A Neodymium Doped Phosphate Glass Laser

4.1 Introduction

In this chapter, the design, construction and operation of a laser diode pumped solid state ring laser (SSRL) system is described, which utilises trivalent neodymium doped phosphate glass as the active medium. Currently, only neodymium-doped yttrium aluminium garnet (Nd^{3+}:YAG) continuous wave laser gyroscopes have ever been built. Nd^{3+}:YAG is the popular choice because it is isotropic (cubic space group symmetry) and has a large gain cross section. In YAG, 1 % of Y^{3+} are replaced by Nd^{3+}. The radius of the Nd^{3+} ion is 3% larger than the Y^{3+} ion [46]. The difference in the radii strains the crystal structure causing decrease in optical quality. On the other hand, phosphate glass will tolerate a very high impurity concentration. This enables the gain medium to be made thinner decreasing the number of periods of the unwanted gain grating. The ability to be doped at higher concentrations and having a lower loss compared to YAG (caused by lower parasitic emission) makes it an attractive candidate for a laser gyroscope. The phosphate glass has loss around 0.1 m^{-1}, while YAG is greater than 0.2 m^{-1} [5].

Additionally, the pump absorption band for phosphate glass is wider and has less fine structure than Nd^{3+}:YAG (Figure 4.1) due to the amorphous structure of the host. This makes the pump wavelength requirement less stringent and less demanding in temperature control of the pump diode wavelength. There is also a possibility of having the pump

tuned to 810 nm (a flatter part of the Nd^{3+} absorption curve). This will give greater tolerance to changes in pump wavelength. Furthermore, the lower melting point reduces the production costs of the glass.

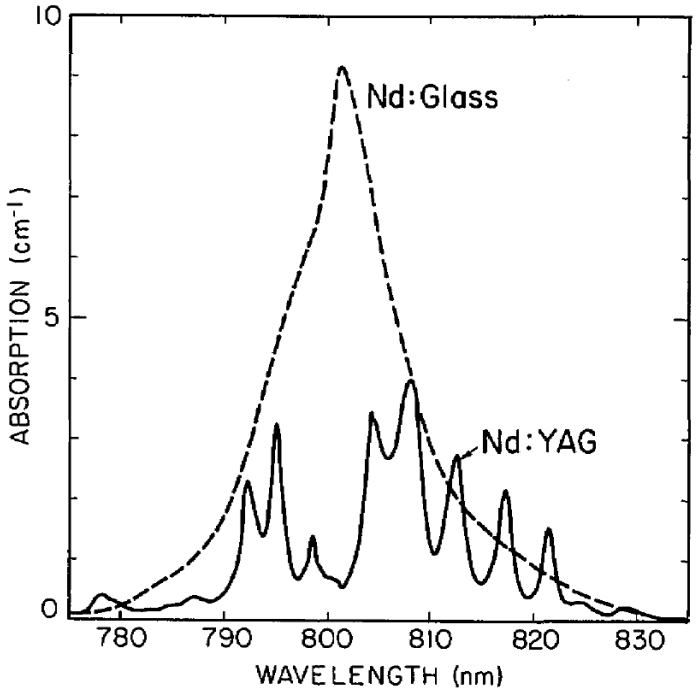

Figure 4.1: Absorption band of 0.7 % doped Nd^{3+}:YAG and a 3 % doped Nd^{3+}:phosphate glass [5].

The first glass laser was built in 1961 using Nd^{3+} doped barium crown glass [47]. It was found that the quantum efficiency decreased as the doping concentration increased above 2 %wt. The quest for materials that can be doped at higher concentration primarily for nuclear fusion using lasers, led to use of phosphate glass [48]. Subsequently, the first continuous wave Nd^{3+}:phosphate laser was demonstrated in 1979 [49] using a 514.5 nm pump wavelength derived from an argon laser. With advances in laser diode technology, diode pumping has replaced bulky argon ion lasers [5].

4.2 The Gain Medium

Glass contains large structural randomness compared to crystals which exhibit translational symmetry. In a glass, the crystal field experienced by optically active dopant ions varies significantly from one site to another. This causes significant inhomogeneous broadening even at room temperature. On the other hand, crystals have a regularly repeating

crystalline lattice structure which leads to predominantly homogeneous broadening arising from the electron-phonon interaction at room temperature. The ratio of homogeneous to inhomogeneous broadening varies between 0.16 and 1.9 for phosphate glasses [50] . This large variability is due to random defects in different glass compositions.

A typical phosphate glass is made from metal oxides combined with P_2O_5. The chemical formula for phosphate glass is: $xP_2O_5 - yAl_2O_3 - zM_2O$ $(M = Na, Li, K)$, or $xP_2O_5 - yAl_2O_3 - zMO$ $(M = Mg, Ca, Sr, Ba)$ where x, y, z are the number of moles of the respective compounds. The molar concentration of P_2O_5 and metal oxides varies over a huge range, giving it a wide range of properties depending on the chosen composition [51], [52]. Table 4.1 shows a range of spectroscopic values for neodymium doped phosphate and other type of glasses. Phosphate glasses are known to offer the best overall combination of properties such as refractive index homogeneity, small cross section for seeds and inclusions, good chemical durability and low attenuation at the lasing wavelength and little or no optical birefringence when compared with other glasses [53].

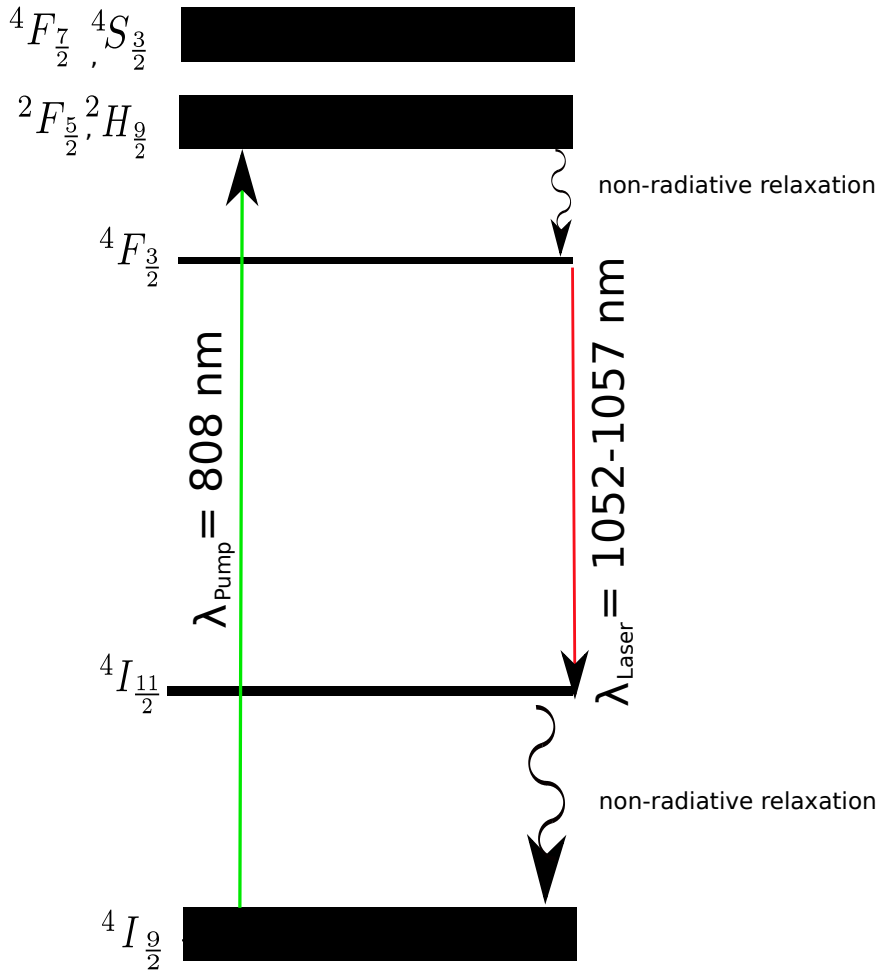

Figure 4.2: Schematic energy level structure for the Nd^{3+} ion.

Host glass	**Refractive index**	**Cross section (pm^2)**	**Peak wavelength (nm)**	**Effective linewidth (nm)**	**Radiative lifetime (μs)**
silicate	1.46-1.75	0.9-3.6	1.057-1.088	34-55	170-1090
germinate	1.61-1.71	1.7-2.5	1.060-1.063	36-43	300-460
tellurite	2.0-2.1	3.0-5.1	1.056-1.063	26-31	140-240
phosphate	**1.46-1.63**	**2.0-4.8**	**1.052-1.057**	**22-35**	**280-530**
borate	1.51-1.69	2.1-3.2	1.052-1.062	34-38	270-450
beryllium fluoride	1.28-1.38	1.6-4.0	1.046-1.050	19-29	460-1030
aluminum fluoride	1.39-1.49	2.2-2.9	1.049-1.050	28-32	540-650
heavy metal fluoride	1.50-1.56	2.5-3.4	1.048-1.051	25-29	360-500
chloride	1.67-2.06	6.0-6.3	1.062-1.064	19-20	180-220
fluoro phosphate	1.41-1.56	2.2-4.3	1.049-1.056	27-34	310-570
chloro phosphate	1.51-1.55	5.2-5.4	1.055	22-23	290-300
sulfide	2.1-2.5	6.9-8.2	1.075	21	64-100
oxysulfide	2.4	4.2	1.075	28	92

Table 4.1: Spectroscopic properties of the ${}^4F_{\frac{3}{2}} \rightarrow {}^4I_{\frac{11}{2}}$ transition of Nd^{3+} for various glass hosts at 295 K [8].

Nd^{3+} lifetime	330 μs
Lasing cross-section at 1.054 μm	3.8 x 10^{-20} cm^2
Density	2.85 g/cm^3
Refractive index	1.55
Thermal expansion coefficient	$8.0 \times 10^{-6} K^{-1}$

Table 4.2: Some relevant properties of Nd^{3+} doped phosphate glass supplied by MolTech GmbH.

Neodymium ions have a 4f valence shell which is shielded by 5s and 5p outer electrons and therefore yield sharp line spectra even when doped into solid state media such as bulk crystals and to lesser degree, phosphate glasses. Optical pumping may be provided by an 808 nm AlGaAs laser diode which excites the ${}^4I_{\frac{9}{2}} \rightarrow {}^2F_{\frac{5}{2}}$ intra-configurational transition of Nd^{3+}. Subsequently, rapid non-radiative relaxation occurs which populates the ${}^4F_{\frac{3}{2}}$ upper lasing level. The terminating laser state ${}^4I_{\frac{11}{2}}$ is located at $\sim$2000 cm^{-1} above the ground multiplet and is therefore unpopulated at room temperature [54]. It also has the desirable feature of rapid relaxation to the ground multiplet which assists in maintaining the population inversion.

The phosphate glass used in this thesis was purchased from Molecular Technology GmbH (Berlin) (MolTech) with a dopant concentration of 4×10^{20} Nd^{3+} ions/cm^3 (4 %wt). This concentration was chosen because of the work done by Kozlovsky et al.[5]. The supplied glass had 1 mm thickness with an anti-reflection coating for the lasing wavelength. Table 4.2 shows the properties of the phosphate glass as supplied by the manufacturer.

Using the information from Table 4.2 it is possible to calculate the available gain (G) using the formula:

$$G = e^{(\sigma_e N_2 - \sigma_a N_1)z} \tag{4.1}$$

where σ_e is the laser emission cross section and σ_a is the absorption cross section. N_2 and N_1 are the number of electrons in the upper and lower lasing levels. z is the thickness of the glass. Due to the four level nature of the system, the absorption due to the lower lasing level can be ignored, and the gain can be approximated by:

$$G \approx e^{\sigma_e N_2 z} \tag{4.2}$$

The amount of gain available from this material is large even at low inversion levels. For example, at an inversion level of 20 %, the gain is 35 % for a 1 mm thick sample. Therefore the amount of gain even at this pumping level is more than enough to overcome typical cavity losses. These are normally around the 2-3 % level.

4.3 A Linear Laser Design

The ultimate aim of this project is to build a rotation sensing, bi-directional ring laser. To achieve this, the first step is to build a linear laser from the proposed gain medium to ensure it can lase at a reasonable pump power before venturing into the more complex ring design.

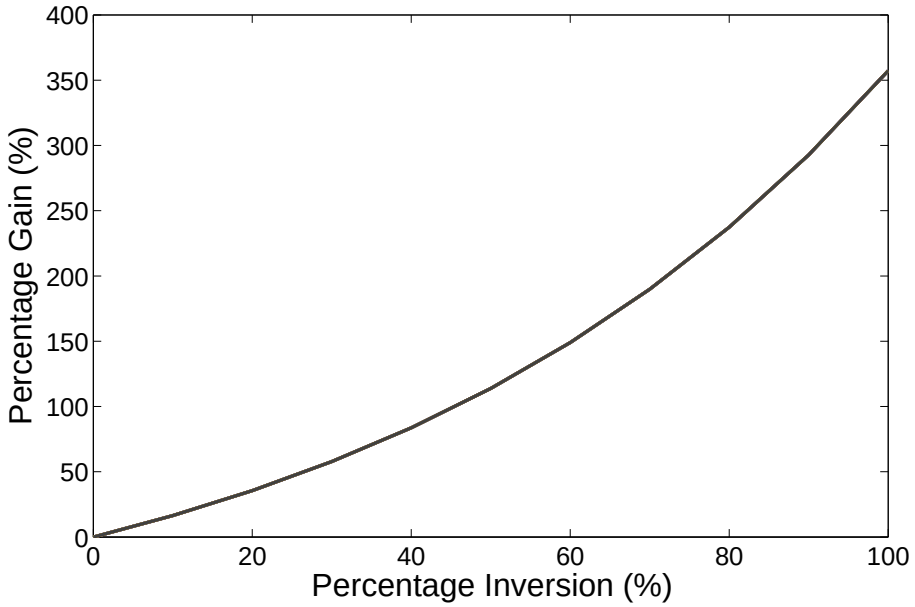

Figure 4.3: Percentage gain versus inversion for a 1 mm thick phosphate glass sample with a Nd^{3+} concentration of 4×10^{20} ions/cm^3.

A simple plano-concave resonator was chosen for the linear cavity. This design is preferred due to its ease of alignment compared with other cavity designs.

The radius of curvature (ROC) of the concave mirror used was 7.5 cm. The stability of the cavity was determined using the appropriate ray transfer matrix [55] for the cavity:

$$\begin{bmatrix} h_o \\ \theta_o \end{bmatrix} = \begin{bmatrix} A & B \\ C & D \end{bmatrix}^n \begin{bmatrix} h_i \\ \theta_i \end{bmatrix} \tag{4.3}$$

Where h_o and θ_o are the output ray height and angle. As a ray travels through the sequence of optics it is transformed from h_i and θ_i by the $ABCD$ matrix. n is the number of round trips. In a resonating cavity n tends to infinity as the light bounces around the cavity. The $ABCD$ matrix is given by matrix multiplication of individual elements in the cavity. We define each element in our cavity as: F_1 the system matrix for flat mirror, C_1 the system matrix for the concave mirror, D_1 the translation matrix for arm length K_1.

$$F_1 = \begin{bmatrix} 1 & 0 \\ 0 & 1 \end{bmatrix} C_1 = \begin{bmatrix} 1 & 0 \\ \frac{-2}{R_1} & 1 \end{bmatrix} D_1 = \begin{bmatrix} 1 & K_1 \\ 0 & 1 \end{bmatrix} \tag{4.4}$$

where $R_1 = 7.5$ cm is radius of curvature of the concave mirror and K_1 is the length of the cavity. Over an entire round trip of the cavity the $ABCD$ matrix will be $D_1F_1D_1C_1$. This is equal to:

$$\begin{bmatrix} A & B \\ C & D \end{bmatrix} = \begin{bmatrix} 1 - \frac{4K_1}{7.5} & 2K_1 \\ -\frac{2}{7.5} & 1 \end{bmatrix} \tag{4.5}$$

We impose the standard stability criterion -1 $<\frac{1}{2}(A+D) < 1$ [55] to solve for K_1. This gives $K_1 \leq 7.5$ cm (ROC of the mirror), so the cavity length has to be no longer than 7.5 cm for stable laser oscillation to occur.

To estimate the length of the cavity we look at the spot size and diffraction losses. The cavity parameters can be expressed it terms of g_1 and g_2:

$$g_1 = 1 - \frac{K_1}{R_1} \qquad \text{and} \qquad g_2 = 1 - \frac{K_1}{R_2} \tag{4.6}$$

where R_1 and R_2 are the radius of curvature of the mirrors. Since $R_1 = \infty$, g_1=1, let g_2=g, so the spot size is defined by these two standard equations [23]:

$$\mathrm{w}_{flat} = \sqrt{(\frac{K_1\lambda}{\pi})\sqrt{\frac{g}{1-g}}} \tag{4.7}$$

$$\mathrm{w}_{curved} = \sqrt{(\frac{K_1\lambda}{\pi})\sqrt{\frac{1}{g(1-g)}}} \tag{4.8}$$

where w_{flat} and w_{curved} are the Gaussian beam waists on the flat and curved mirrors respectively and λ is the lasing wavelength. Equations 4.7 and 4.8 were used to generate the Figures 4.4 and 4.5. Figure 4.4 shows that the beam spot size increases rapidly as the cavity length increases then plateaus at value around 2 to 6 cm and subsequently decreases again.

Similarly, in Figure 4.5 the spot size on the concave mirror shows the least change for a cavity length between 2 and 6 cm. The greatest mechanical tolerance will be achieved by building a laser between 2 to 6 cm. The laser was built with a cavity length of 3 cm since a smaller cavity size is easier to align. Furthermore, the modal volume that is required to be pumped depends on the position of the gain medium. It is lowest when the medium is positioned close to the flat mirror and largest when it is close to the concave mirror.

4.3.1 Construction and Laser Output.

Figures 4.6 and 4.7 show the experimental layout of the laser. The dielectric cavity mirrors were bought from CVI Melles Griot . Mirror M1 (PR1-1053-99-1037-0.075C) is a concave 1 % output coupler with a radius of curvature of 7.5 cm. Mirror M2 (SWP-0-R1053-T800-PW1025-C) is a dichroic high reflective coated planar mirror at 1053 nm on one side. The other side of (M2) is anti reflection coated for the pump wavelength of 808 nm.

The gain medium (G) is placed near the planar mirror. The beam diameter is smallest

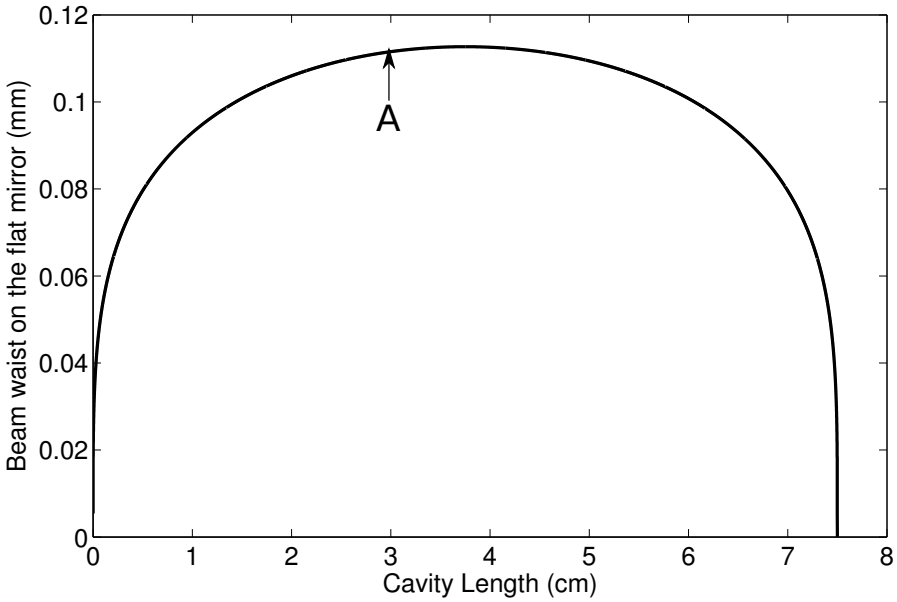

Figure 4.4: Beam waist on the flat mirror of a plano-concave cavity with a concave mirror ROC of 7.5 cm. The cavity length built is marked by point A.

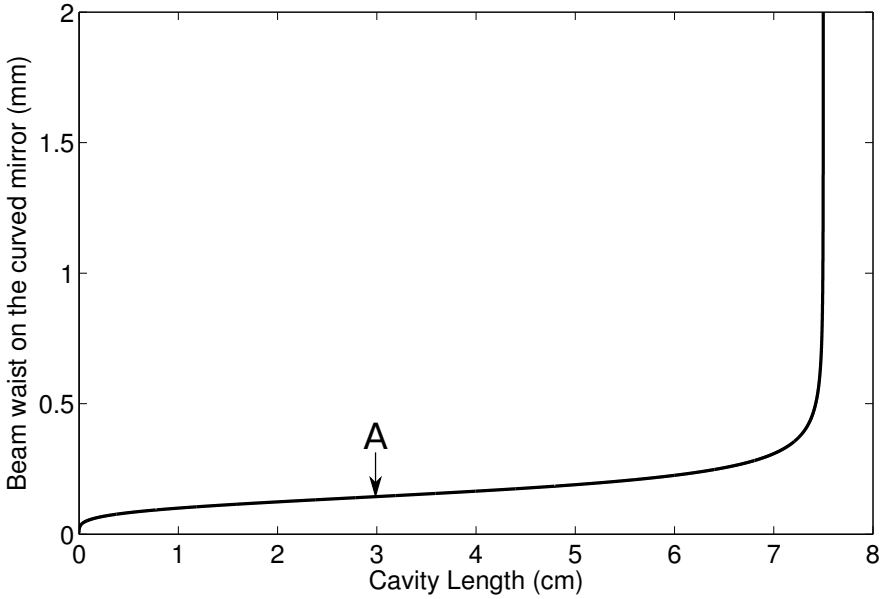

Figure 4.5: Beam waist on the concave mirror of a plano-concave cavity with a concave mirror ROC of 7.5 cm. The cavity length built is marked by point A.

at this point, so it is easier to achieve laser action by mode matching the focused pump beam and the TEM_{00} modal volume.

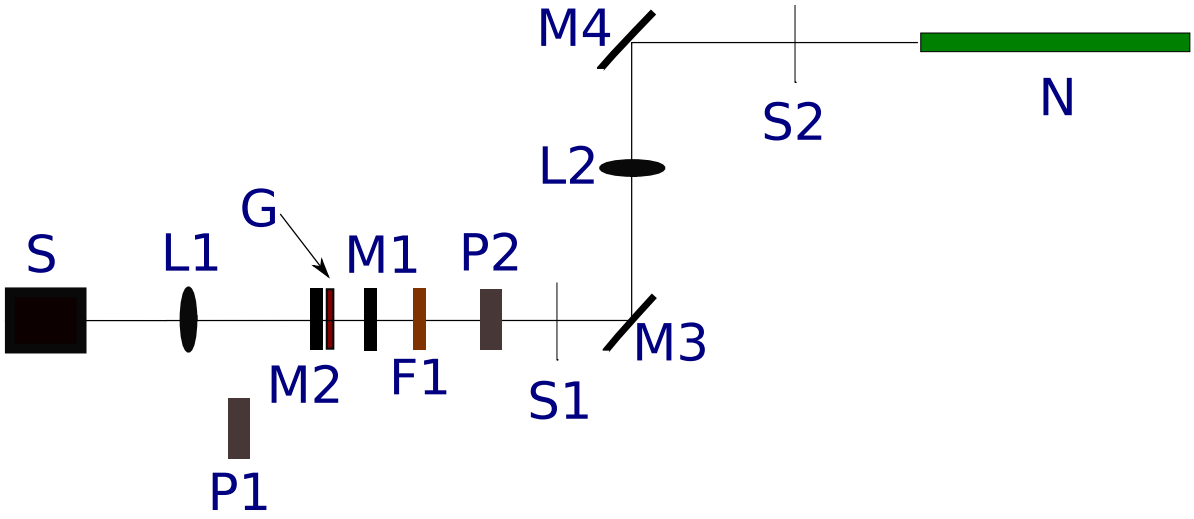

Figure 4.6: Schematic of the constructed Nd^{3+}:Phosphate linear laser. Where L1, L2-are lenses, M1 is a concave cavity mirror (1 % output coupler), M2 is a dichroic planer cavity mirror, M3 is a tuning mirror, F1 is a filter, G is the gain medium, S is the diode pump laser, P1 is a high power meter, P2 is a low power meter, S1, S2 are screens and N is a green He-Ne laser.

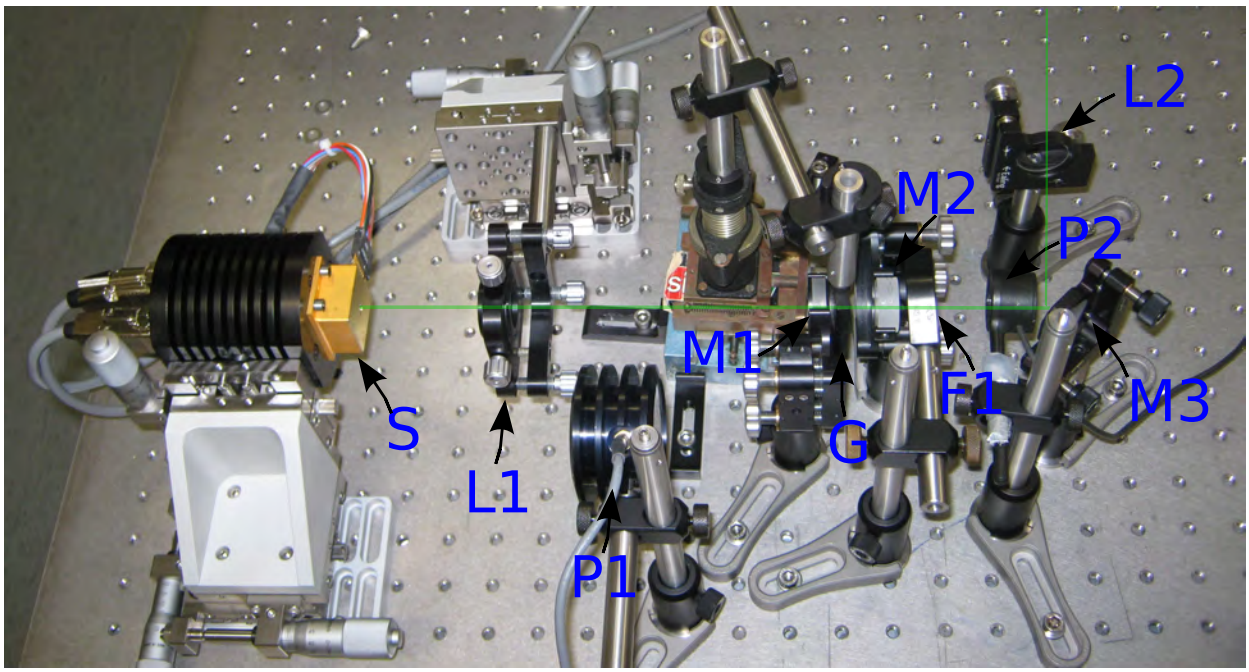

Figure 4.7: Photo of the constructed Nd^{3+}:Phosphate linear laser. Where L1, L2 are lenses, M1 is a planar cavity mirror (1 % output coupler), M2 is a dichroic concave cavity mirror, M3 is a tuning mirror, F1 is a filter, G is the gain medium, S is a diode laser, P1, P2 is laser power meters.

The pump laser was a AlGaAs laser diode from Intense^{TM} (3030-HHL-TEC-FAC-80803). The diode has a maximum power output of 3.16 W with a wavelength of 807.2 nm with a FWHM of 0.2 nm. Figure 4.8 shows the wavelength profile of the diode at 25^{o}C. The wavelength emitted ranges from 806-808 nm depending on the exact diode temperature. However the Nd^{3+}:phosphate glass has a wide absorption band that is particularly suited in this situation, as shown in Figure 4.1. It was found that the best working temperature for the diode is 23.6 degrees at a given power. This was done by changing the temperature of the diode while keeping the power constant to obtain maximum power output from the Nd^{3+}:phosphate laser. Having a lower temperature decreases the wavelength of the pump diode laser making it more aligned with the peak absorption of Nd^{3+}:phosphate.

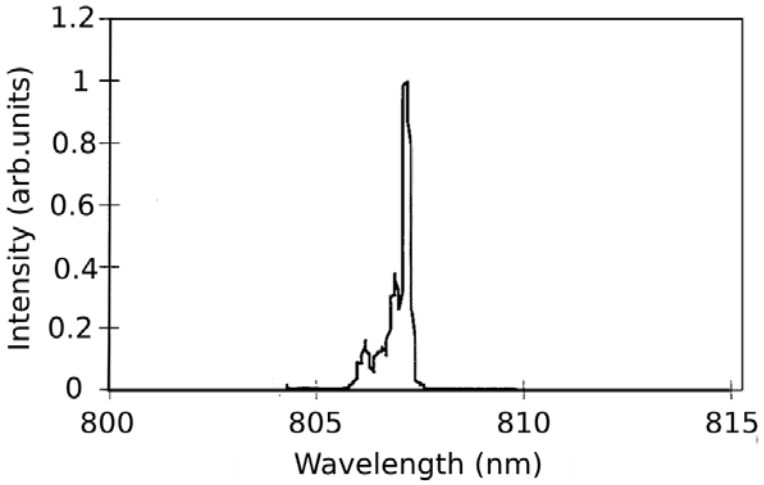

Figure 4.8: Wavelength distribution of the Intense laser diode at 25^o C. Information supplied by the manufacturer.

The diode was bought with a TEC (thermoelectric cooler) to allow operation at constant temperature. A fast axis collimator was built into the diode to compensate for the high divergence along the fast axis. It is a tiny rod mounted on the aperture of the laser diode and converges the beam only on one axis. The output from the beam is put though a 5 cm focal length lens and focused into the gain medium.

Precise alignment of the laser cavity is critical for the stability conditions to be maintained. Figure 4.6 shows a schematic of the experimental arrangement. A green laser (N) is reflected through mirror (M4) and (M3) along the axis of the cavity. The laser is reflected from the back surface of mirror (M1) on to the screen (S2) which has a small hole equal to the size of the alignment beam. Mirror (M2) is then added and again the laser is reflected through to screen (S2). The alignment beam diverges due to the curved surface

of mirror (M2). The diverged beam can be seen in the screen (S1) which also has a small hole equal in diameter to the alignment beam. Once the diverged beam was centred on the screen (S1) it was removed to allow for the beam to travel through. Then the lens (L2) was added to compensate for the divergence. When the back reflected beams from (M1) and (M2) overlap with the incoming alignment beam both mirrors are parallel. The pump laser diode (S) and the lens (L1) were then centred along the alignment beam path. A IR fluorescent card (Thorlab VRC2) was placed between the mirrors (M1) and (M2). The pump diode (S) was turned on just above the diode lasing threshold and aligned so that the spot on the fluorescent card from the laser diode overlapped with the beam from the alignment laser. Finally, the 1 mm gain medium (G) was placed in the cavity along with screen (S1). It produced a circular interference pattern on the screen (S1) from reflection on the front and back surfaces of the gain medium. The gain medium was moved until the center of the pattern overlapped with the alignment beam. This indicated the gain medium was perpendicular to the lasing axis. The diode power was then increased

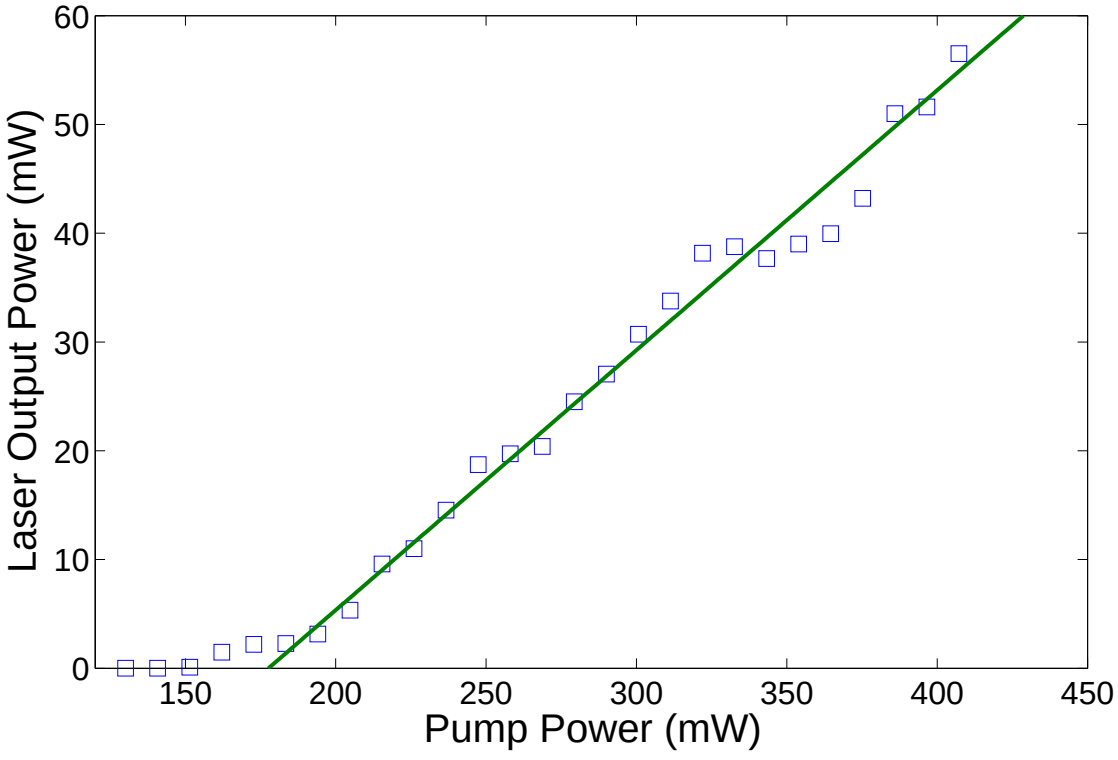

Figure 4.9: The measured laser output power of the Nd^{3+}:phosphate linear laser versus diode pump power using a 1 % output coupler (M2).

until lasing occurred. Finally, mirrors (M1),(M2) and lens (L1) were iteratively adjusted further to achieve maximum laser output power. The output from the laser is shown in

Figure 4.9. From this plot, we infer a slope efficiency of 24 %. The lasing threshold was 180 mW. Also, between 150 nm to 180 nm there is a build up of fluorescence just before lasing occurs. The values displayed on the graph are measured directly from power meters P1 and P2.

4.3.2 Polarisation Stability.

The laser was linearly polarised but the axis of the polarisation changed over time. The preferred polarisation angle is somewhere between 110 and 120 degrees (at 0 degrees the polariser is perpendicular to the optical table), followed by 12 and 22 degrees. The angle values are given as ranges due to the changing polarisation axis.

This experiment was done by placing a polariser in front of the laser beam. Then the polariser was rotated. Maximum and minimum outputs were recorded on the photo diode. The polarisation angle constantly changed between the angles described above, but most of the time they stayed in one axis long enough to carry out the measurements.

This behaviour is caused by the laser not having a unique least possible loss state. There are two possible least losses states at 110-120 degrees and 14-22 degrees. When losses in the cavity at different axes are close to each other, as displayed in this laser, any small change in loss causes it to change to another axis. Continual changes in the polarisation axis leads to instability in the intensity of the laser. Having a polariser in the cavity could therefore improve the system in terms of stability, but it would also increase the loss in the cavity.

4.3.3 Transverse Laser Modes.

It was possible to observe a wide range of traverse laser modes by changing the laser diode power and alignment. Different alignment varied the losses, favouring various TEM modes. TEM_{00} was our preferred mode since it is the easiest mode to work with especially when overlap of two beams are needed in the ring laser design. The largest two transverse modes that were produced are shown in Figure 4.10.

4.4 Saturation of the Gain Medium

An experiment was performed to test for any evidence of gain saturation over the range of usable pump powers. This gave an indication of how much gain was available via an

Figure 4.10: Highest order transverse modes produced by the Nd^{3+}:phosphate laser. Different alignment of the laser diode produced these modes.

experimental procedure. We removed the output coupler (M1) while keeping other parts of the linear laser intact. The fluorescence from the gain medium is collimated by lenses (L2) and (L3) into the spectrometer. A neutral density filter (N) is added to prevent saturation of the detector (D). The experimental set up is shown in Figure 4.11. The

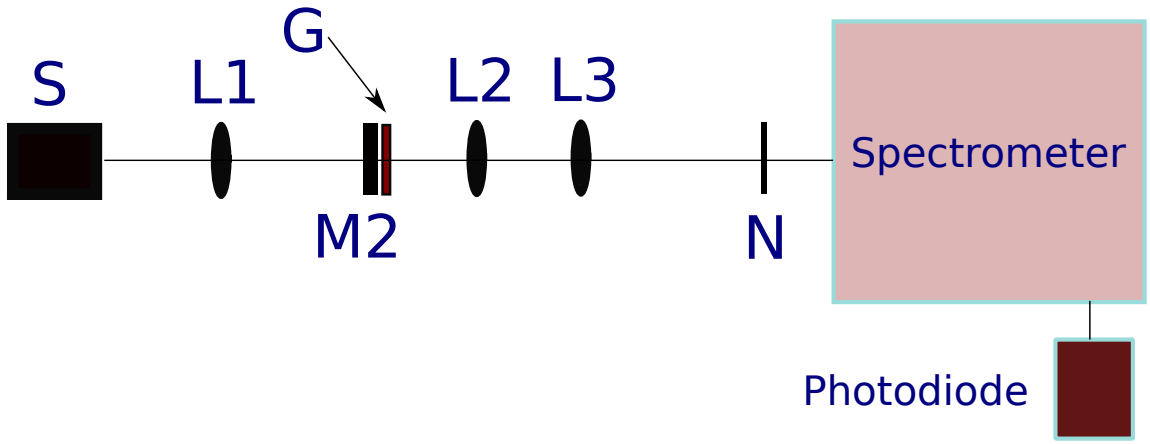

Figure 4.11: Experimental set-up to measure the fluorescence spectrum at various powers to observe saturation of the lasing transition. L1 is a lens, M2 is a dichroic concave cavity mirror, G is the gain medium, S is the pump diode laser. L2 and L3 are lenses used to collimate the light into the spectrometer. N is a neutral density filter.

$^4F_{\frac{3}{2}} \rightarrow ^4 I_{\frac{11}{2}}$ fluorescence spectrum of the gain medium has been measured at increments of 20 mW over a power range between 130 mW and 450 mW. Figure 4.12 shows the spectra obtained from the experiment. The peak fluorescent intensity (at 1053 nm) is plotted as a function of excitation power in Figure 4.13. This figure shows there is no tendency to saturate for the powers tested. This result indicated that the gain medium was suitable for the construction of the potentially lossier ring cavity.

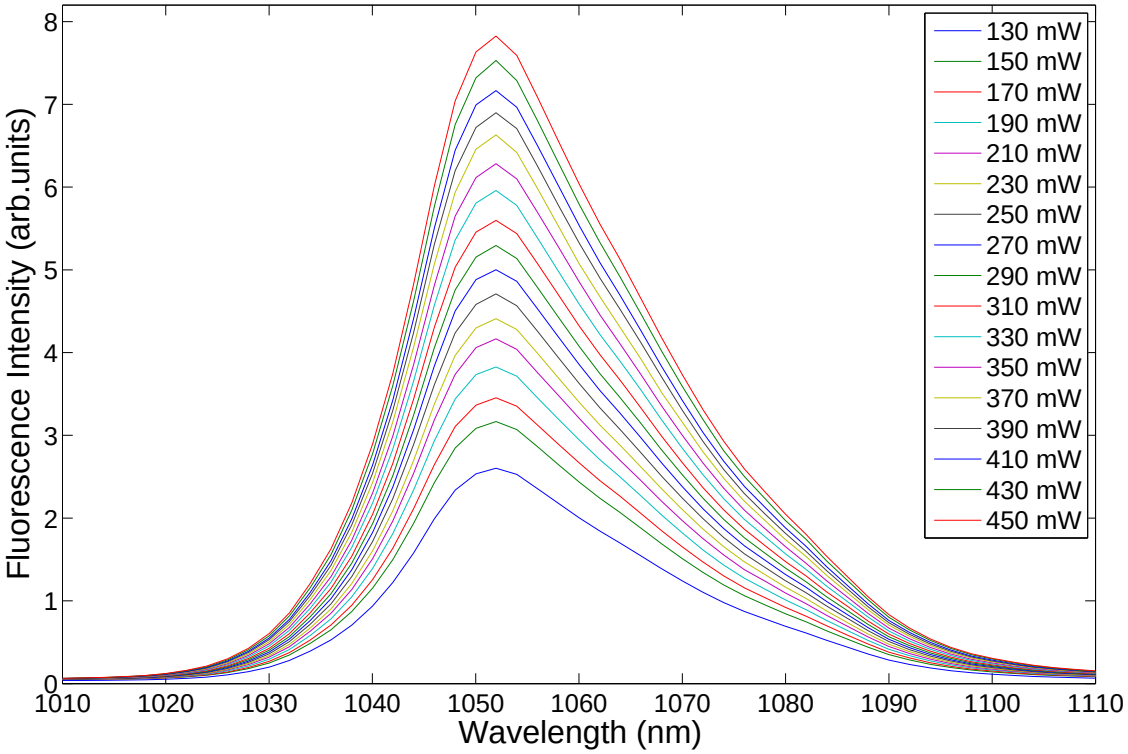

Figure 4.12: Room temperature ${}^4F_{\frac{3}{2}} \rightarrow {}^4 I_{\frac{11}{2}}$ fluorescence spectrum of the neodymium doped phosphate glass gain medium. The spectra have been measured for pump powers between 130 and 450 mW, at an increment of 20 mW.

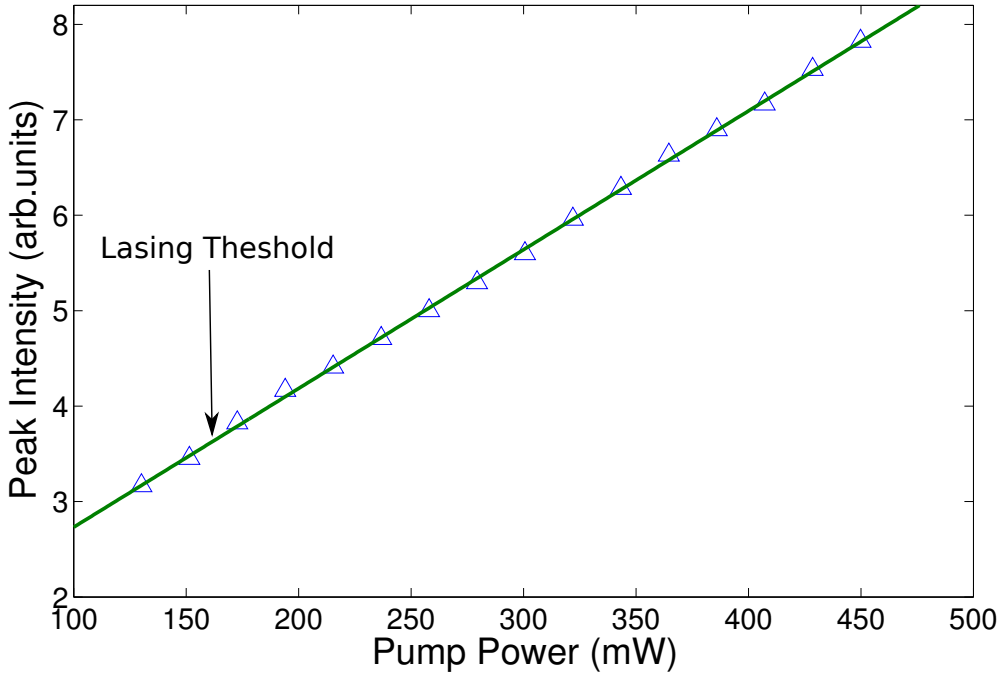

Figure 4.13: Peak fluorescence intensity versus pump power for the Nd^{3+}:phosphate glass gain medium. No evidence of gain saturation is present.

4.5 L-Cavity Design

As an evolutionary step towards building a ring cavity, a three mirror folded cavity in the shape of an 'L' was constructed. The additional concave cavity mirror was implemented at 45^o which increased the alignment complexity.

4.5.1 L-Cavity Stability Analysis.

As with the linear cavity design, the first step is to determine the cavity stability prior to construction. An analysis is required to determine an appropriate range of arm lengths. The ray transfer matrix defined in equation 4.3 is used. The translation and system matrices are: F_1,F_2 for the two planar cavity mirrors, C_1 for the concave mirrors and D_1,D_2 for translation over arm lengths H_1 and H_2.

$$F_1\&F_2 = \begin{bmatrix} 1 & 0 \\ 0 & 1 \end{bmatrix} C_1 = \begin{bmatrix} 1 & 0 \\ \frac{-2}{R} & 1 \end{bmatrix} D_1 = \begin{bmatrix} 1 & H_1 \\ 0 & 1 \end{bmatrix} D_2 = \begin{bmatrix} 1 & H_2 \\ 0 & 1 \end{bmatrix} \tag{4.9}$$

where R=7.5 cm is the radius of curvature. Over a round trip through the cavity the $ABCD$ matrix will be $F_2D_1C_1D_2F_2D_2C_1D_1$. This is equal to:

$$\begin{bmatrix} A & B \\ C & D \end{bmatrix} = \begin{bmatrix} \Omega & H_1 + H_1\Omega - 2K_2(\frac{4H_1}{15} - 1) \\ \frac{32H_2}{225} - \frac{8}{15} & H_1(\frac{32H_2}{225} - \frac{8}{15}) - \frac{H_2}{15} + 1 \end{bmatrix} \tag{4.10}$$

Where Ω is defined as:

$$\Omega = 8K_2(\frac{\frac{H_1}{15} - 1}{15}) - \frac{8H_1}{15} + 1 \tag{4.11}$$

As before, we impose a stability criterion -1 $<\frac{1}{2}$(A+D) < 1 [55] to solve for H_2 and H_1. Therefore H_1 and H_2 must be less than 3.5 cm.

Figure 4.14 shows the set-up of the L-cavity. The pump is transmitted through a dichroic planar mirror (M2). The gain medium (G) is placed closed to (M2) where the mode volume is the smallest. The mirror (M3) is high reflecting at 45^o and s-polarised (Y1-1037-45S-0.075C). s-polarising mirrors are used as they have the lowest reflection loss compared to un-polarised and p-polarised mirrors. s-polarising mirrors have higher reflectivity than other polarisations due to the angle of the mirror approaching Brewster angle. Mirror (M2) is dichroic with a high reflective (HR) coating at the lasing wavelength inside the cavity and an anti reflection coating for the pump beam (SWP-0-R1053-T800-PW1025-C). Finally, mirror (M1) is a planar mirror with a high reflective coating (JLM-1064-0-1037).

4.5.2 Alignment Process.

The alignment process is more critical in the L-cavity than the previous design, mainly due to poor transmission of the alignment laser through the dielectric mirrors and astigmatism induced by the concave mirror used at 45^0. A polariser was placed in front of the green He-Ne laser and rotated to give the maximum reflection from the front surface of the curved mirror (M3). The alignment beam travelling through (M1), (M3) and (L1) is back reflected by (M5). The beam diverges as it travels through (M3). (L1) is placed in such a way that it focuses onto (M5). The distance between (L1) and (M5) was adjusted so a spot was formed around the hole on the screen (S2). The beam travelling through (M1) is reflected by the curved surface of (M3) onto (M2). (M2) back-reflects the beam back through (M3) onto the screen (S1). M4 is added to stop the beam from getting blocked by the screw on the mount (see Figure 4.15). On the screen there are two spots. One spot is back-reflected from (M2), the other is back-reflected from (M5) and reflected from the curved surface of (M3). (M2) is adjusted so that both beams are combined. The laser diode was turned on at very low incident power. A fluorescent IR card (Tholab VRC-2)

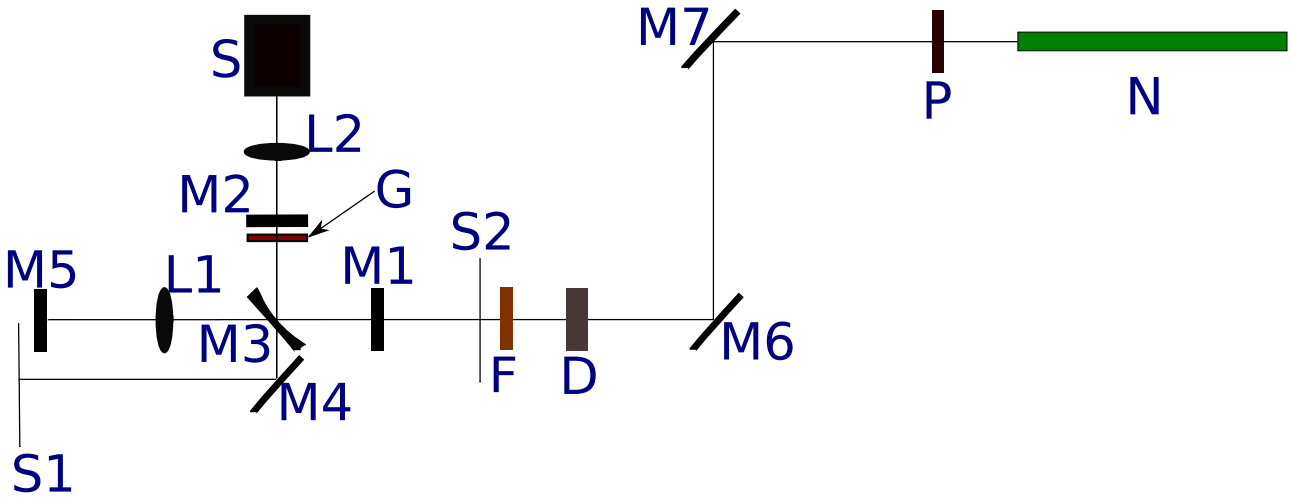

Figure 4.14: Schematic of the constructed Nd^{3+}:phosphate L-cavity laser. The laser cavity is formed by mirrors M1, M2 and M3. S is the 808 nm pump laser diode. Where mirrors M5, M6 and M7 are fold mirrors for assisting with the alignment. M3 (output coupler) is an s-polarised concave mirror with radius of curvature of 7.5 cm. M1 (output coupler) and M2 are planar cavity mirrors. L1, L2 are lenses with focal lengths of 12.5 cm and 5 cm. S1 is a plane white screen. S2 is a screen with a small hole equal to beam diameter. F is a λ= 1000 nm high pass filter. D is a silicon photodiode.

was placed between (M2) and (M3). (L2) and (S) were adjusted so the spot on the card matches the alignment laser. Finally the gain medium was added. It produced a circular interference pattern on the screen. It was adjusted so that the central maximum of the interference pattern matched the two spots.

4.5.3 Performance of the L-Cavity Laser.

Once the cavity was optimised, the power outputs through the mirrors were measured. The output from the s-polarised (M1) and planar mirrors (M3) is shown in Figure 4.16. The decrease in power for mirror (M1) and increase in power for mirror (M3) at higher pump power is possibly due to a change in transverse mode. The slope efficiency for (M1) is 3.8 %. For (M3) it is 1.3 %. This simply indicates that the mirror (M3) has higher reflectivity than (M1) as more light is reflected than transmitted through it. The lasing threshold was 126 mW of pump power. This laser has a lower lasing threshold and smaller output power than the linear laser due to having higher reflectivity mirrors than the previous design. Also, the reflectivity of (M3) is greater than (M1). This is reassuring as four mirrors with the same specifications as (M3) will be used in the ring cavity.

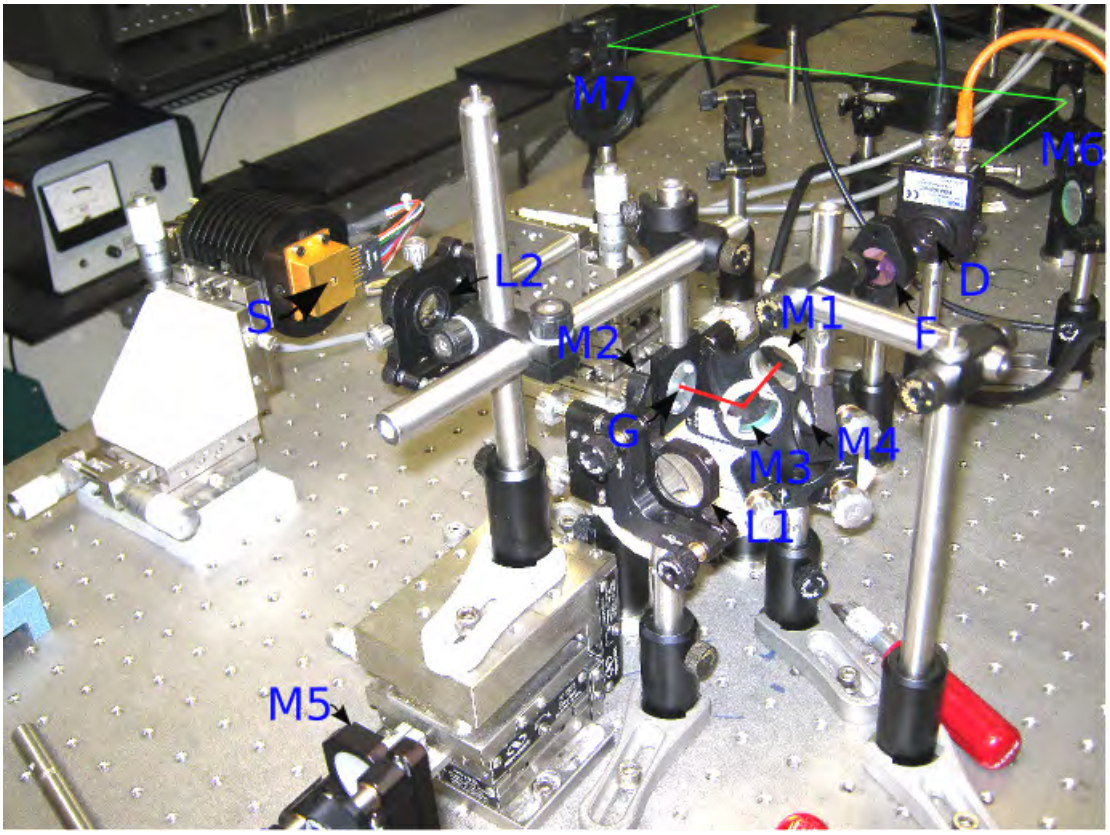

Figure 4.15: Photo of the constructed Nd^{3+}:phosphate L-cavity laser. Where mirrors M5, M6 and M7 are tuning mirrors. M3 (output coupler) is an s-polarised concave mirror with radius of curvature of 7.5 cm. M1 (output coupler) and M2 are planar cavity mirrors. L1, L2 are lens with focal length of 12.5 cm and 5 cm. S1 is a plane white screen. S2 is a screen with a small hole equal to the beam diameter. F is 1000 nm high pass filter. D is a silicon photodiode. S is the 808 nm laser diode

The L-cavity laser shows a fixed polarisation axis parallel to the optical table. The mirror (M3) is s-polarised and has lower loss at s-polarisation. Also, this laser has less fluctuations in intensity than the linear laser, because there is only one axis with the least loss.

4.6 Ring Laser Design

Having successfully constructed the linear and L-cavity lasers, a ring laser was built. The main drawbacks for the ring apart from additional construction requirements is that the gain available is halved as the gain medium is traversed only once per round trip. Also, astigmatism created by the off axis curved mirrors needs to be compensated for in the design and alignment.

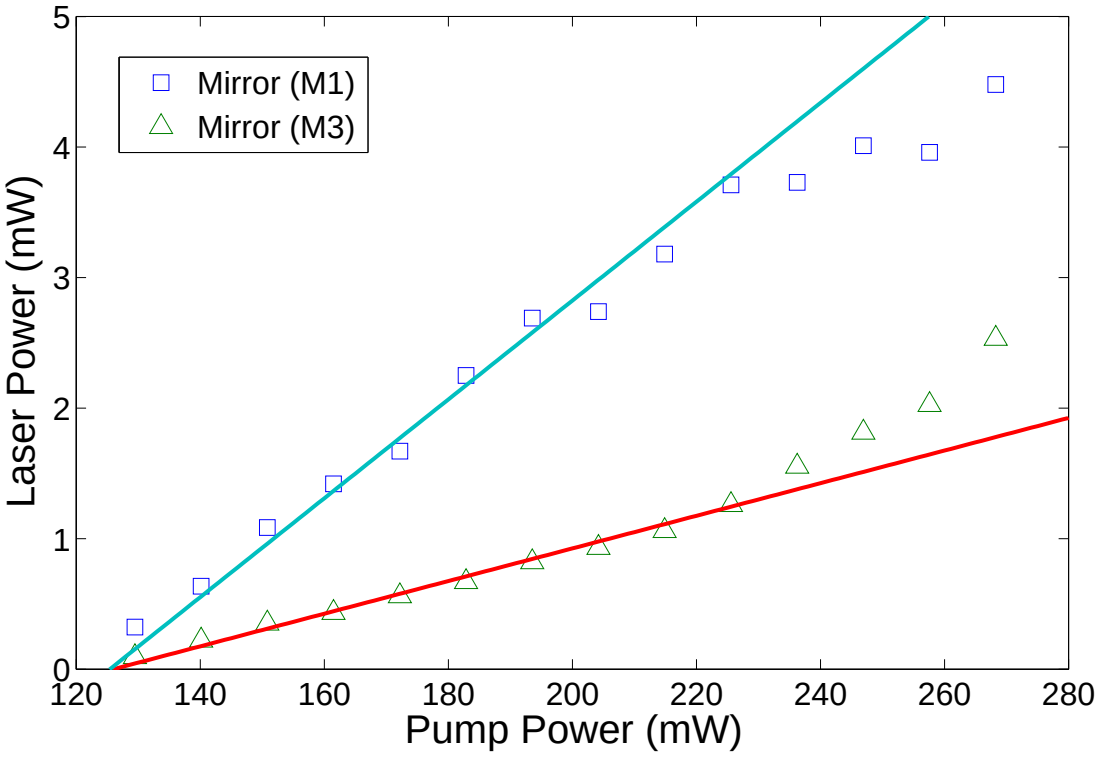

Figure 4.16: The measured laser output power of the Nd^{3+}:phosphate L-cavity laser for various pump diode powers through output coupler mirrors (M1) and (M2).

4.6.1 Largest Mode Volume Pumped by the Diode

Population inversion along the modal volume is the crucial requirement for the ring laser. To achieve population inversion, one needs to know the largest mode volume supported by the current pumping set-up. To test for the largest feasible mode volume, a 6 cm linear laser was built. The gain medium was moved from the flat mirror side towards the curved mirror while the laser power was continually monitored as shown in Figure 4.17. The gain medium was moved until the laser was just about to stop. The pump alignment was then optimised. This process was repeated until the laser stopped working. It was found that the gain medium could be moved up to 5.4 cm from the flat mirror.

Figure 4.18 shows the change in the radius of the beam waist with increasing distance from the flat mirror. This was generated using the equation:

$$W = W_0\sqrt{(1+\frac{Z^2}{Z_0^2})},\ Z_0 = \frac{\pi \times W_o}{\lambda} \tag{4.12}$$

where W_0 is the beam waist at the flat mirror. It is equal to 0.13 cm from equation 4.7. Z is the distance translated from the flat mirror, λ is the wavelength of the laser and Z_0

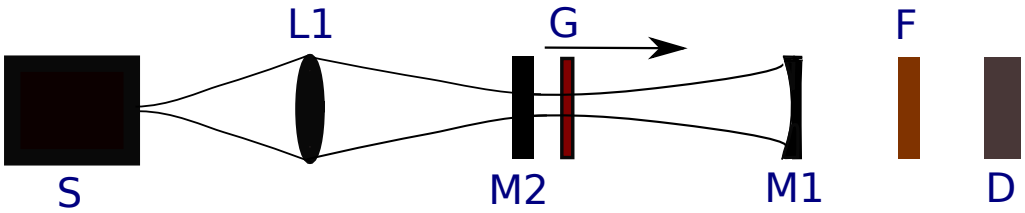

Figure 4.17: The gain medium (G) is moved in the direction of the arrow. L1 is a lens, S is the pump laser diode, M2 is a flat mirror, M1 is a curved mirror, F is a filter and D is the detector

is the Rayleigh length. From Figure 4.18, the distance translated of 5.4 cm corresponds

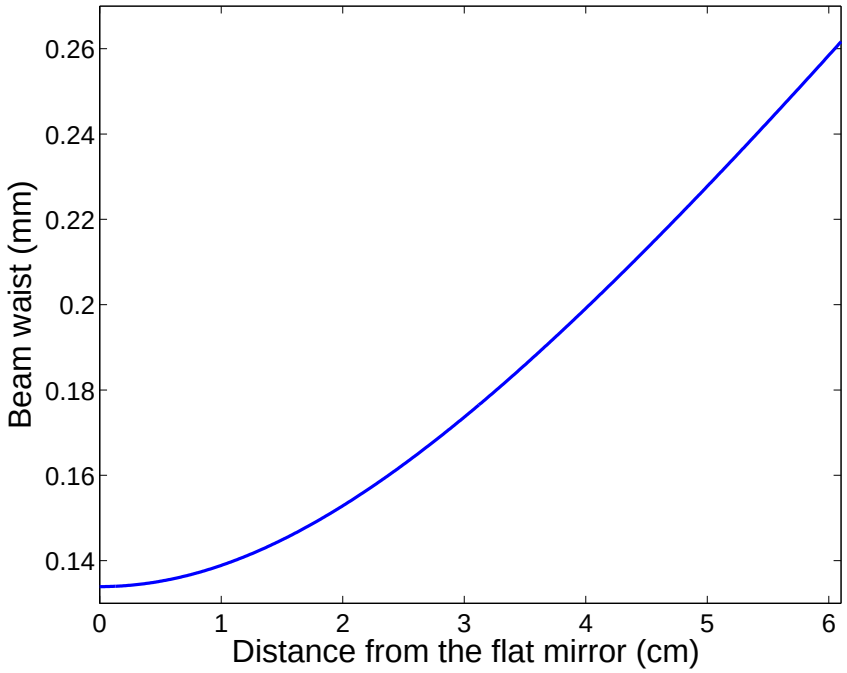

Figure 4.18: Variation of the beam waist along the 6.1 cm cavity. The lowest beam waist is at the flat mirror.

to a beam waist of 0.24 cm. The ring laser group in the University of Canterbury has developed a spread sheet to calculate stability and beam waists for rectangular cavities. It was developed for building the large gas lasers and can be scaled to the small solid state ring. By a trial and error method, a cavity length of 8 cm by 10 cm and radius of curvature of 7.5 cm were chosen, giving a convenient beam waist of 0.11 mm at the middle of the 10 cm arm. The spot size at this point is equal in the out-of-plane and in-plane directions. Since we are able to pump more than twice this value it covers 99.99 % of the Gaussian beam.

4.6.2 Astigmatism Correction.

A concave mirror in a ring cavity at a 45^0 angle causes strong astigmatism on the pump beam. To correct for astigmatism, the ray paths were modelled using an optical design program Zemax. Figure 4.19 shows the incoming beam focused by a plano-convex lens (H) travelling through a concave mirror (C) with radius of curvature of 7.5 cm tilted at 45^0 to the axis. To correct for astigmatism a plano-convex lens (L) with radius of curvature of 7.5 cm is placed on a 45 degree to the pump beam as shown in Figure 4.20. It was found that the plano-convex lens (L) needs to be off-axis to the cavity mirror. To avoid custom making this exact optical component, a standard 15 cm focal length lens was used as an alternative. The radius of curvature of this lens (V) was 7.73 cm. At this radius of curvature Zemax indicates that the difference in distortion is negligible. Also, practically its not possible to sandwich the mirrors together because of the optical mounts. Figure 4.21 shows a realistic scenario used in the pumping setup.

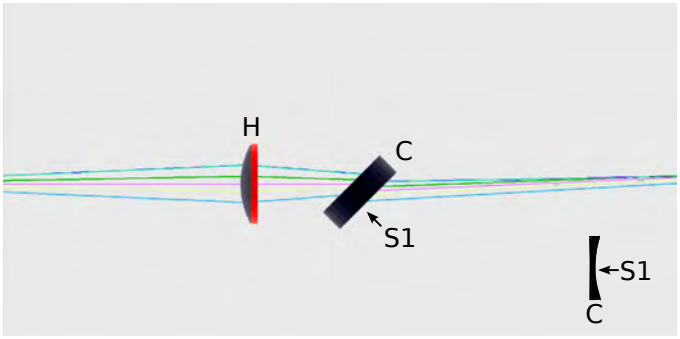

Figure 4.19: Pump beam thorough a plano-convex lens (H) and a angled dichroic concave cavity mirror (C). S1 is the curved surface of the dichroic mirror, which is high reflective coated for the lasing wavelength. The other side of mirror (C) is anti-reflective coated for the pump wavelength. The beam is distorted after travelling through (C). (S1) is the curved surface of the dichoric cavity mirror.

4.7 Aligning a Ring Laser Gyroscope

The schematic and a photo of the constructed Nd^{3+}:phosphate ring laser are shown in Figures 4.22 and 4.23. Elaborate aligning methods are required due to multiple concave surfaces and the number of optics involved. The ring was aligned by tracing a green He-Ne laser around the cavity. The He-Ne laser enters the cavity at mirror (M3) and is reflected around the mirrors (M2), (M1), (M4) and (M4). The problem is that after each reflection, the intensity of the alignment beam decreases. When the laser reaches

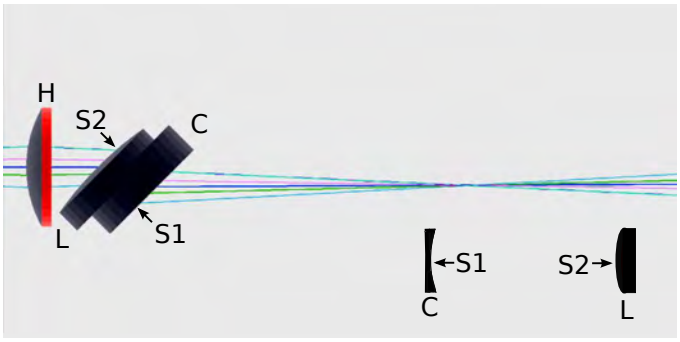

Figure 4.20: Pump beam through a plano-convex lens (H), ideal plano-convex lens (L) with ROC of 7.5 cm and a concave cavity cavity mirror (C). The pump beam is focused without distortion. (S1) is the curved surface of the dichoric cavity mirror (C). (S2) is curved surface of the ideal plano-convex mirror (L).

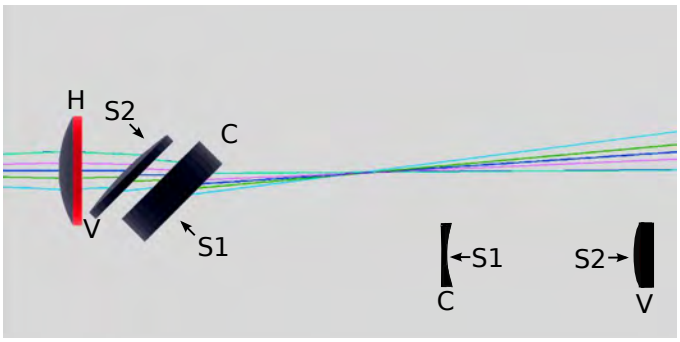

Figure 4.21: Pump beam through a plano-convex lens (H), standard plano-convex lens (V) with ROC of 7.73 cm and a concave cavity cavity mirror (C). The pump beam is focused with acceptable distortion. (S1) is the curved surface of the dichoric cavity mirror. (S2) is the curved surface of the standard plano-convex mirror (L).

the mirror (M3), the beam is too faint to be mapped and go back through (M3). This means that mirror (M3) is not aligned. To align (M3), a retro reflector comprising mirror (M7) and (L2) was set up, where (M7) is a focal length distance away from (L2). This results in back reflection occurring as the incoming beam enters through (M3) and (M2). This back reflection gets mapped with the beam that is travelling around the cavity. The alignment beam through (M4) is used to align (M6), (M5) and (B), so that the clock-wise travelling alignment beam overlaps with the anti-clockwise beam.

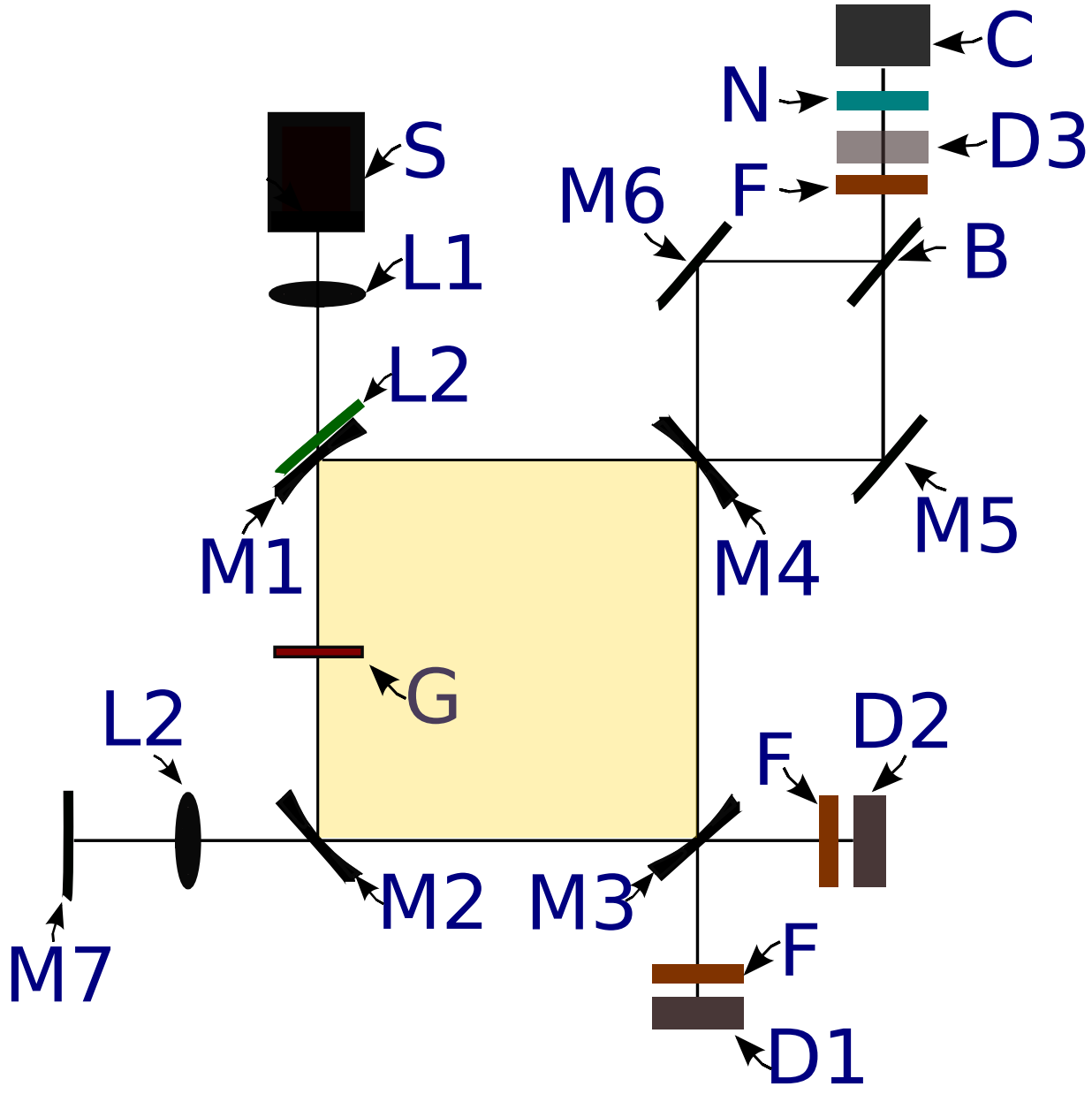

Figure 4.22: Diagram of the layout of the ring cavity. The cavity is formed by mirrors M1-M4, having specifications equivalent to mirror (M3) in the L-cavity laser were used for the ring laser. Having s-polarised mirrors fixes the ring to one polarisation axis. Mirrors (M1-4) are concave mirrors with a radius of curvature of 7.5 cm. F is a long pass filter at 1000 nm. Mirrors (M5-7) are planar mirrors. (B) is a 50:50 beam combiner. The mirror (M7) and lens (L2) are used to back reflect the alignment laser. (S) is the pump laser diode and (L1) is used to focus the beam. (L2) is used to focus the alignment beam. (G) is the gain medium. (D1-3) are photo diodes. (N) is a neutral density filter to prevent camera (C) from saturating.

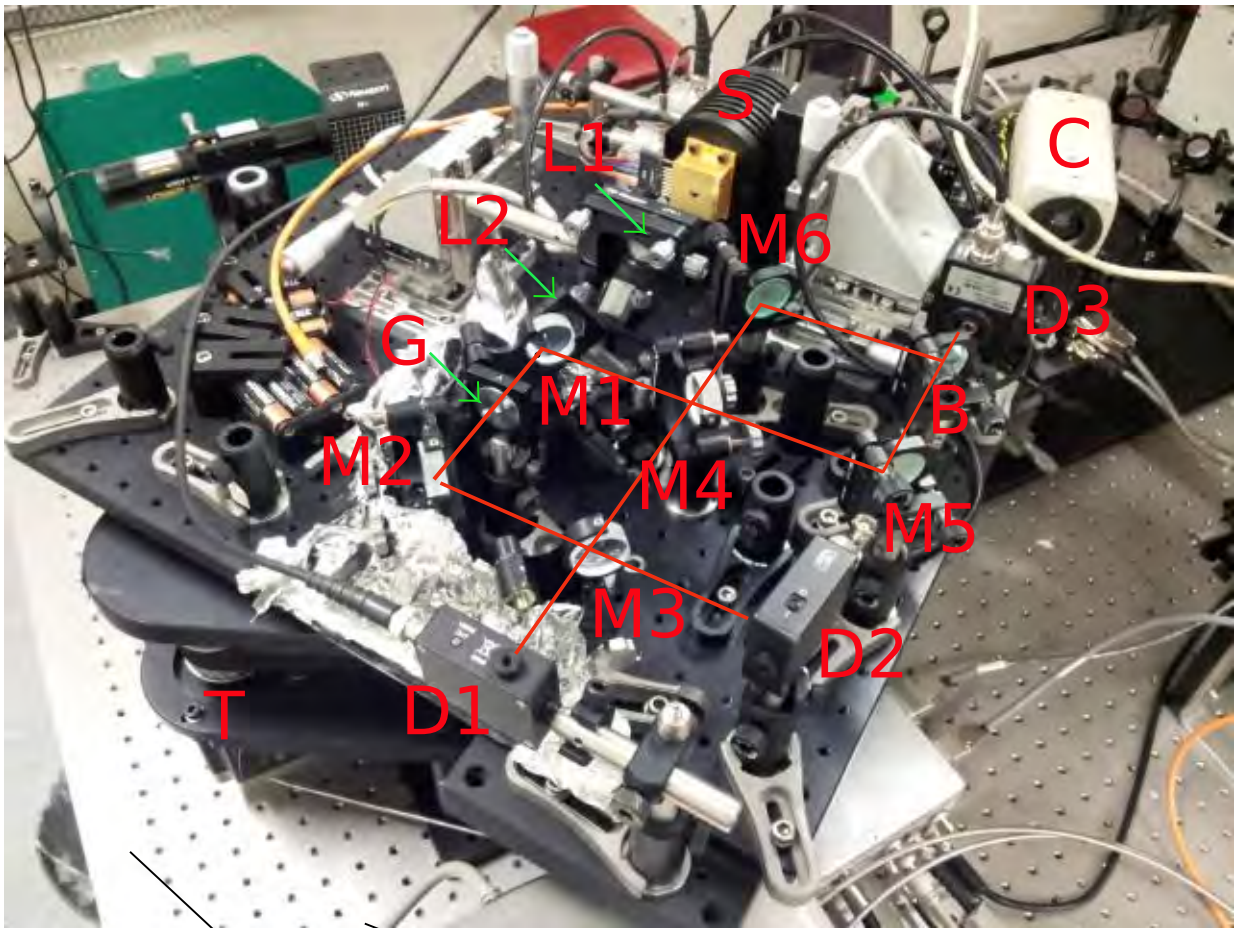

Figure 4.23: The Nd^{3+} phosphate laser gyroscope. Mirrors (M1-4) are concave mirror with radius of curvature of 7.5 cm. Mirrors (M5-6) are planar mirrors. (B) is a 50:50 beam combiner. (L1) is the pump focusing lens and (L2) is a correction lens. (D1-3) are silicon photo diodes. (T) is the stepper motor used to rotate the ring. C is the CCD camera. (S) is the 808 nm laser diode. Finally, (G) is the gain medium.

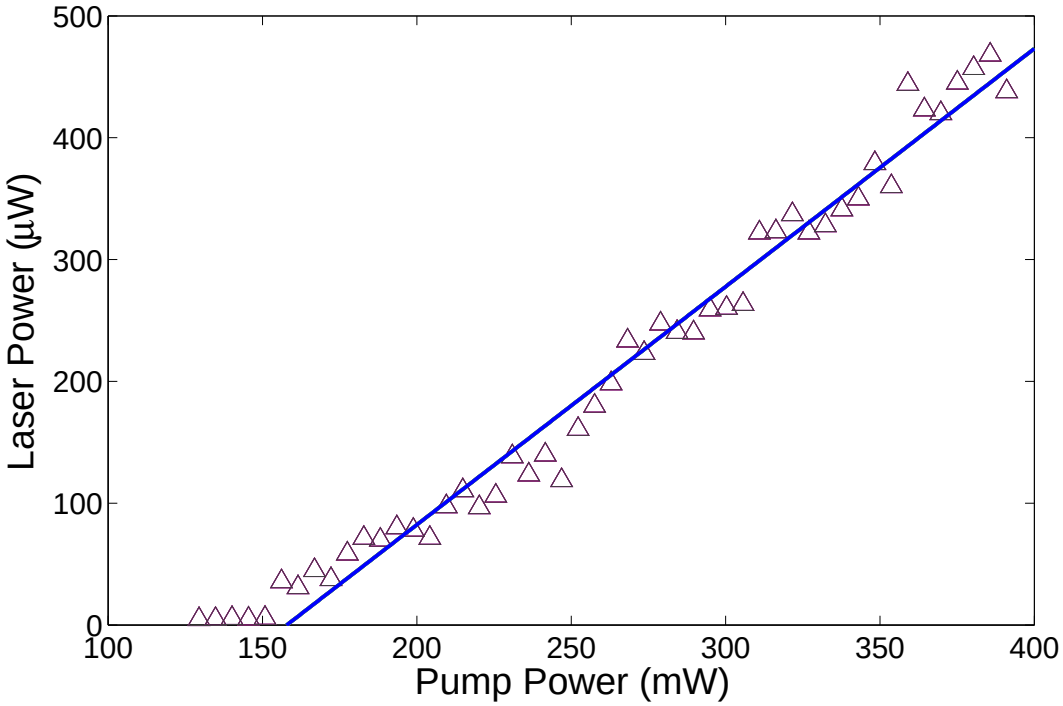

Figure 4.24: Output power versus input pump power for the ring laser.

The output from the ring laser is shown in Figure 4.24. The slope efficiency of the ring is 0.19 % with the lasing threshold of 150 mW of pump power. The low slope efficiency compared to the L-cavity and linear laser is due to low transmission by the mirrors combined with single pass gain.

4.8 Rotation Sensing Behaviour of the Nd^{3+}:phosphate Glass Ring Laser

Ring lasers have significantly more complicated behaviour than linear lasers. For the linear lasers there was only one beam produced. In ring lasers there are two beams which share the gain from the Nd^{3+}:phosphate gain medium. For an ideal rotation sensor the two beams are independent of each other, and the rotation experienced by the ring causes the shift in the frequency of the beams. In the previous chapter we have seen how backscattering one beam into the counter-propagating beam contributes towards a shift in frequency, which adds error to the rotation measurement in laser gyroscopes. This also applies to solid state ring lasers. Not only are SSRLs affected by this backscattering from cavity mirrors and the surface of the gain medium they also suffer from backscattering

from the gain grating formed by the standing wave in the gain medium. Figure 4.25 shows a schematic of the backscattering occurring through the gain grating. The layers of the grating are spaced half a wavelength apart. Each layer reflects a small proportion of the beam back into the other direction. This causes coupling between the beams in the ring gyroscope causing error in the measurements. Ideal gratings are formed by two waves (beams) travelling in the opposite direction but with the same frequency. The effect of these gratings on the population difference in shown in Figure 4.26. These gratings

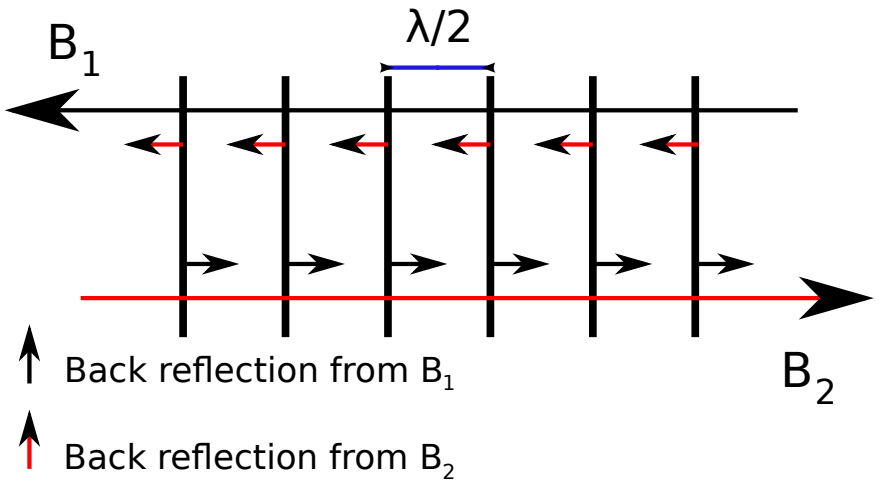

Figure 4.25: Schematic of gain gratings formed along the gain medium. The gratings are one half the wavelength apart. B_1 and B_2 are anti-clockwise and clockwise beams travelling around the cavity. Some of the clockwise beam is reflected by the grating into the path of the anti-clockwise beam, and vice versa. This causes coupling between the beams.

do not form in a gas ring lasers due to thermal motion of atoms which causes spatial averaging (smoothing). In a SSRL however, vibrations in the solid state material are small compared to the wavelength of the light, so spatial averaging does not occur (unless large vibration is deliberately introduced) [56]. When the frequency difference between the waves increases the spatial averaging increases. If the frequency difference is much larger than the inverse of the lasing life time of the material the gain grating decreases considerably or is eliminated [23].

The output from the ring is measured by using three silicon photo diodes shown as (D1), (D2) and (D3) in Figure 4.23. (D1) and (D2) measure the clockwise and counter clock wise monobeams, while (D3) measures the combined beams. Three different scenarios were observed in the ring through the detectors: when the ring has no AC modulation (lock-in), modulation at zero rotation rate and when the laser is measuring rotation of the turntable.

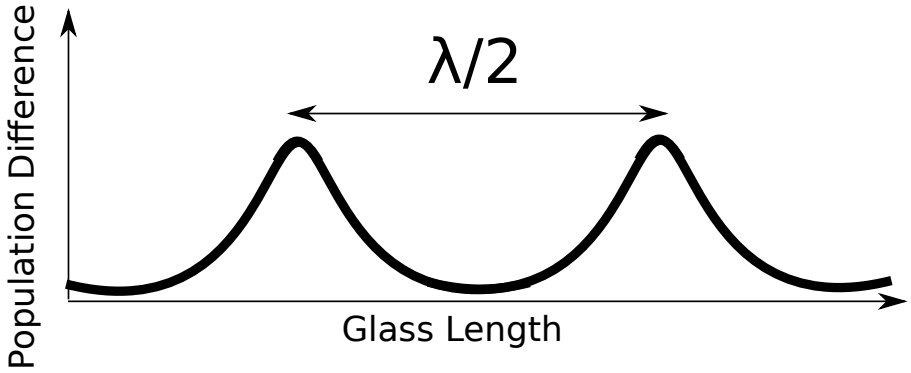

Figure 4.26: The gain grating formed inside the glass. The spacing between maximum population difference is half the wavelength. The frequency of the travelling wave in the clockwise and counter clockwise direction is the same.

4.8.1 Frequency Locked Operation

When the ring is not rotated, the measured output from the detectors (D1) and (D2) consists of a DC signal, that is similar to the output from the linear lasers. This is because the backscattering in the ring is high enough to cause strong coupling between the beams leading both beams to have the same frequency. The "lock-in" can be seen as a fixed fringe pattern in Figure 4.27 (left hand picture). This was observed by using a CCD camera (C in Figure 4.22) after a beam combiner. In order to produce such a fixed fringe pattern, both beams must have the same frequency.

The relative intensity of the two beams goes though a wide range of values. On some occasions, there were signs of coupling between the two beams, when one beam decreased in power while other increased at the same time. This is an indication that the available population is being shared between the beams.

4.8.2 Modulation at Zero Rotation Rate

Occasionally, the non-rotating ring produces a modulation pattern for a short period of time. Figure 4.28 shows an example of one of the modulation patterns observed. The monobeams (red and blue) are 180 degrees out of phase with each other. The combined beam is shown as a green trace from the photo-diode (D3).

Many similar modulation patterns can be observed with different fractional intensities and varying relative phase. The fractional intensity and the measured frequency of the beams are shown in Figure 4.29. It is also observed that when the modulation pattern appears, the fringe pattern measured by the CCD camera becomes blurred indicating the

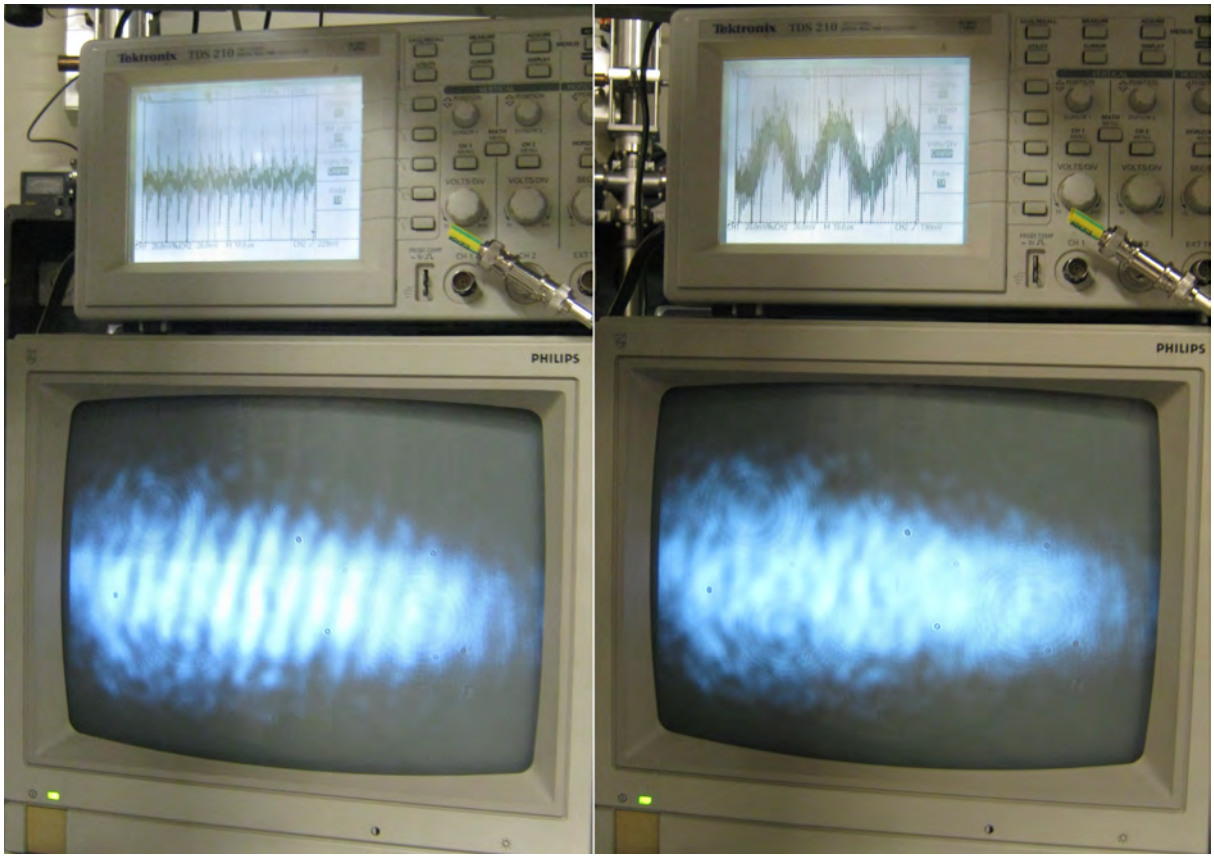

Figure 4.27: The picture on the left is the output from a locked gyroscope, while the right hand side is the unlocked gyroscope. The beat oscillation from the gyroscope is seen on the oscilloscope on the right.

two beams have different frequencies (see Figure 4.27). It is likely that the randomly observed modulation is a sign that the gain grating is unstable. As the grating weakens, possibly by noise of the pump or temperature changes, there are changes in the frequency of the observed modulation. The change in frequency (Δf) can be described by [57]:

$$\Delta f \approx \frac{c}{n\pi L}\sqrt{\gamma} \tag{4.13}$$

where n is average refractive index, L is length of the cavity and γ is the intensity-reflection coefficient of backscatter. Variation in γ causes the different modulation frequencies observed in Figure 4.29.

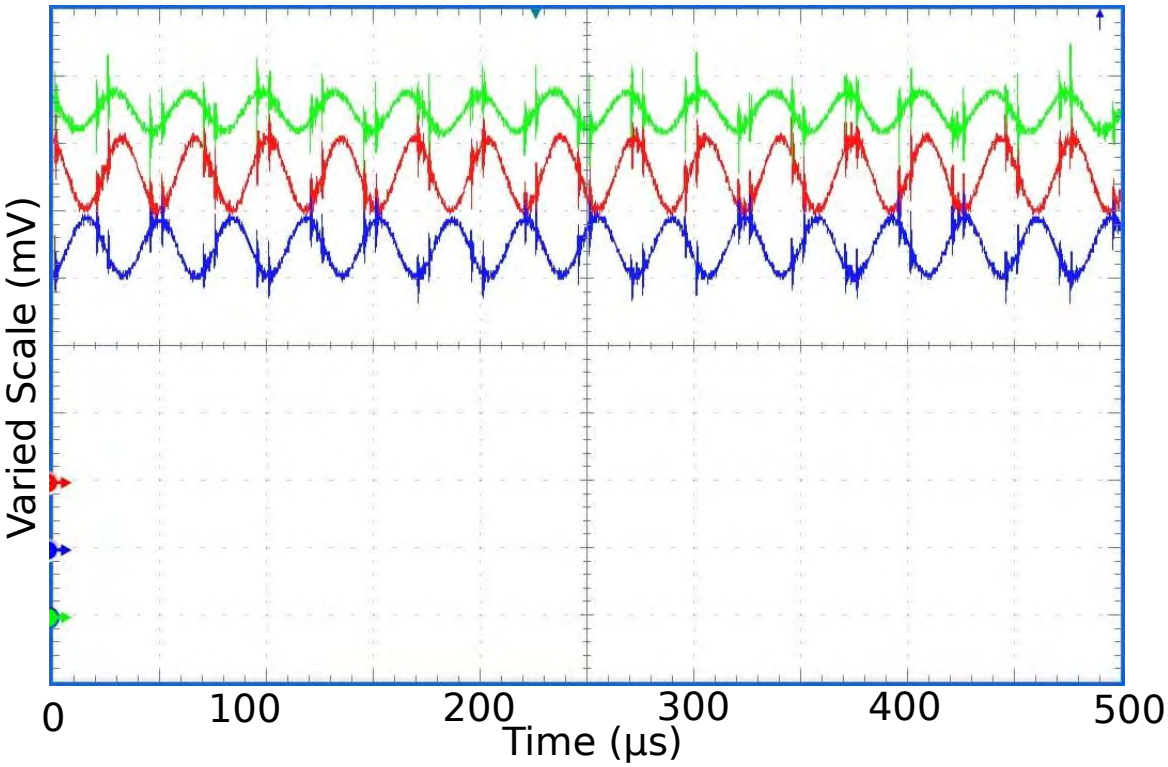

Figure 4.28: The red and blue traces are the mono beams, while the green trace is the combined beam. The reference point is different for each monobeam and the combined beam. The vertical scale is 40 mV per division for the monobeams. For the combined beam it is 90 mV per division. These scales were used so all the waveforms could be fit on the oscilloscope screen. In reality the combined beam signal is larger than the monobeam signal.

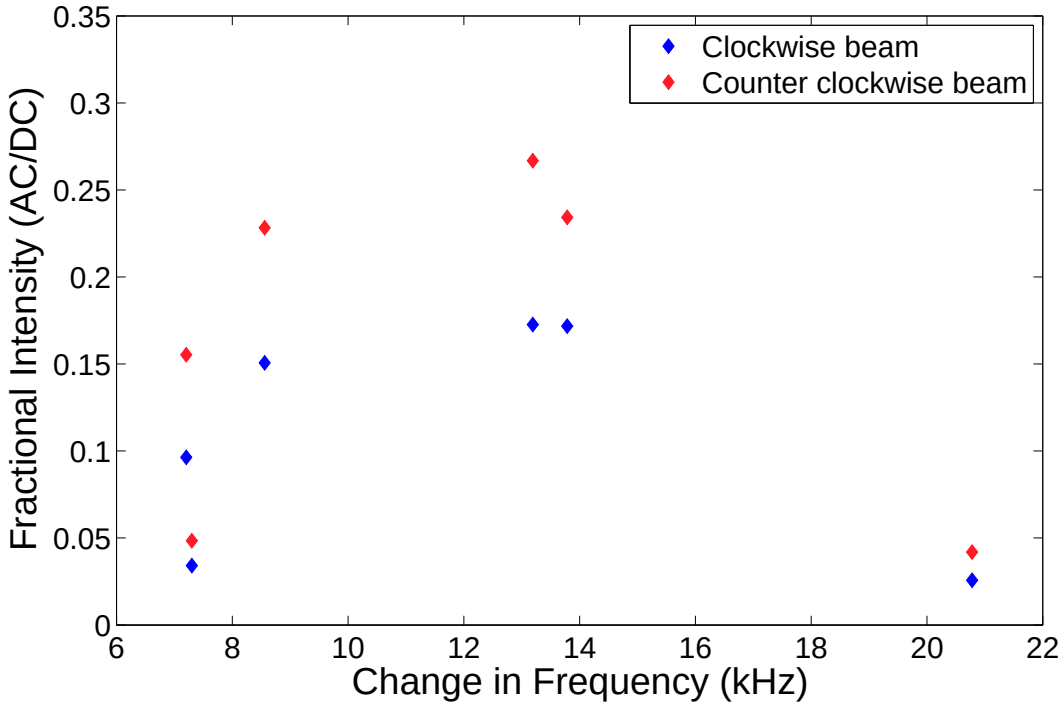

Figure 4.29: Fraction modulation intensity at various modulation frequencies observed when the ring is stationary.

4.8.3 Rotation Sensing Capability.

Under the influence of an external rotation provided by the turntable a clear Sagnac frequency (i.e modulation) could be observed. The Sagnac frequency was measured by a radio frequency (RF) spectrum analyser (Hewlett Packard ESA-L1500A). The output from the analyser for one of the rotation speeds is shown in figure 4.30. The Sagnac frequency measured in a similar way for various rotation rates is shown in Figure 4.31. The lowest frequency that the instrument can measure is 9 kHz, which limits the measurement at lower rotational speeds. Initially, the Nd gyroscope performance matched the theoretical line (shown as a solid red line), until an abrupt change in backscatter caused a break in the data. The abrupt change is possibly caused by a change in dimensions of the laser which affects the backscatter of the laser. As the rotation rate further increased, the effect of backscatter decreased, causing the measured Sagnac frequency to tend towards the theoretical line. This decrease in the effect of backscatter can also be seen on the fractional intensity of the beams, which decreases in amplitude as the rotation rate increases (see Figure 4.32). A similar effect can be observed in gas laser gyroscopes. The

theoretical solid red line was plotted using the Sagnac formula:

$$\upsilon(\Omega) = \frac{4\widehat{\Omega}.\widehat{A}}{\lambda P} \tag{4.14}$$

where $\upsilon(\Omega)$ is the Sagnac frequency, $P = 36$ cm is the perimeter of the cavity, $A = 80$ cm^2 is area enclosed by ring, lasing wavelength λ is 1054 nm and Ω is the rotational rate. The derivation of this formula is shown in the earlier introductory chapter.

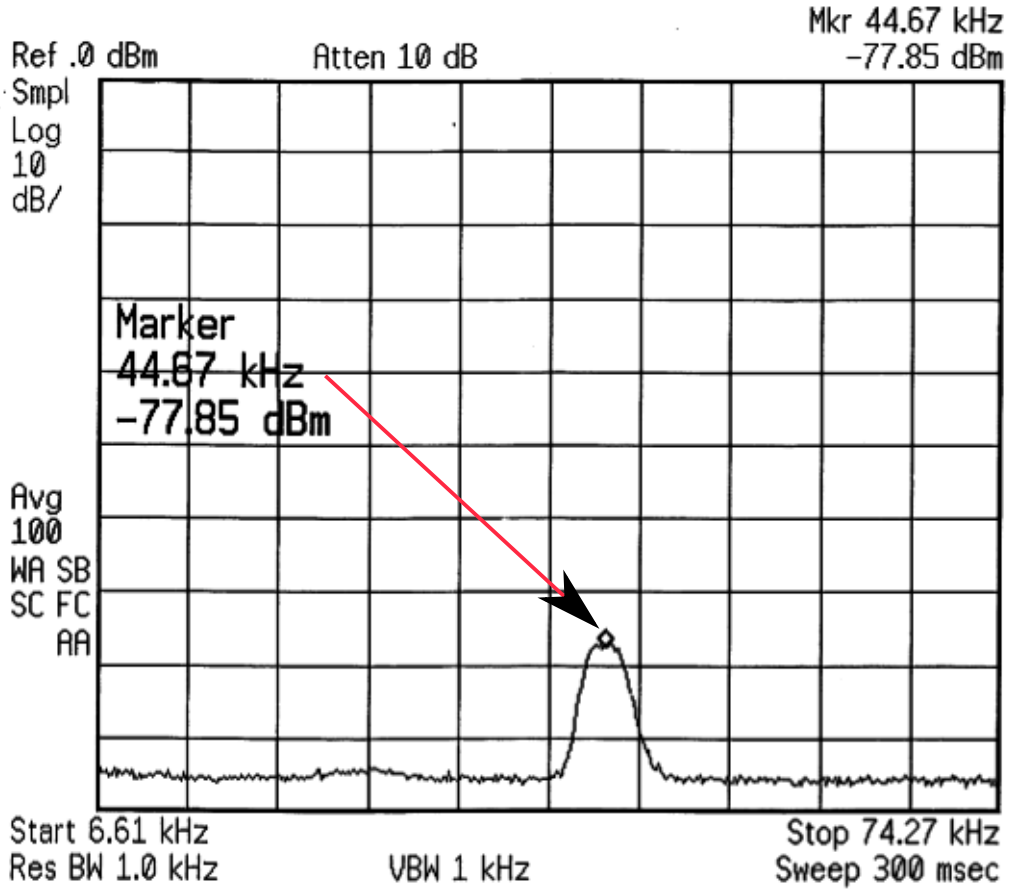

Figure 4.30: Output from a RF spectrum analyser. This measurement was taken at rotational speed of 0.46 rad/s and has been video averaged. The peak is marked by the marker point and value is displayed on the middle left of the figure.

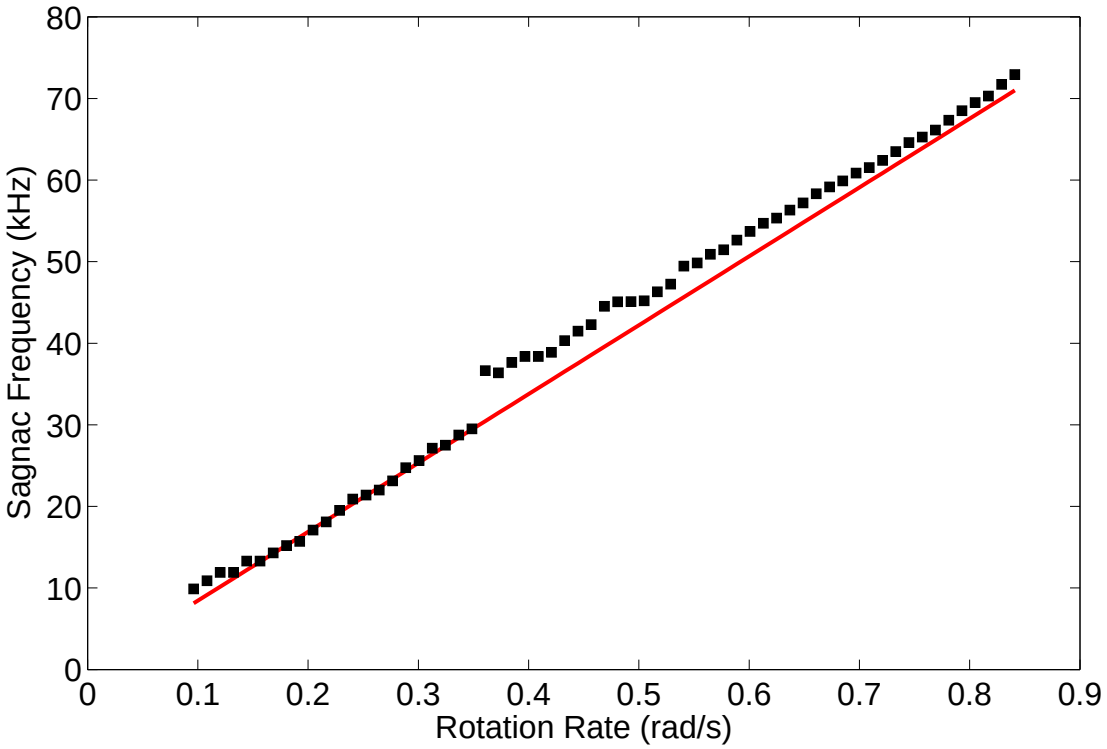

Figure 4.31: Sagnac frequency versus rotation rate for the Nd: phosphate ring laser. The solid line is the theoretical value.

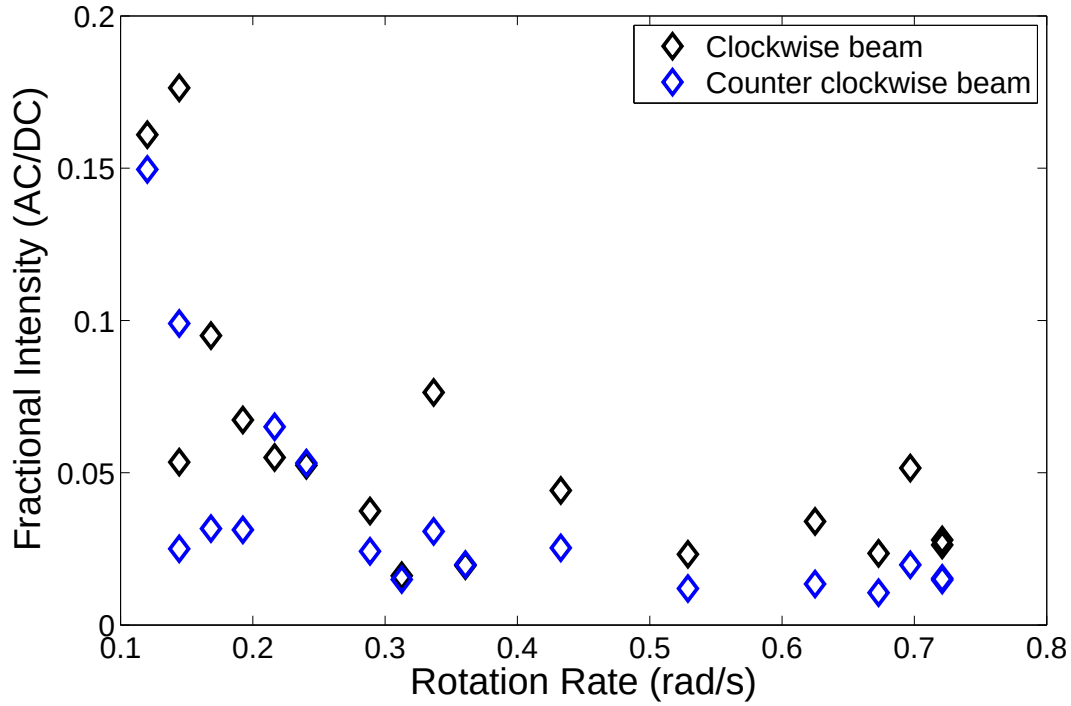

Figure 4.32: Variation of the monobeam fractional intensities for different rotation rates. Both beams show a general decrease in fractional intensity.

4.9 Observed Modulation Regimes

SSRLs have many types of modulation regimes. Several of them were observed throughout the course of characterisation of the gyroscope. Most of them are temporary and last only a fraction of a second. Due to the temporary nature of these regimes, only few are reported. One of the regimes observed is periodic directional switching of the laser beams. Figures 4.33 and 4.34 weringe observed when the ring is rotated at 2.5 rad/s. At this speed, backscattering is reduced considerably. As the backscattering lowers at a certain critical point sinusoidal modulations that are typically observed in both gas and SSRL are replaced by periodic directional switching [33]. A similar scheme was also observed in Nd^{3+}:YAG by Schwartz et al. [35] and Klochan et al. [32]. Schwartz et al. obtain this regime by modulating the pump power, while Klochan et al. increase the rotation speeds of the resonator. An extensive theoretical work by Zeghlache et al. [39] showed various pattern of modulation shown in figure 4.34 and 4.33.

Another phenomenon that occurs is chaotic modulation. In our experiment it occurred at a very high speed of 6.3 rad/s as shown in Figure 4.35. The regime was unpredictable

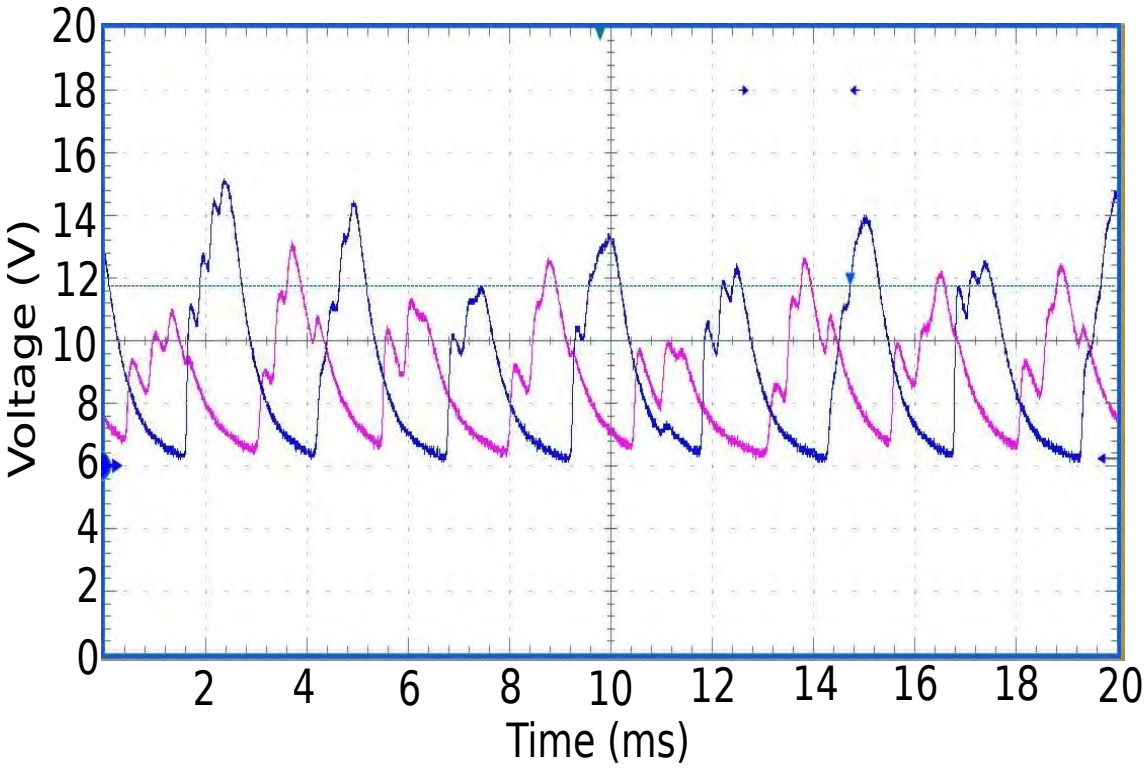

Figure 4.33: Periodic switching of the monobeams. The switching is out of phase with each other. It occurred at 2.5 rad/s

and only lasted for a fraction of a second. Similar chaotic behaviour has previously been reported, in a bi-directional ammonia ring laser [58] and in Nd^{3+}:YAG [35]. Chaotic behaviour was achieved in these rings by modulating the pump. It could be that the high rotational speed and vibration of the table modulated the pump alignment causing modulation in pump power. Both of the modulation regime are avoided by rotating table at lower rotational speeds.

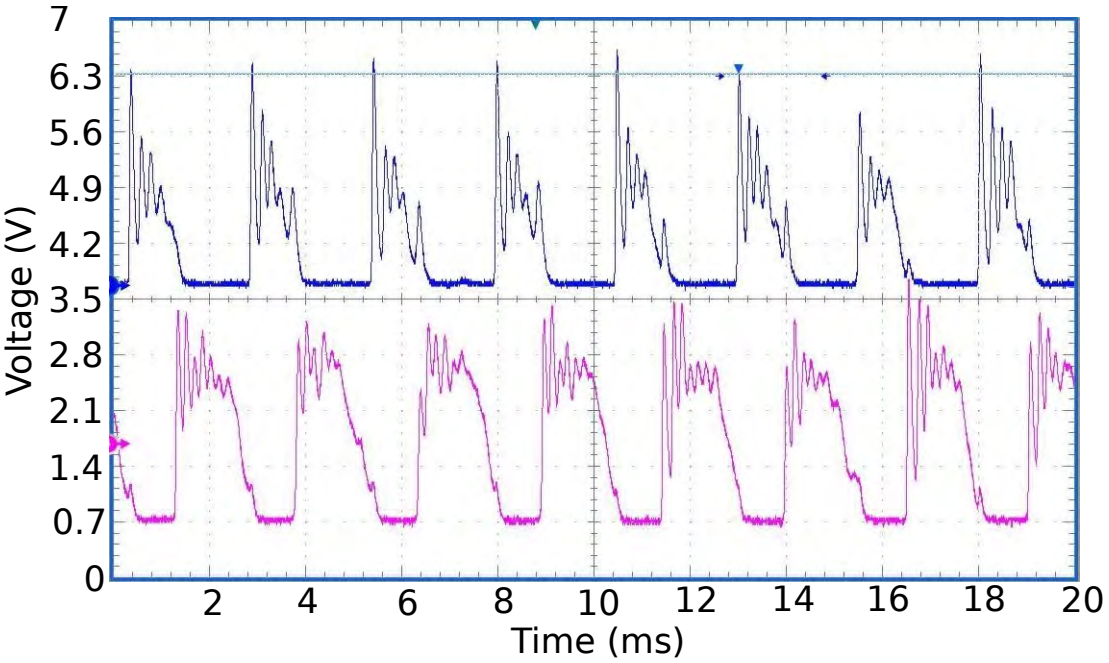

Figure 4.34: Periodic switching of the monobeams. The switching is out of phase with each other. It occurred at 2.5 rad/s

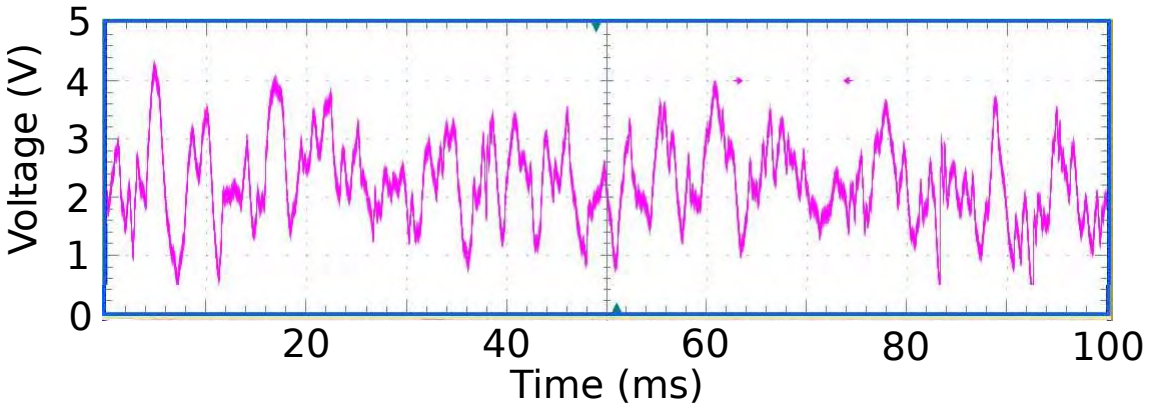

Figure 4.35: Chaotic modulation seen in the Nd^{3+}:phosphate ring at 6.3 rad/s.

4.10 Conclusion

In this chapter, the development of a laser diode pumped neodymium doped phosphate glass ring laser gyroscope has been presented. As the trivalent neodymium ion gives a four level laser system and due to the high solubility of rare-earth ions in phosphate glass, considerable gain is available. At a dopant concentration of 4 $\times 10^{20}$ ions/cm^3 a 20 % optically generated inversion yields 35 % gain. Initially, a 3 cm plano-concave linear cavity was used to test the 1 mm thick anti-reflection coated gain medium with longitudinal laser diode pumping. Using a 1 % output coupler, a slope efficiency of 24 % was achieved with a lasing threshold of 180 mW. It was notable that the laser did not have well defined polarisation states and this limited the operational stability. This was overcome by using s-polarised cavity mirrors in the ring laser design. The constructed ring laser had a perimeter of 36 cm and was placed on a homemade turntable and subjected to external rotation to test its usefulness as a gyroscope. Good behaviour was observed for rotation rates between 0.1 and 0.8 rads^{-1}. Lower rotation speeds can be measured using a different spectrum analyser with greater range than the one used in this experiment. Also using better cavity mirrors will also enable measurement at lower rotation rates. This is (to our knowledge) the first operation anywhere of a neodymium phosphate glass ring laser gyroscope in continuous wave mode. A gain grating formed in the material which caused several modulation regimes to be present in the gyroscope. When the ring was not rotated, frequency locking of the counter-propagating beams could be observed with occasional modulations apparent for short periods due to instability. Under the influence of an external rotation both periodic directional switching and chaotic modulation were apparent.

Chapter 5

Solid State Laser Gyroscopes. Part 2: An Erbium- Ytterbium Co-doped Phosphate Glass Laser

5.1 Introduction

In this chapter, the design and construction of a novel erbium-ytterbium (Er^{3+}-Yb^{3+}) co-doped phosphate glass laser gyroscope will be presented and discussed. It is a continuation of our goal to explore various gain media for laser gyroscopes. A particular interest has been given to erbium due to its very long life time of the upper laser level (24 times the lifetime of Nd^{3+}:phosphate). This leads to a longer time required to form the gain grating that creates unwanted coupling in SSRLs. Furthermore, the lasing wavelength of 1.5 μm emitted by erbium is extensively used in the telecommunications industry [59]. This means that the components needed for the laser gyroscope can be more readily and cheaply available.

Erbium is known to lase at cryogenic temperatures in CaF_2 (77 Kelvin) [60], and can be made to lase at room temperature when co-doped with ytterbium in $KY(WO_4)_2$ [61], $KLu(WO_4)_2$ [62], $SrY_4(SiO_4)_3O$ [63] ,Y_2SiO_5 [64] and Y_2SiO_2 [63]. Most of these lasers require expensive multiple pump diode set-ups and have large lasing thresholds that are not practically feasible in our facility. However, the lasing threshold can be lowered considerably using phosphate glass as a host. This is due to the high solubility of the dopants in this glass enabling high concentrations of erbium and ytterbium to be added. Highly efficient energy transfer between the erbium and ytterbium also occurs in phos-

phate glass, due to the close spatial proximity experienced in high dopant concentrations [65]. Additionally, the phonon energy in many crystals is lower than oxide based glass. For example, CaF_2 has a phonon energy around 328 cm^{-1} [66], while phosphate glass has an energy of 1100 cm^{-1} [67]. The larger phonon energy causes a higher probability for multi-phonon decay to the lasing level [68], an increase in efficiency by decreased parasitic emission and improved energy transfer between the erbium and ytterbium ions leads to a lower lasing threshold. The main difference between the Er^{3+}-Yb^{3+} laser and the Nd^{3+} laser built in the previous chapter is how the population inversion is maintained. For the Er^{3+}-Yb^{3+} laser to function, more than half of the available electron population needs to be excited to the upper lasing level. In a four level laser population inversion must simply be maintained between lasing levels which does not include the ground state. Therefore four level laser systems are the most commonly used.

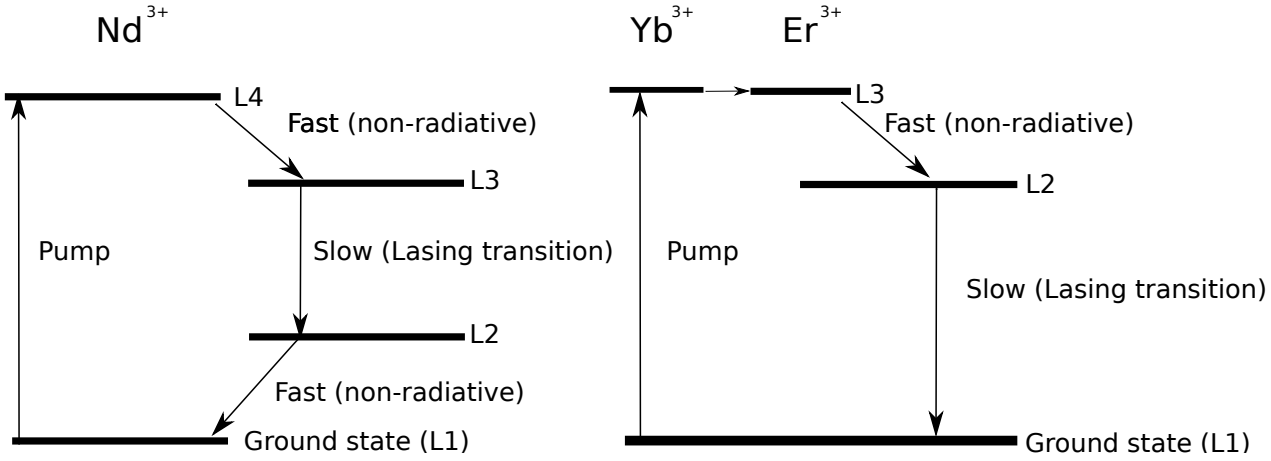

Figure 5.1: Energy level diagram for four and three level laser systems. Population inversion between (L2) and (L3) are required for Nd^{3+} and between the ground state (L1) and (L2) for Er^{3+}-Yb^{3+} .

Figure 5.1 shows the three and four level lasing systems. A three level system has the ground state (L1) as a part of the lasing transition, requiring at least half of the population from the ground state to be pumped to achieve inversion. In a four level system, the lower lasing transition is emptied by fast (non-radiative) processes, making it easier to achieve the required inversion. Furthermore, the high pump power required to achieve inversion in a 3-level system increases the chances of thermal damage. Additionally, the Er^{3+}-Yb^{3+} modal volume in the cavity needs to be completely pumped otherwise absorption at the lasing wavelength by the ground state adds to the losses. The neodymium system does not have this requirement, since the lasing level is not populated at room temperature. Due to these lower system requirements the Nd:phosphate gyroscope was built first.

5.2 The Gain Medium

Erbium by itself does not have the required efficiency to work as a laser at 1.5 μm at room temperature [46]. It is the addition of ytterbium ions having a large absorption cross section at the pump wavelength that improves the efficiency enough to be able to achieve lasing at room temperature. As shown in Figure 5.2 the upper energy level of trivalent ytterbium ${}^2F_{\frac{5}{2}}$ is closely matched with the ${}^4I_{\frac{11}{2}}$ multiplet of Er^{3+} . This facilitates resonant energy transfer between the ytterbium and erbium ions. This process also occurs between ytterbium ions, especially when the doping concentration is high [69]. The energy transfer process terminates when it reaches an erbium ion.

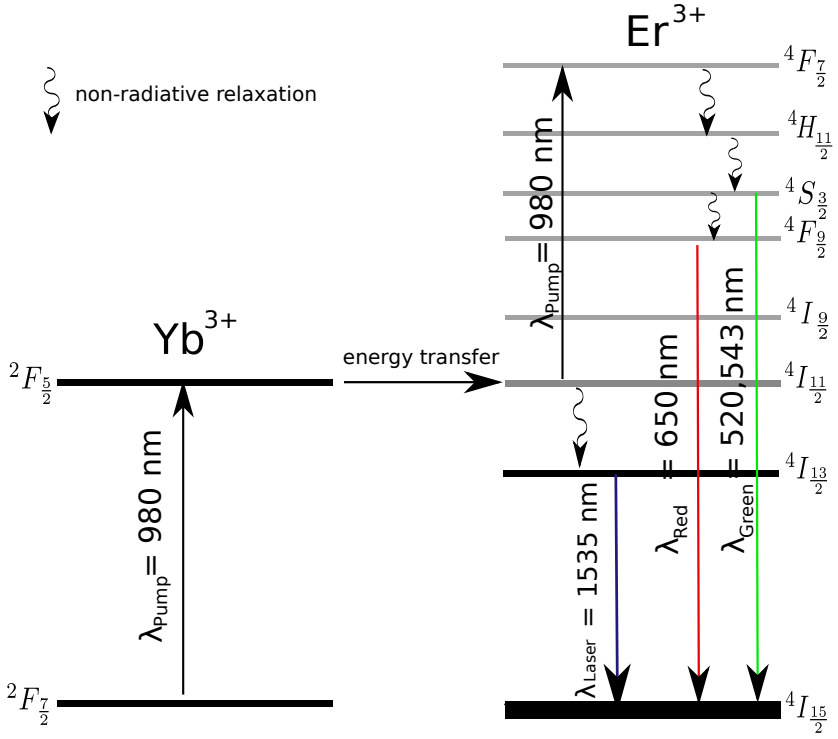

Figure 5.2: Schematic energy level diagram for the erbium ytterbium system.

Once the ${}^4I_{\frac{11}{2}}$ multiplet is populated two main processes can occur: (1) the erbium can be further excited by the pump to ${}^4F_{\frac{7}{2}}$ causing parasitic green and red emission or (2) A more favourable process is multi phonon decay to the upper lasing level. These two processes are dependent on the lifetime of ${}^4I_{\frac{11}{2}}$. For example, the non-radiative lifetime for a phosphate glass is less than 1 μs while it is 13 μs for the ytterium orthosilicate crystal [63]. This causes the likelihood of parasitic emission to be higher in ytterium orthosilicate. The main requirement for the material to work as a laser is that there must be population inversion between the ${}^4I_{\frac{13}{2}}$ and ${}^4I_{\frac{15}{2}}$ multiplets.

5.2.1 Erbium and Ytterbium Dopant Concentrations

The concentration of erbium and ytterbium will determine the performance of the laser. In the literature, the concentration of erbium varies from 1.4×10^{19} cm^{-3} to 1.5×10^{20} cm^{-3} and that of ytterbium varies from 2×10^{20} cm^{-3} to 2×10^{21} cm^{-3} [61, 62, 64, 70–75] for various hosts.

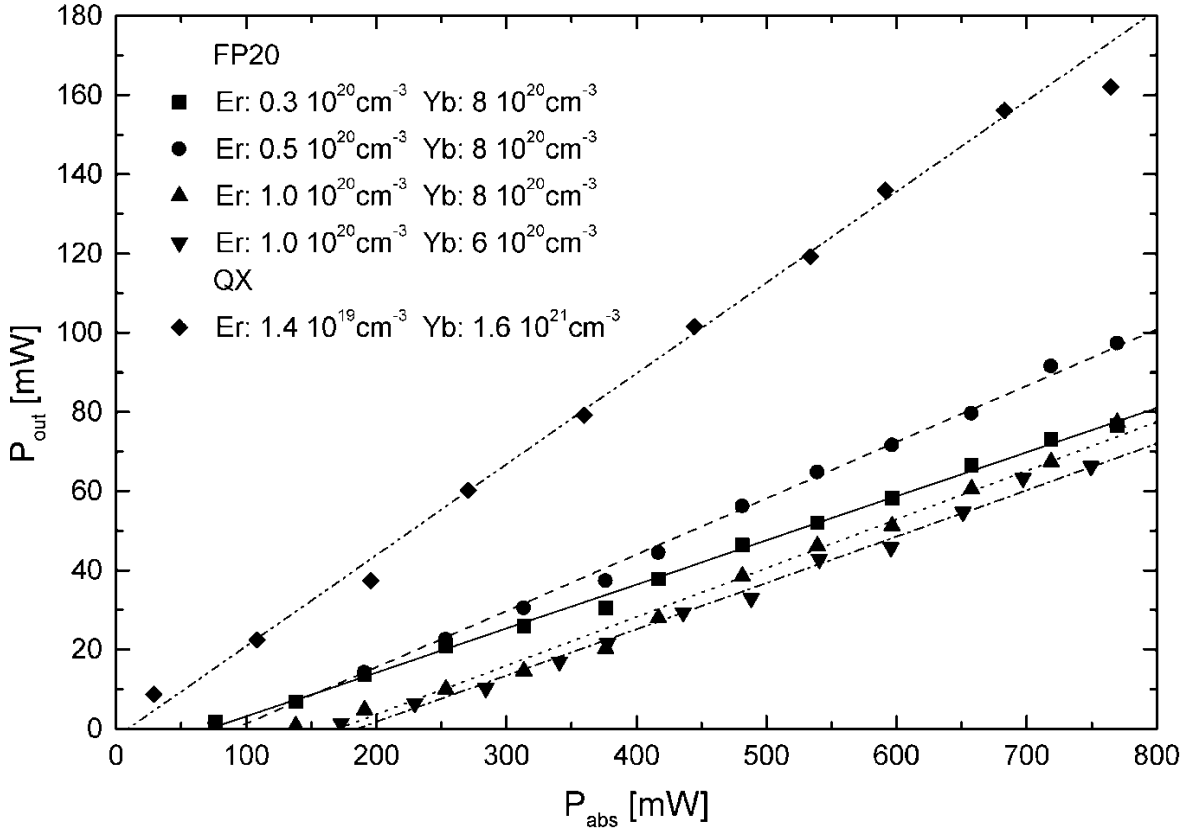

Figure 5.3: Lasing properties for different dopant concentrations of Er^{3+} and Yb^{3+} in fluoride phosphate and a phosphate glass (Kigre). P_{abs} is the absorbed pump power. P_{out} is the laser output power. All samples were 1.8 mm thick [6].

The relationship between ytterbium and erbium is demonstrated by Figure 5.3. The lasing threshold decreases as the ytterbium concentration increases, while an increase in erbium concentration improves the slope efficiency at the expense of the lasing threshold. An increase in the ytterbium concentration provides more ions to absorb the pump. However, it can only increase to a certain extent since erbium ions are needed to transfer the energy. While adding erbium improves the slope efficiency, it also increases the absorption loss. This also illustrates the need to pump the whole mode volume of the laser as unexcited erbium ions will absorb at the lasing wavelength. From Table 5.2, the lowest threshold of 58 mW was achieved from material made by Kigre with erbium and

ytterbium concentrations of 1×10^{20} ions/cm^3 and 2×10^{21} ions/cm^3 respectively for a gain medium 1 mm thick.

An attempt at building a laser was made using the same concentration as the Kigre material but with a 5 mm gain medium to increase the overall gain. This sample was made by MolTech and failed to lase. When the pump power was increased the gain medium fractured.

The failure of this material was attributed to a reduction in the transmission of the pump beam through the gain medium (the mode volume is not completely pumped in the cavity). To calculate the transmission through the sample, the Beer Lambert law was used:

$$\sigma_a(\nu) = \frac{-\ln \frac{I_o}{I}}{Nl} \tag{5.1}$$

where I_o is the incident power, I is the power transmitted through the sample, N is number of ytterbium ions per cm^3 and l is thickness of the sample. The absorption cross section of the erbium and ytterbium used was 10.5×10^{-21} cm^2 [68] and 8.4×10^{-21} cm^2. Calculation showed that the transmission through the failed 5 mm glass sample was practically 0 % (2.8×10^{-3} %). This shows that the erbium ions at the end of the sample are not pumped. This cannot be done by increasing the power, as it will cause the glass to fracture. This led to the choice of a decrease in the sample length. Another approach that could have been taken is to pump the sample from both side.

Two gain media were ordered from MolTech, having an ytterbium concentration of 1.4×10^{21} ions/cm^3 and an erbium concentration of 0.5×10^{21} ions/cm^3. The concentration of ytterbium and the thickness were lowered to increase the transmission, while the erbium concentration was increased by 5 fold to compensate for the loss of gain caused by the decrease in length of the sample. Two samples were ordered with 1 mm and 1.5 mm length. The transmission through the sample were 66 % and 54 %. Lasing was achieved with both media.

Table 5.1: Erbium-ytterbium co-doped lasers as published (1992:2008).

Reference	Slope efficiency	Threshold	Wavelength (nm)	Pump method	Type of host and length	ROC	Cavity Length (cm)	Reflectivity of output coupler
[70]	8.2-10.2%	88.6-165.7 mW	1545	InGaAs 970 nm	Phosphate, 1 cm	5 m	N/A	80-99%
[61]	1.00%	470 mW	1500	Ti-Al_20_3 930 nm	$KY(WO_4)_2$, 0.25 cm	10 cm	N/A	99%
	N/A	1W	1500	InGaAs 965 nm	$KY(WO_4)_2$, 0.25 cm	5 cm	N/A	99%
[64]	0.40%	274 mW	1554	InGaAs 966-980 nm	$SrY_4(SiO_4)_3O$, 0.25 cm (c-cut)	0.75 cm	N/A	99%
	12.00%	36 mW		InGaAs 966-980 nm	Phosphate, (N/A)	0.75 cm	N/A	99%
[71]	Pulsed 4%	Average-20W	1540	Phosphate, N/A	8 cm	N/A	N/A	
[5]	1.1-1.2%	2.6W, 3.3W, 4.45W	1591-1614	fibre coupled laser 24W 980nm	$KLu(WO_4)_2$, 0.32 cm	5 cm	0.9 cm	99.3%, 98% ,97%

Table 5.2: Erbium-ytterbium co-doped lasers as published (1992:2008) continued

[62]	0.9-1.1%	0.7W, 1.3W,1.6W, 2.4W	1534-1594	High power fibre coupled laser	$KY(WO_4)_2$, 0.32 cm	5 cm	0.9 cm	99.7%, 99.3%, 98%, 97%
	1.3-1.6%	1W, 1.1W, 1.5W, 1.9W	1554-1596	High power fibre coupled laser	$KY(WO_4)_2$, 0.32 cm	5 cm	0.9 cm	99.7%, 99.3%, 98%, 97%
[73]	30%	58 mW, 48 mW, 32 mW	1533 - 1563	InGaAs	Phosphate, 0.1 cm	1 cm	0.5 cm	99.5%, 99%, 98%
[74]	21%, 19%, 19%	Above 73 mW	1535-1567	InGaAs	Phosphate, 0.1 cm	1 cm	N/A	98%, 99%, 99.5%
[75]	12%	100 mW	1530	InGaAs	Phosphate, 0.2 cm	flat	N/A	99%

5.2.2 Spectroscopy of the Gain Medium

Spectroscopy of the gain medium was performed to calculate the available gain of the material. For neodymium only the emission cross section is needed to calculate the gain. The erbium-ytterbium system requires both the emission and absorption cross sections. Absorption measurements were conducted using a single beam Infrared Fourier Transform Spectrometer (Digilab FTS-40). Figure 5.4 shows the transmission through the sample

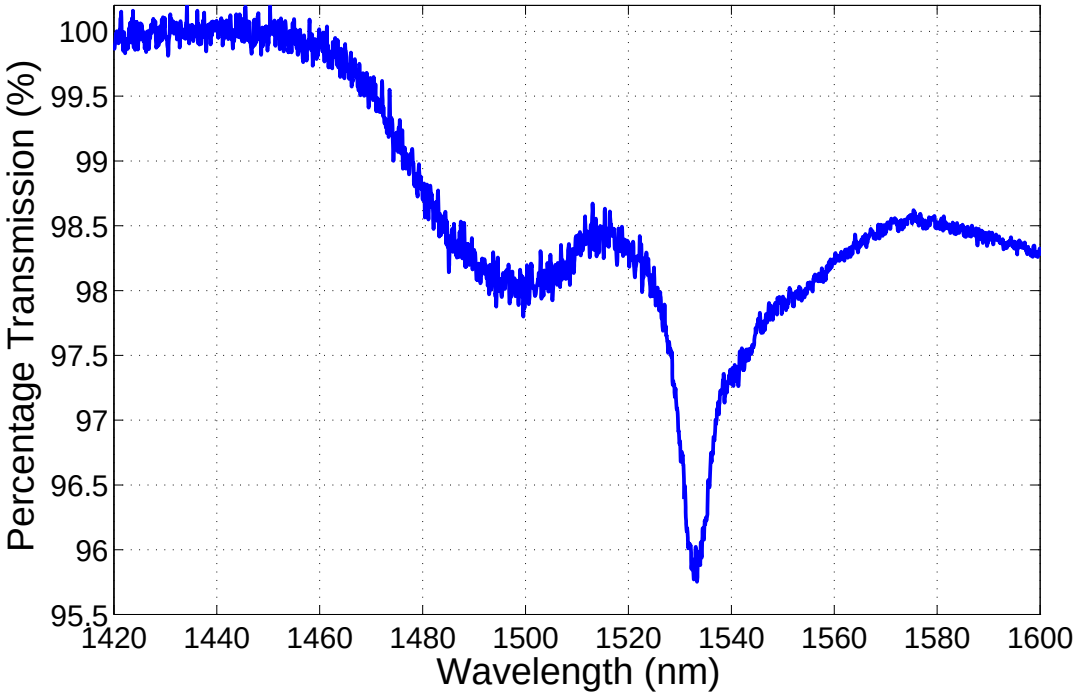

Figure 5.4: Percentage transmission through a 1 mm Er^{3+}-Yb^{3+} phosphate glass sample.

measured by the spectrometer. This was converted to absorption cross section (σ_a) using equation 5.1, where $\frac{I_o}{I}$ is the frequency dependent transmission. N is the number of erbium ions per cm^3 and is equal to 5×10^{19} ions/cm^3. l is the thickness of the medium and is equal to 1 mm. From the absorption cross section (σ_a), it is possible to determine the emission (σ_e) cross section using McCumber's theory [76, 77].

$$\sigma_e(\nu) = \sigma_a(\nu)\frac{Z_l}{Z_u}e^{[\frac{\epsilon - h\nu}{kT}]} \tag{5.2}$$

where ϵ is the difference in energy between the lowest crystal field spilt ${}^4I_{\frac{13}{2}}$ and ${}^4I_{\frac{15}{2}}$ energy levels and it is equal to 6493 cm^{-1}. Z_u and Z_l are partition functions for the upper and lower levels. The fraction $\frac{Z_u}{Z_l}$ is approximated to be unity [78]. The absorption and emission cross section calculated are shown in Figure 5.5. Even though the emission cross

section value is twice that of neodymium, for low inversion levels a high proportion of photons are absorbed since the absorption and emission cross section values are almost the same. For example, the emission and absorption cross sections at the peak value are 8.6×10^{21} cm^2 and 8.4×10^{21} cm^2 (at 1534 nm).

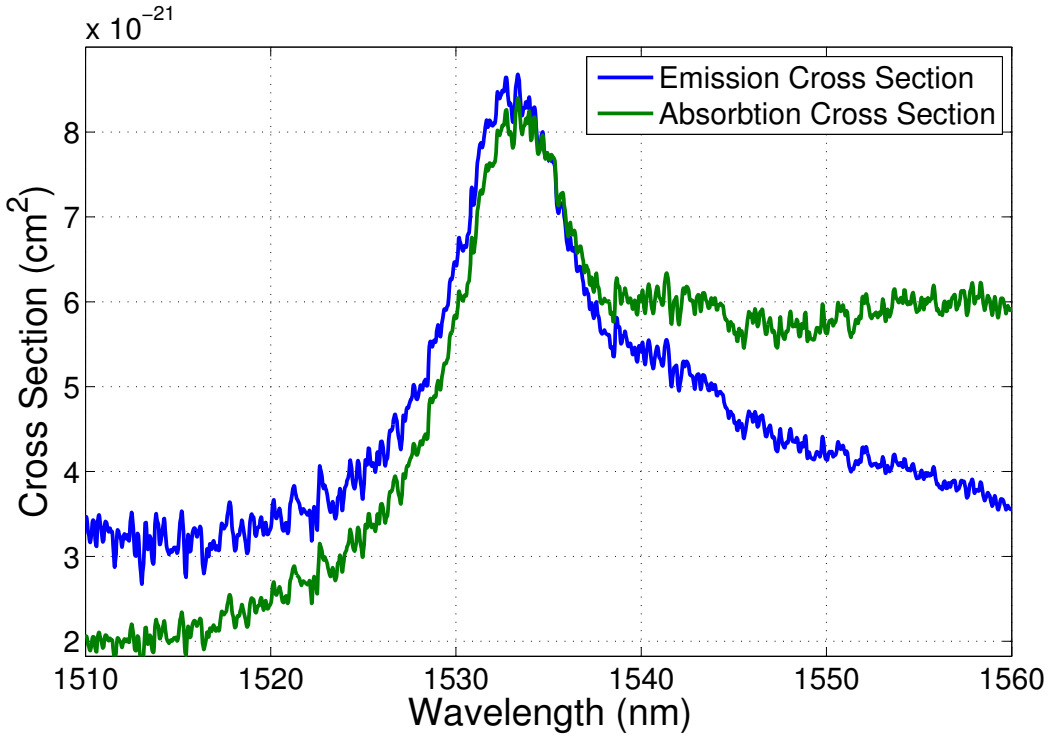

Figure 5.5: Absorption and emission cross sections of a 1 mm thick Er^{3+}-Yb^{3+} phosphate glass sample.

Using the absorption and emission cross sections the single pass gain is calculated using:

$$G = e^{(\sigma_e N_2 - \sigma_a N_1)z} \tag{5.3}$$

where N_1 and N_2 are the populations of the upper and lower lasing levels and z is the length of the crystal. Figures 5.6 and 5.7 show the gain G for various inversion levels. When the gain G is unity the absorption loss from the gain medium is equal to the amplification. For example a value 1.04 corresponds to four percent gain above the threshold. The larger the pump rate, the greater the inversion and gain. In Figures 5.6 and 5.7, the length of the gain media z are different. A longer gain medium produces higher overall gain for the same inversion level. The shape of the gain curve also changes with the inversion. At 60 % inversion the gain in the region around 1555 nm is greater than 1534 nm, but for higher inversion this is reversed.

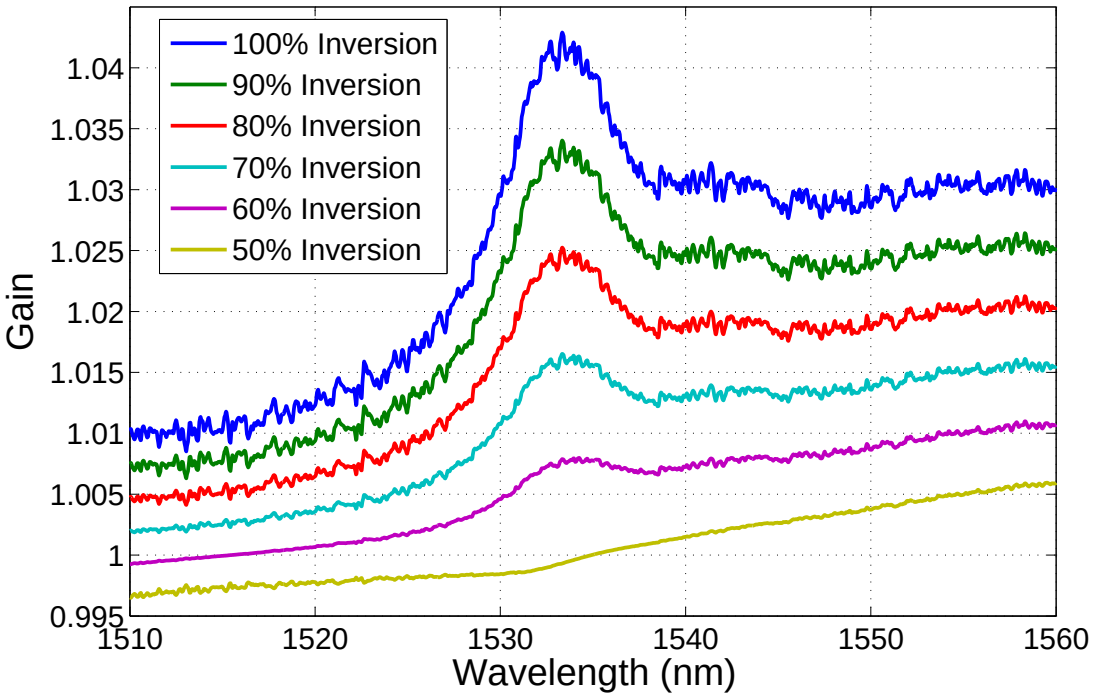

Figure 5.6: Gain profile for a 1 mm thick Er^{3+}-Yb^{3+} phosphate glass sample.

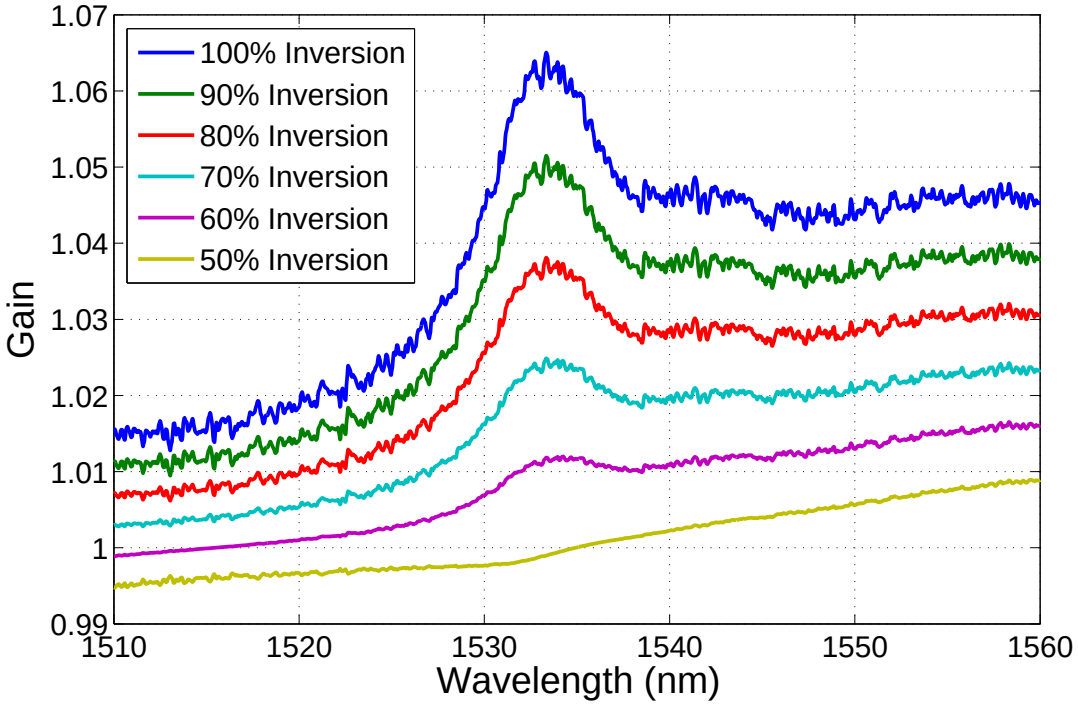

Figure 5.7: Gain profile for a 1.5 mm thick Er^{3+}-Yb^{3+} phosphate glass sample.

Figure 5.8 shows the percentage gain above threshold at 1534 nm at various inversion levels for the 1 mm and 1.5 mm gain media. At 50 % inversion, the percentage gain is zero and any value below this inversion level the net gain is negative due to absorption. Figure 5.8 also shows the 1.5 mm sample needs greater pumping than the 1 mm sample to counteract the greater absorption.

This is in contrast to the similar Figure 4.3 for the Nd^{3+}:phosphate sample, where there is no absorption at the lasing wavelength. In comparison the gain at 50 % inversion for Nd^{3+}:phosphate is 114 % while Er^{3+}-Yb^{3+} gain is zero. This significant difference in gain makes the tolerance of building the Er^{3+}-Yb^{3+} laser much tighter.

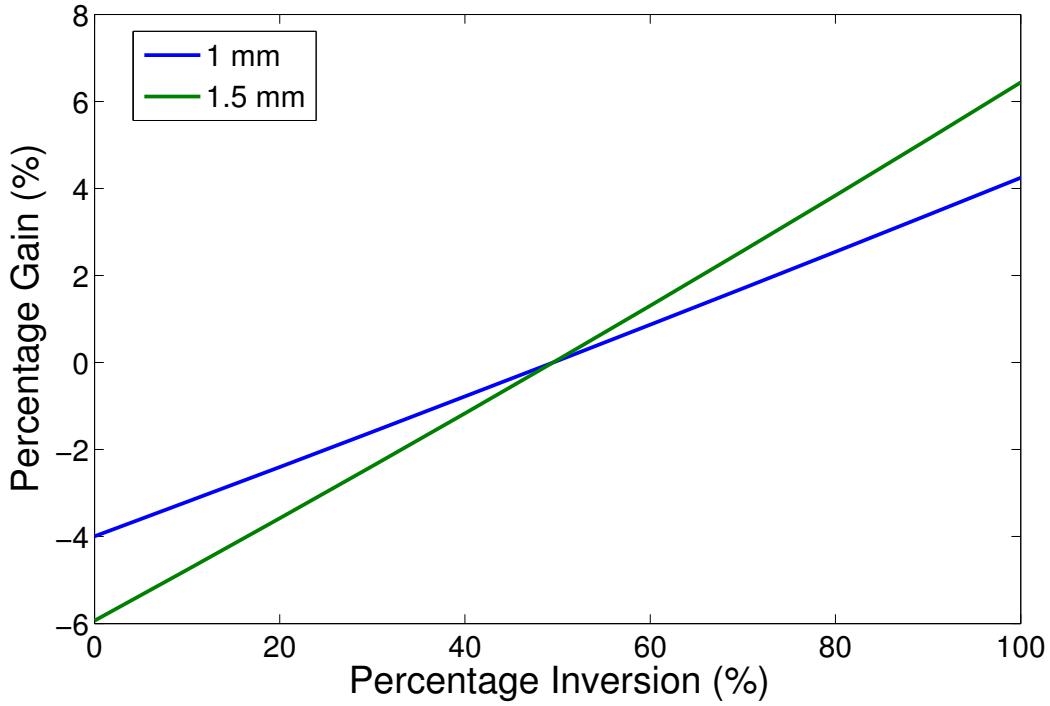

Figure 5.8: Gain available at 1534 nm for a 1 mm and 1.5 mm Er^{3+}-Yb^{3+} phosphate glass gain medium as a function of inversion level.

5.3 Linear Laser Cavity

A linear laser was built using the same cavity parameters as used for the neodymium phosphate linear laser. Consequently, it has the same stability conditions. Furthermore, the alignment process is the same, but using a red helium neon laser as an alignment beam, due to the higher reflectivity of red light by the cavity mirrors (see Figure 5.9 and

5.10).

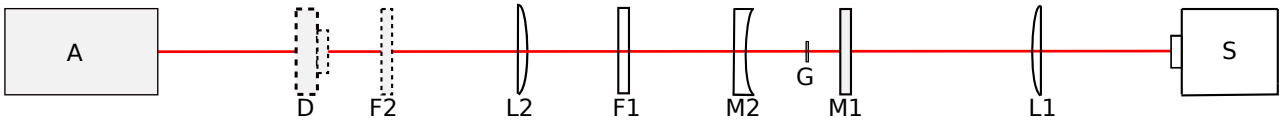

Figure 5.9: Schematic of the constructed Er^{3+}-Yb^{3+} linear laser. Where, A is a red He-Ne laser, D is the detector, L1, L2 are lenses, M1, M2 are the cavity mirrors, F1, F2 are filters, O is a fibre spectrometer, G is the gain medium and S is the diode laser.

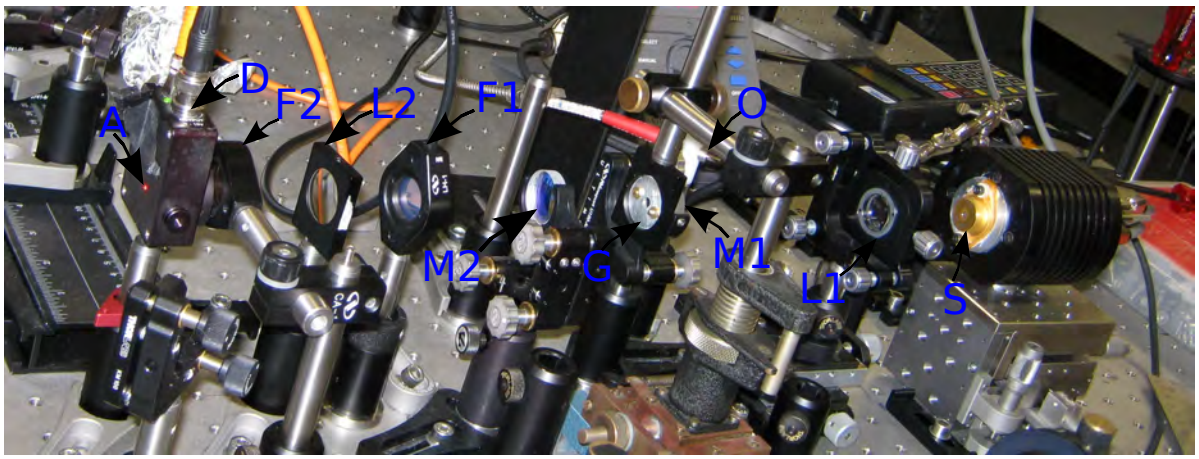

Figure 5.10: Photo of the constructed Er^{3+}-Yb^{3+} linear laser. Where, A is a red He-Ne laser, D is the detector, L1, L2 are lenses, M1, M2 are the cavity mirrors, F1, F2 are filters, O is a fibre spectrometer, G is the gain medium and S is the diode pump laser.

The linear cavity concave mirror (PR1-1550-98-1025-0.075CC) and planar mirror (SWP-0-R-1500-T-946-PW-1025-C) were purchased from CVI Melles-Griot. The planar mirror was dichroic to allow transmission of the pump beam. Since the gain available is small it was worth testing the reflectivity of the mirrors. The cavity mirrors were tested using a Fourier Transform Infra-red (FTIR) spectrometer and the result is shown in Figure 5.11. There is a flat region between 1400 nm and 1750 nm where the transmission is the smallest. The region is about 50 nm shorter for the planar mirror. Past this region the reflectivity decreases rapidly.

Looking back at Table 5.1 (fourth column), the biggest range of wavelengths emitted is between 1530 nm and 1614 nm, which is in the region of lowest transmission. This gives the measured range of transmission between 1.2 % to 1.5 % for the concave mirror (output-coupler) and 0.2 % to 0.3 % for the dichroic mirror. This essentially agrees with the manufacturer's quoted values.

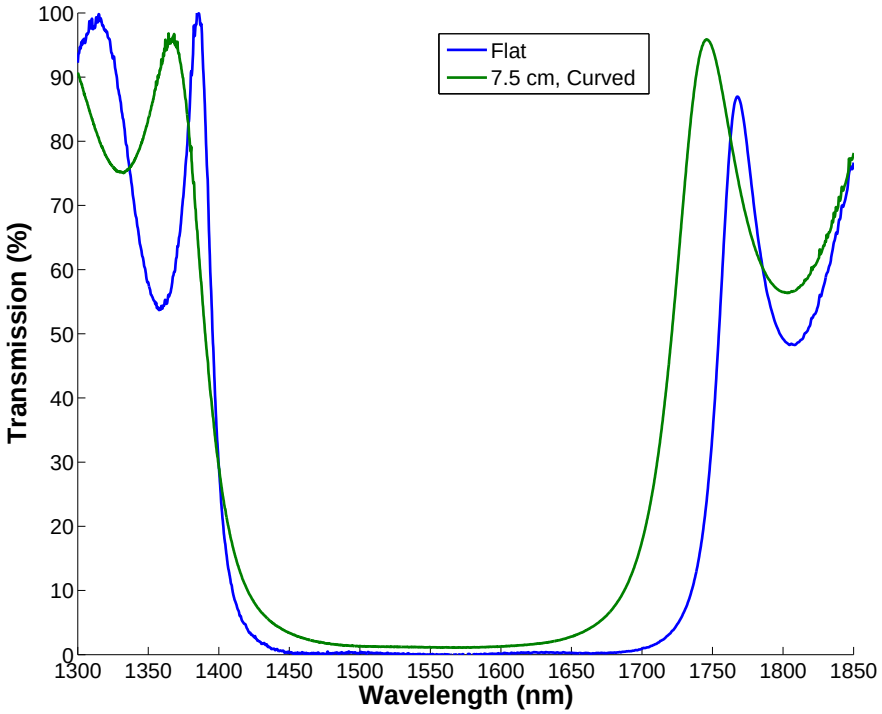

Figure 5.11: Transmission through the cavity mirrors. The planar mirror is dichroic and the concave mirror is a 2 % output coupler.

5.3.1 Laser Diode Pump

The optimum pump source is one that matches the absorption band of the gain medium, and that can be manipulated to create a population inversion along the entire mode volume. Fortunately, InGaAs diodes operate around 980 nm which matches closely with the absorption wavelength of ytterbium. The pump laser was supplied by Intense^{TM} (3120-T03-TEC-FAC-98005) corporation and had a maximum output of 2 W. The centre wavelength was 979.6 nm with a FWHM of 0.7 nm at 25 ^{o}C. Figure 5.12 shows the wavelength profile. The diode also has a TEC (thermoelectric cooler) to maintain a constant temperature.

The beam quality is equally important as power. For maximum efficiency the beam waist of the diode should match the beam waist of the cavity [79]. Longitudinal pumping is particularly suited to achieve this criteria [80]. The Intense^{TM} diode has a full width half maximum divergence of 48×10 deg [81] . The diode was purchased with fast axis collimation (FAC) so the beam divergence on the fast axis is comparable to the slow axis. To check the performance of the FAC, the beam profile was measured by blocking

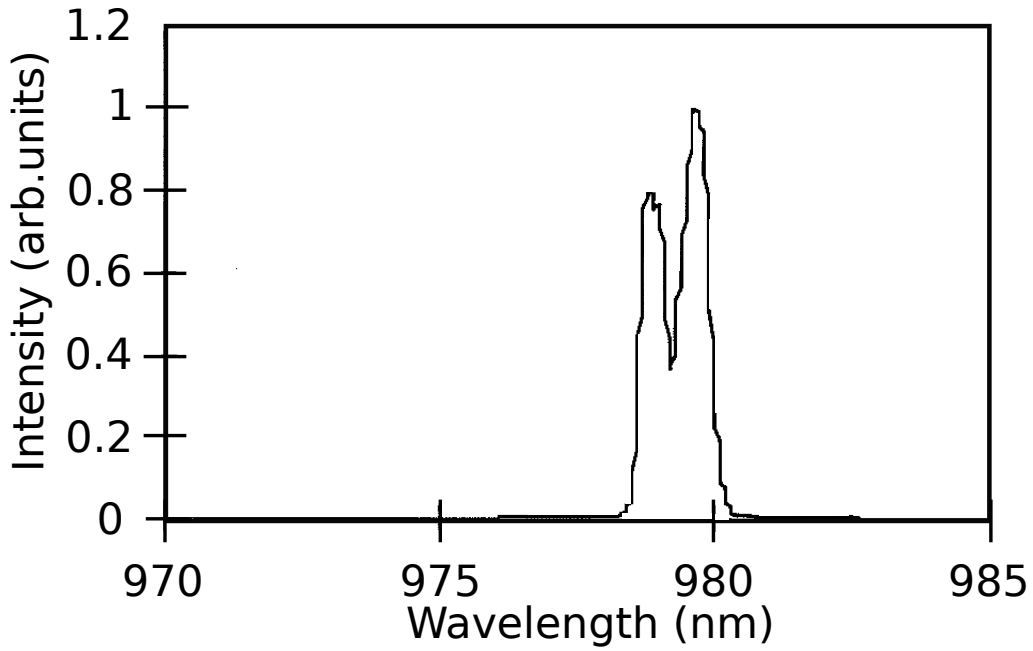

Figure 5.12: Spectrum of the Intense laser diode at 25^o C. The information was supplied by the manufacturer.

the beam with a knife edge in the horizontal and vertical directions. Two cross sections are needed to measure the divergence angle of the beam. One of the cross sections was taken on the face of the diode, the other is 13.5 mm away from the diode. The first cross section is denoted A and the other denoted B. One of the assumptions was that the emitting aperture was a point source. Throughout the experiment, the diode power was maintained at a constant power. The change in flux was divided by the change in distance and plotted in Figure 5.13 for cross section A and Figure 5.14 for cross section B. The laser diode maybe running on multiple transverse mode causing noise seen in figure 5.13 and reffig:crossB. Both figures also have horizontal lines intersecting where the diameter of the beams were taken. This was added to the uncertainty of the measurement seen in Figure 5.15 and 5.16. The uncertainty is large for the cross section away from the diode face due to divergence of the beam. The angle β is calculated to be $2.5^o \pm 0.6^o$ and θ is 2.9^o $\pm$ 0.6^o. Thus, the divergence of the beam on both axes is the same within the uncertainty of the measurement, hence standard optics will be sufficient for the experiment[1]

[1]Normally cylindrical lens or amamorphic prisms are used to compensate for varying divergence on different axes.

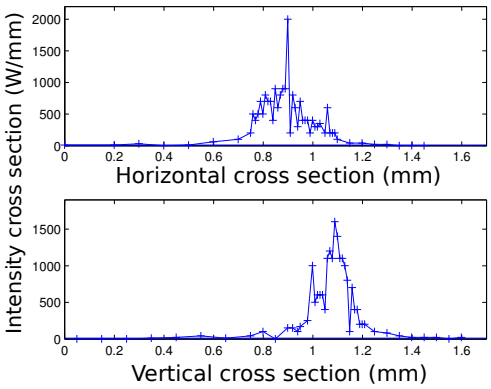

Figure 5.13: The beam cross section of the diode face.

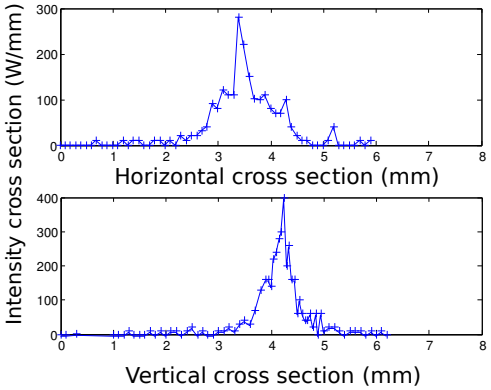

Figure 5.14: The beam cross section 13.5 mm from the diode face.

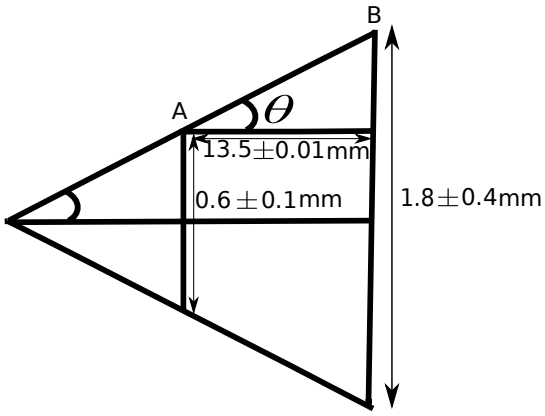

Figure 5.15: Vertical cross section of A and B.

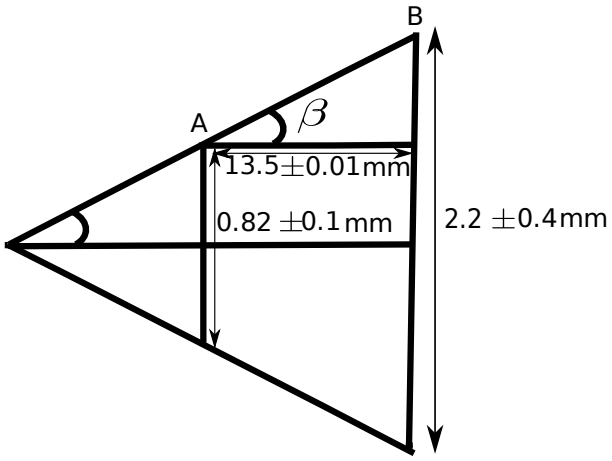

Figure 5.16: Horizontal cross section of A and B.

Pulsed Pumping of the Laser.

To decrease the chance of damage, the pump power was initially pulsed at a high power of 147 mW rather than applied continuously. The optimum duty cycle was about 10% at 5 Hz. Any lower duty cycle than this value was insufficient to create a population inversion. This value was determined by looking at the emission from the Er^{3+} and increasing the duty cycle of the pump pulse until the emission saturated. This pulse can be seen in Figure 5.17 and 5.18 as a green trace. Figure 5.17 is just before the laser starts lasing. There is also a small signature of the fluorescence on the blue trace, which is measured by a photo detector looking directly into the lasing path. With further alignment, as shown in Figure 5.18, lasing is observed at the end of the pump pulse (blue trace). It is at the end of the pump pulse because inversion needs to build up to a critical level before lasing occurs. With improved alignment, the laser starts to lase earlier along the pulse. Once

the maximum duration of lasing within the pump pulse is reached, the pump power is lowered to just above the threshold. This value is used for continuous wave operation. This procedure minimised the amount of heat going into the glass.

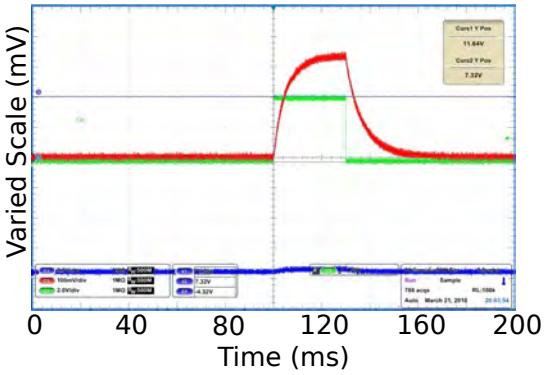

Figure 5.17: Oscilloscope trace shortly before the laser is lasing. The red trace is spontaneous emission from the sample. The green trace is the input voltage into the pump controller. The length of the pulse is the duration of the pump. The blue trace is the output from the laser.

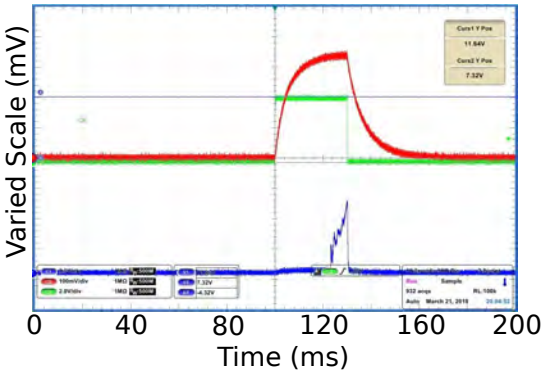

Figure 5.18: Oscilloscope trace when the laser is lasing. The red trace is spontaneous emission from the sample. The green trace is the input voltage into the pump controller. The length of the pulse is the duration of the pump. The blue trace is the output from the laser.

5.3.2 Relaxation Oscillations

It was noticed that the laser power has a tendency to oscillate (spike) in intensity in both continuous wave and pulsed pump mode. This is due to relaxation oscillations. The relaxation oscillations observed are caused by noise in the system such as mechanical vibration, acoustical, thermal noise and pump noise [82]. This effect was first observed in ruby lasers [83]. It is particularly pronounced in lasers with a high spontaneous emission life time such as ruby which has a lifetime of 2 ms, and even more so in the Er^{3+}-Yb^{3+} laser having a lifetime of 8 ms. This effect is also observed in Nd:phosphate but it diminishes quickly because of the short lifetime of 330 μs. Figure 5.19 shows the observed relaxation oscillations. The regular spikes are indicative of single mode operation and similar to what has been observed in ruby lasers [84, 85]. There is also some competition between the modes in the laser that can cause the laser to mode jump as shown in Figure 5.20. The mode jump changes the periodicity of the intensity spikes as different modes use slightly different gain due to the shape of the gain curve. If the mode has slightly higher

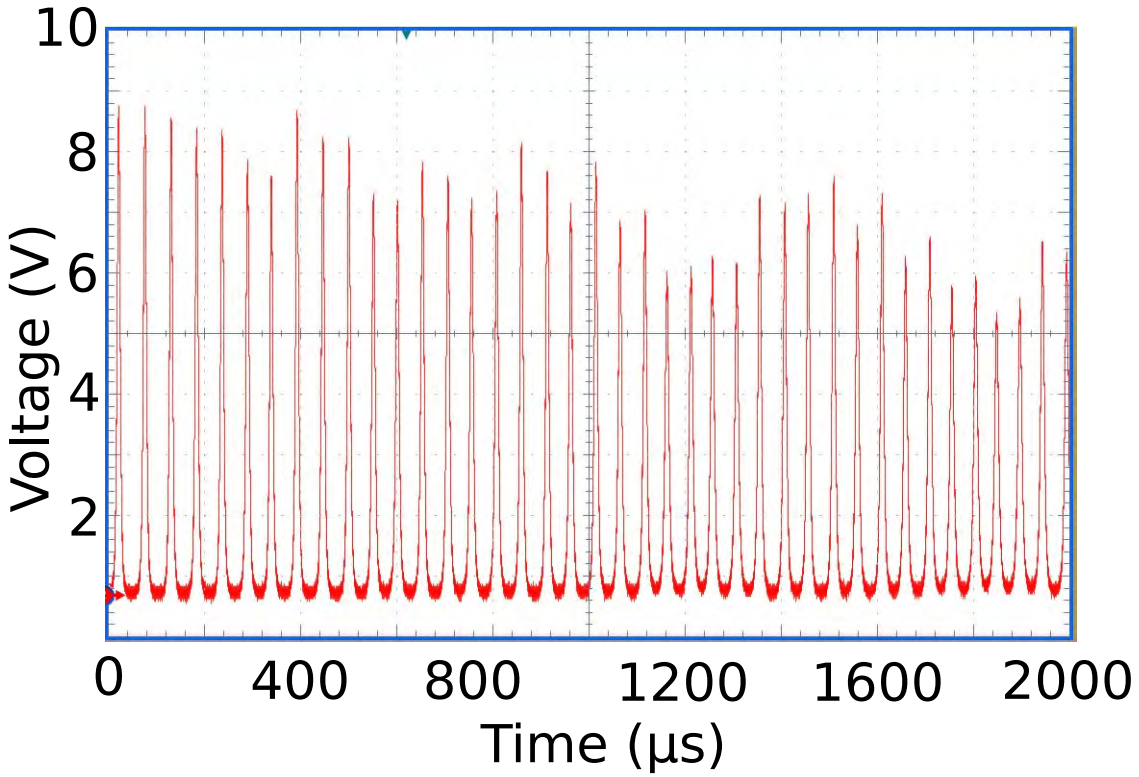

Figure 5.19: Relaxation oscillations observed in the Er^{3+}-Yb^{3+}:phosphate glass linear laser.

gain, the period of the spikes is shorter and vice versa.

The available gain for a given mode can be also changed by varying the pump power. Figure 5.21 shows the effect on relaxation oscillations of changing the power. As the pump power increases, the period is observed to decrease. When the laser is not lasing (between the spikes), the population inversion builds up to a critical point and a rapid depopulation occurs, causing a spike. When the power is increased the critical point is reached sooner, hence the decrease in the period of the spikes. When the spikes are put through the spectrometer, a spectrum is obtained as shown in Figure 5.22.

During the observation of the spikes, the pump power is kept constant. Each scan of the spectrometer produces different wavelengths. This indicates that the inversion in the laser changes rapidly during spiking causing the gain curve to change allowing for a wide range of wavelengths. It is clear that the relaxation oscillation is required to be eliminated or minimised for a stable solid state gyroscope to be developed. To minimise the oscillation the noise processes that may trigger this behaviour such as external vibration and air currents were investigated. In our experiment the main contribution to the noise was identified to be the pump diode. There was a 2.5 Hz periodic signal present in the signal. The noise was identified to be flickering of the laser diode itself and the periodic signal was

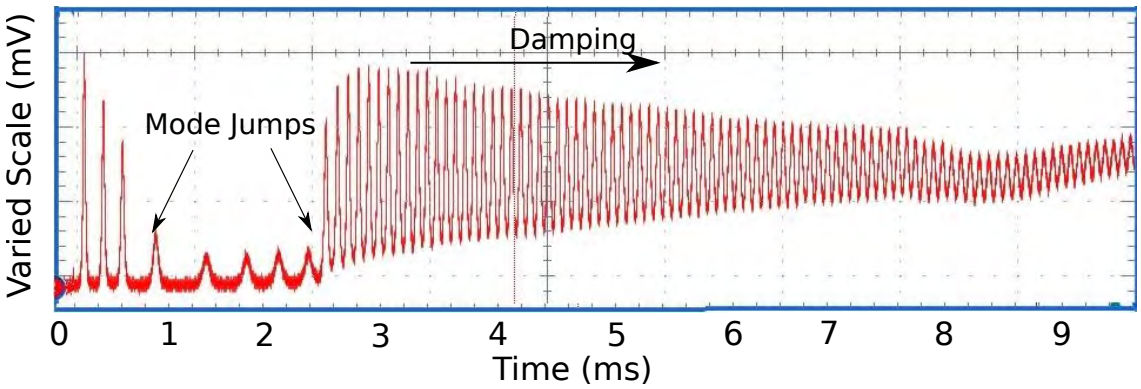

Figure 5.20: Relaxation oscillation combined with mode hops. The mode hops result in a change in the period of oscillation. The figure also shows damping of the relaxation oscillation from 3 ms onwards.

due to oscillations in the temperature controller. Initially, the problem looked like it was caused by inability of the heat sink to cool the photodiode but the problem persisted even at higher set temperatures (i.e 30 degrees). The laser diode controller was then bypassed to check the individual outputs from the thermistor and the thermoelectric cooler and the diode was powered by a bench top power supply. During the investigation the laser diode was optically damaged, probably due to a surge in current. This led to the purchase of a new diode of the same type, which did not have the same noise problem. Stable continuous wave operation was then possible.

.

5.3.3 Saturation of the Gain Medium

Since there is a finite number of erbium ions present in the lasing mode volume, at a certain pump intensity the observed fluorescence will start to saturate.

This is particularly important for the Er^{3+}-Yb^{3+} system due to its comparatively low gain (Figure 5.8). If the gain is saturated any extra pumping will only increase the temperature of the glass. The experimental set-up to measure the saturation is the same as the one used in Figure 4.11. The spectrum obtained from the experiment is shown in Figure 5.23.

Plotting the peak fluorescence as a function of pump power yields Figure 5.23. A quadratic is fitted to allow smoothing and extrapolation. The fluorescence peaks at a pump power ∼127 mW. This value gives the highest usable pump power. Any power higher than this, will mostly contribute to heating. This effect is indirectly observed.

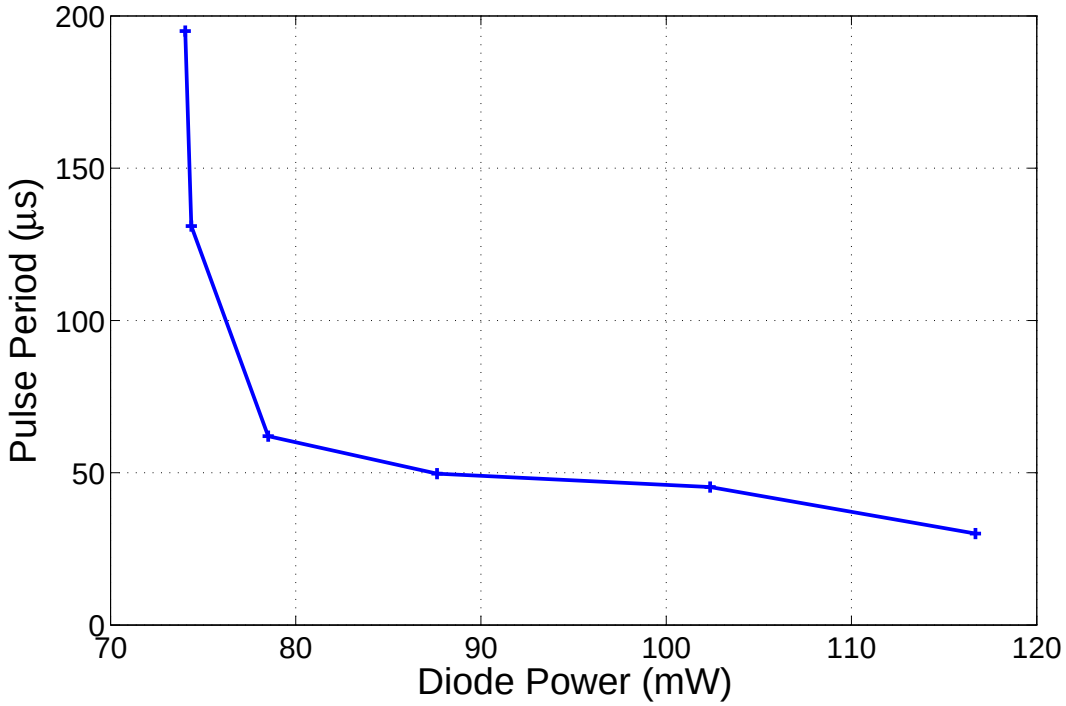

Figure 5.21: Change of the pulse period with power for the Er^{3+}-Yb^{3+} laser.

When the pump power is increased beyond saturation the laser does not increase in its power output but the intensity becomes unstable, likely caused by thermal effects.

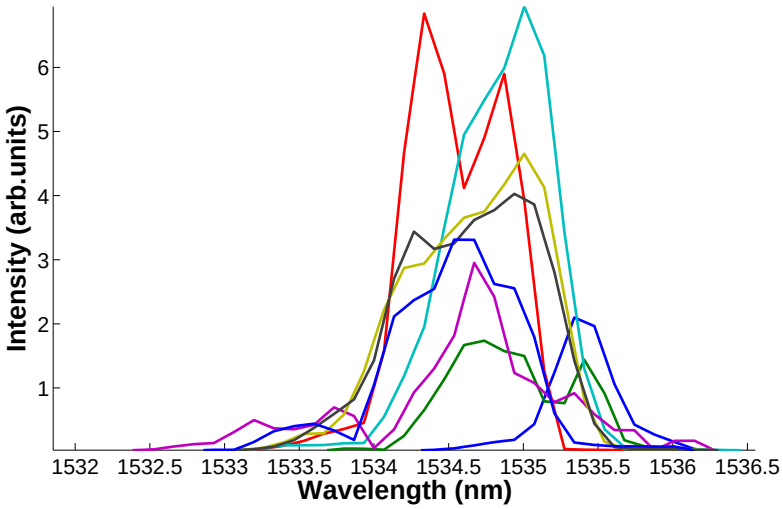

Figure 5.22: Variation in the laser output wavelength during relaxation oscillation. Each scan is taken at a different time while all other parameters are kept constant.

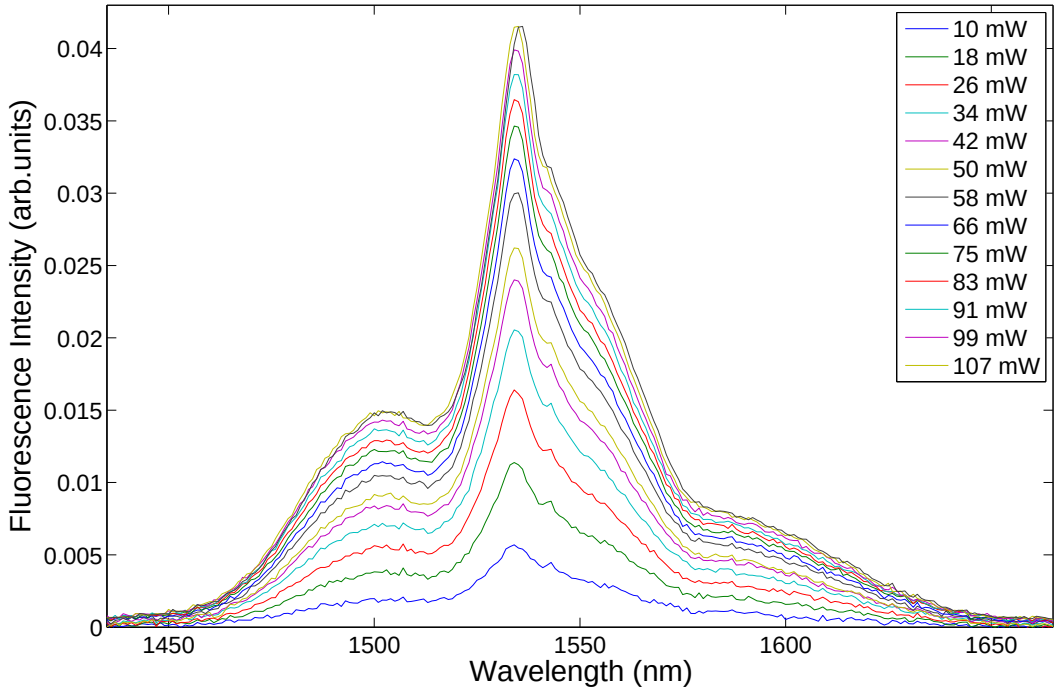

Figure 5.23: Room temperature ${}^4I_{\frac{13}{2}} \rightarrow {}^4I_{\frac{15}{2}}$ fluorescence spectrum of the Er^{3+}-Yb^{3+}:phosphate glass gain medium. The spectra have been measured for pump powers between 10 mW and 107 mW, at an increment of around 8 mW.

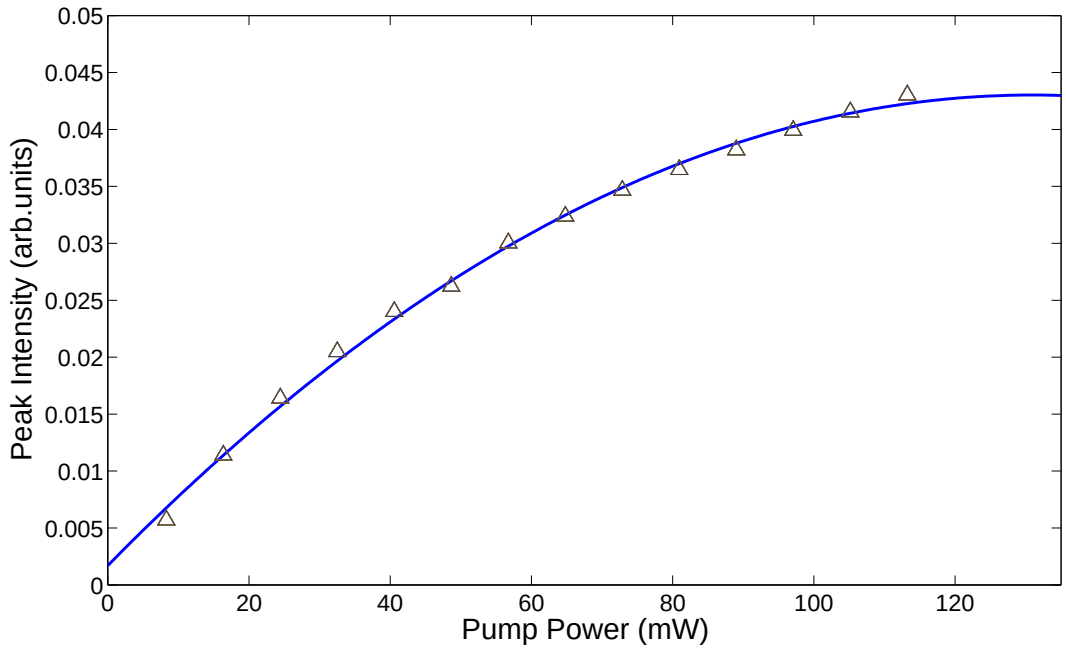

Figure 5.24: Peak fluorescence intensity versus pump power for the Er^{3+}-Yb^{3+}:phosphate gain medium. The solid line is a quadratic fit.

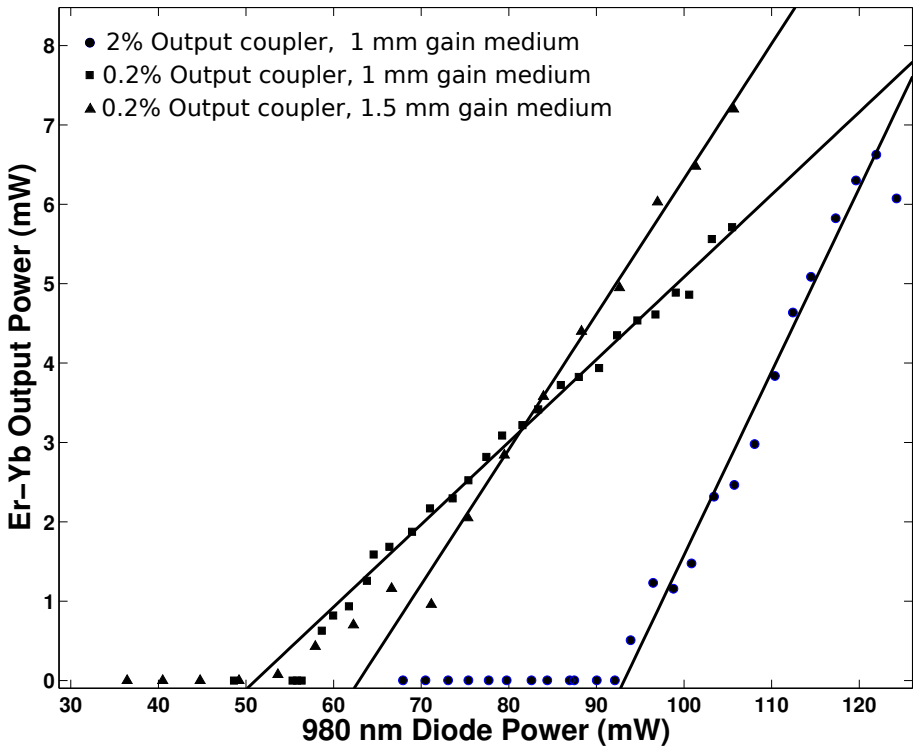

Figure 5.25: The measured laser output power of the Er^{3+}-Yb^{3+}:phosphate linear laser for various diode powers and using different output couplers and gain media.

5.3.4 Lasing Performance

Once the relaxation oscillations were eliminated the output power was stable enough to be measured. The measured output power for lasers with different output couplers and using gain media with different lengths is shown in Figure 5.25. The highest slope efficiency of 23 % is given by the 2 % output coupler with a 1 mm gain medium, it also gives the highest lasing threshold of 92 mW. This high efficiency is due to the high output coupling compared to the other two set-ups. Consequently, the losses inside the cavity are also higher so it requires greater pump intensity to reach the lasing threshold. The lowest efficiency of 10.4 % is shown by the 0.2 % output coupler. It also has the lowest threshold due to the low intra-cavity loss. The system with longest gain medium has a slope efficiency of 18 % and a threshold of 62 mW. The higher threshold is due to greater absorption and scattering loss due to increased length.

5.3.5 Multi Wavelength Emission

Another feature of the Er^{3+}-Yb^{3+} laser system is the ability to lase at different wavelengths depending on the cavity losses. These losses can be changed by using different output couplers. From Figures 5.6 and 5.7 we see that the shape of the gain curve changes for different inversion levels. When the inversion is below 70 % the region around 1555 nm has greater gain than the region around 1534 nm. Even though this applies only at threshold, if we assume the line is predominantly homogeneously broadened it will be approximately correct for higher pump powers as well [73]. This approximation is valid since the wavelength of the laser does not change with pump power. This experiment also provides a tool to measure the inversion directly by observing the wavelength. The lasing spectra are shown in Figure 5.26.

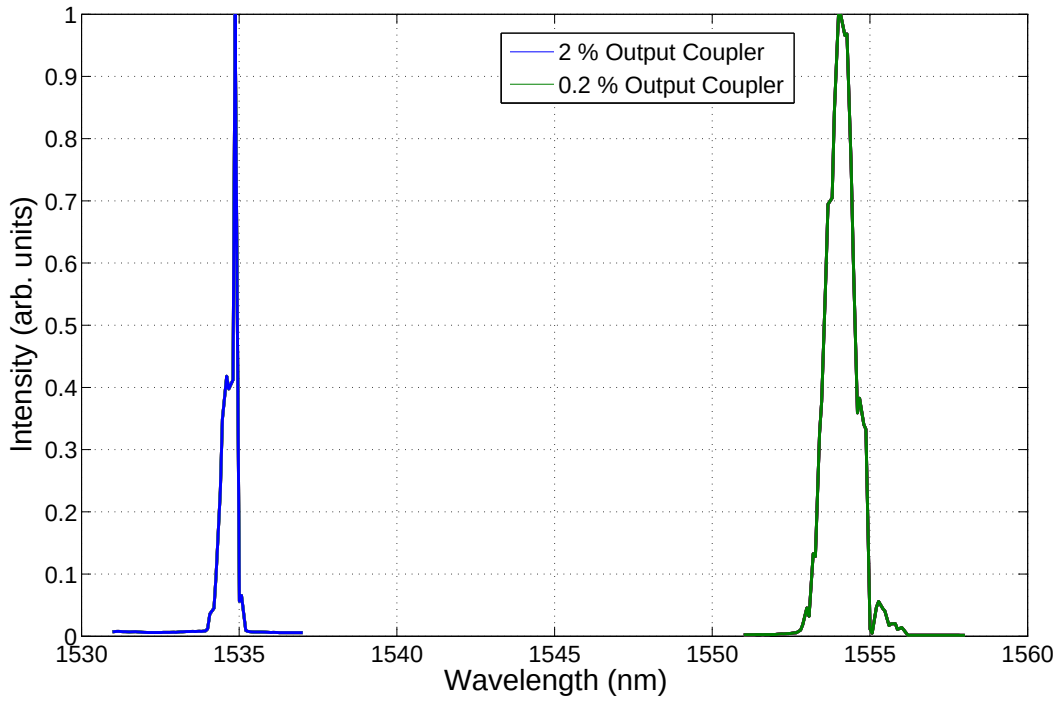

Figure 5.26: Laser spectra for the Er^{3+}-Yb^{3+} linear laser for different intra-cavity losses.

5.3.6 Scattering due to the Gain Medium

Scattering by the gain medium's surfaces increases the losses inside the cavity. To measure this scattering loss the experiment shown in Figure 5.27 is used. Fortunately, Er^{3+}-Yb^{3+} does not have an absorption line at 632.8 nm [86], so a red He-Ne was used as a probe beam. Iris (I1) and (I2) were about three times bigger than the laser beam diameter

to remove any excessive scattering from the probe laser itself, while (I3) removes the scattering from the glass. The power is measured at the points shown in the diagram and used to calculate the scattering loss. (P3) is the input power into the gain medium and it is taken away from the reflection losses (P2) and transmission losses (P1). (P1) and (P2) were measured sufficiently far away from the laser to minimise the effect of scattered light on the measurements.

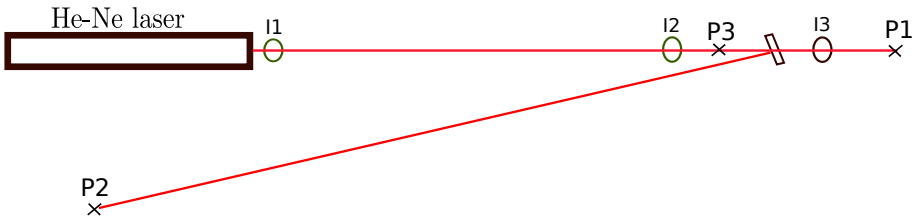

Figure 5.27: Experimental set-up to measure scattering within the laser glass. (I1), (I2) and (13) are irises. (P1), (P2) and (P3) are the locations of the power meters.

We assumed the dominant scattering process in the glass is Rayleigh scattering. The amount of light lost was measured as 1.1 % at 632.8 nm which translates to 0.03 % (using the Rayleigh scattering power law) at 1534 nm for the 1 mm and 0.05 % for the 1.5 mm gain medium. Using this information it is possible to calculate total gain-losses in the cavity.

For a 1 mm gain medium with a 0.2 % output coupler which emits at 1555 nm the maximum inversion is 70 % (see section 5.3.5). From Figure 5.6 the percentage single pass gain is 1.5 % so the round trip gain is 3 %. The total scattering loss from the gain medium is 0.06 % (double pass). The total loss from the cavity mirrors is 0.4 % (two 0.2 % mirrors). The overall percentage gain in the system is: 3 %-0.4 %-0.06 %=2.5 %. This ignores any reflection losses since the sample is anti reflection coated. If we assume the same amount of inversion for a 2 % output coupler with other mirrors being at 0.2 % loss, the overall gain is 0.4 %. However it is known from section 5.3.5 that the inversion is greater than 70 %. Thus if we take the inversion to be 100 % then the round trip gain is 8.4 % which gives the overall gain of 6.1 %. It not realistic to be able to achieve 100 % inversion especially in a 3 level system, so the overall gain will be lower than this. For a 1.5 mm sample the overall gain is 4.1 % at 70 % inversion with a 0.2 % output coupler and 10.1 % at 100 % inversion for a 2 % output coupler .

5.3.7 Transverse Laser Modes

It was possible to produce the transverse modes TEM_{00}, TEM_{01}, TEM_{02}, TEM_{03} and TEM_{04}. Combinations of these modes were also observed. Lower order modes are observed in the Er^{3+}-Yb^{3+} system compared to Nd system due to much smaller overall gain. The different modes were produced by changing the power and fine[2] alignment of the pump, which changes the gain cross section area. To observe the TEM modes a fluorescent card was placed into the path of the laser beam and a photo was taken of the card. By looking at the saturation of the pixels it was possible to produce the intensity pattern for each of the main modes, which are shown in Figure 5.28.

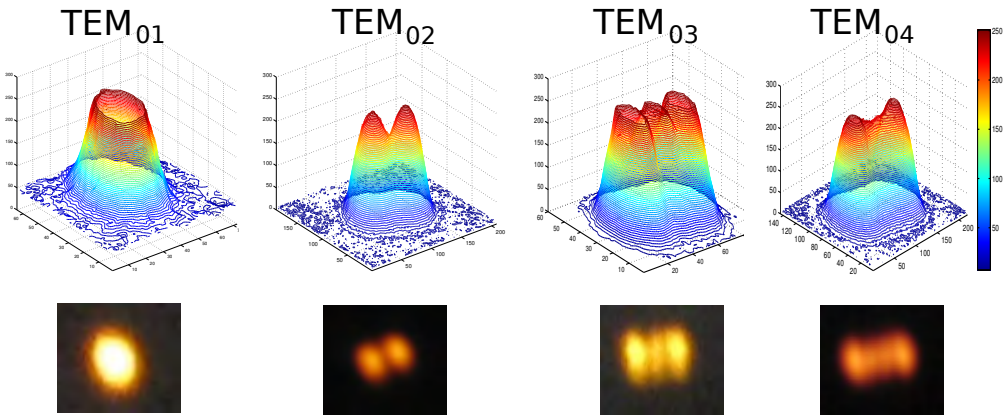

Figure 5.28: Transverse modes observed for the Er^{3+}-Yb^{3+} phosphate glass laser.

5.4 L-Cavity

As with Nd^{3+}:phosphate an L-cavity laser was built as a step towards the ring laser. Due to the low gain it is a significant step. When the third mirror is added the round trip losses increase not only from the extra added mirror but also from extra reflections by the middle mirror. Figure 5.29 shows the constructed laser. The cavity dimensions are the same as the Nd:phosphate L-cavity laser, so the same stability condition applies. It was only possible to get the laser working in a pulsed pump mode. The lasing threshold was 106 mW. From Figure 5.24 this is close to the saturation point. It was more time consuming to align than the Nd^{3+}:phosphate ring due to finer tolerances. During an attempt to run the laser in continuous mode, the high power from the diode caused the glass to fracture. The curved mirror (M2) used in the cavity was unpolarised and hence will have higher loss than the s-polarised mirrors (Figure 5.30).

[2]Fine tuning is done by a vernier attached to the translation stage that the pump is mounted on.

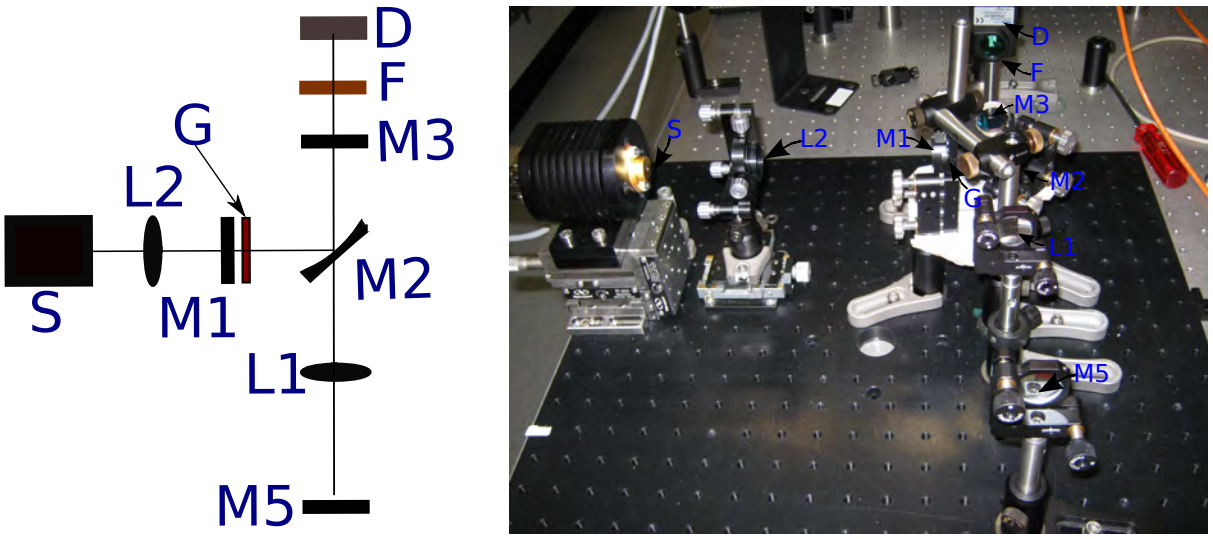

Figure 5.29: Schematic of the constructed Er^{3+}-Yb^{3+}:phosphate L-cavity laser. M2 is a concave mirror with a radius of curvature of 7.5 cm. M3 and M2 are planar cavity mirrors. L1, L2 are lenses with focal lengths of 12.5 cm and 5 cm. F is a λ= 1000 nm high pass filter. D is a germanium photodiode. S is the 980 nm laser diode. G is the gain medium.

5.5 Ring Laser Cavity

The ring laser was built using s-polarised mirrors. The s-polarised mirrors were supplied by Laser Components^{TM} and were guaranteed to have losses less than 0.1 %. With this performance a ring cavity was attempted. The total loss from the four mirrors will be less than 0.4 %. In the ring, the gain is halved compared to the linear and L-cavity for the same gain medium because of the single pass per round trip. For a ring cavity using a 1 mm gain medium the total loss is less than 0.43 % taking into account the scattering loss and 0.1 % loss for each mirror. Even at 70 % inversion the total gain is around 1.5 %, so the overall gain in the system is around 1 %. This makes the building tolerance small compared to Nd^{3+}:phosphate which has a gain of 175 % at 70 % inversion. It was easier to build a ring using the 1 mm sample than 1.5 mm as 1 mm sample has a lower lasing threshold.

5.5.1 Cavity Design

The dimensions of the ring laser are the same as the Nd^{3+}:phosphate ring laser except that extra lenses (L2) and (L3) are added to correct for astigmatism of the alignment beam. This addition is required to improve precision of the alignment. The alignment beam was a red He-Ne laser instead of a green He-Ne as the mirror coatings were better

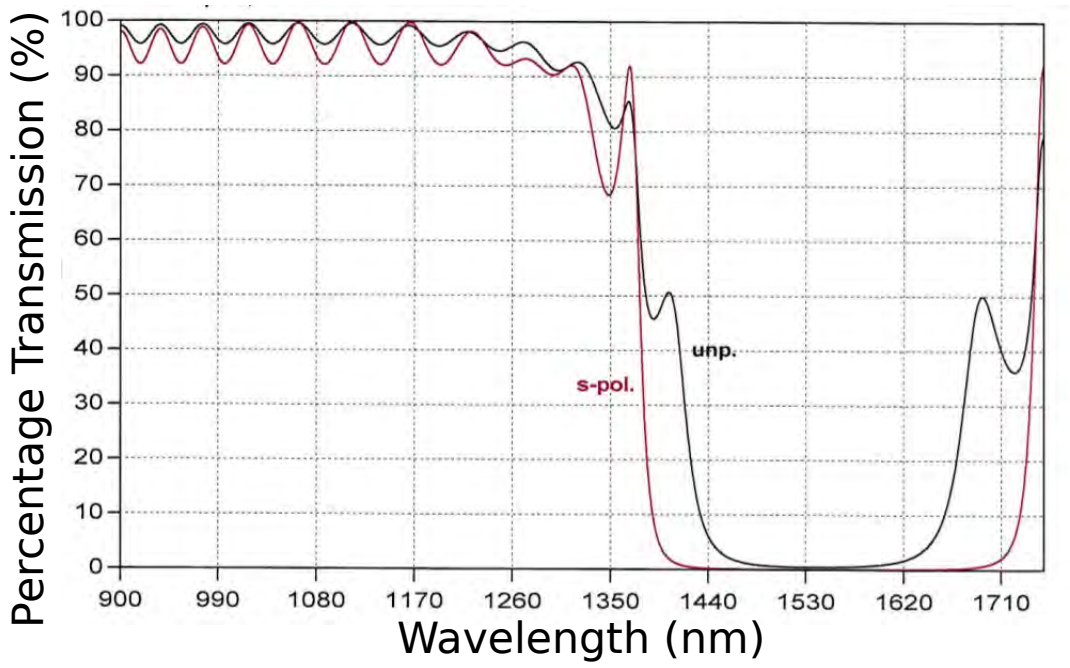

Figure 5.30: Comparison between 45^o un-polarised and s-polarised mirrors. The figure was supplied by Laser Components^{TM}.

at reflecting the red beam. Also, a beam combiner is not added as it is possible to obtain the Sagnac frequency directly from the monobeams. Furthermore, alignment of a beam combiner is difficult without large area cameras which are responsive to 1.5 microns. A photo and the schematic of the ring laser is shown in Figures 5.31 and 5.32.

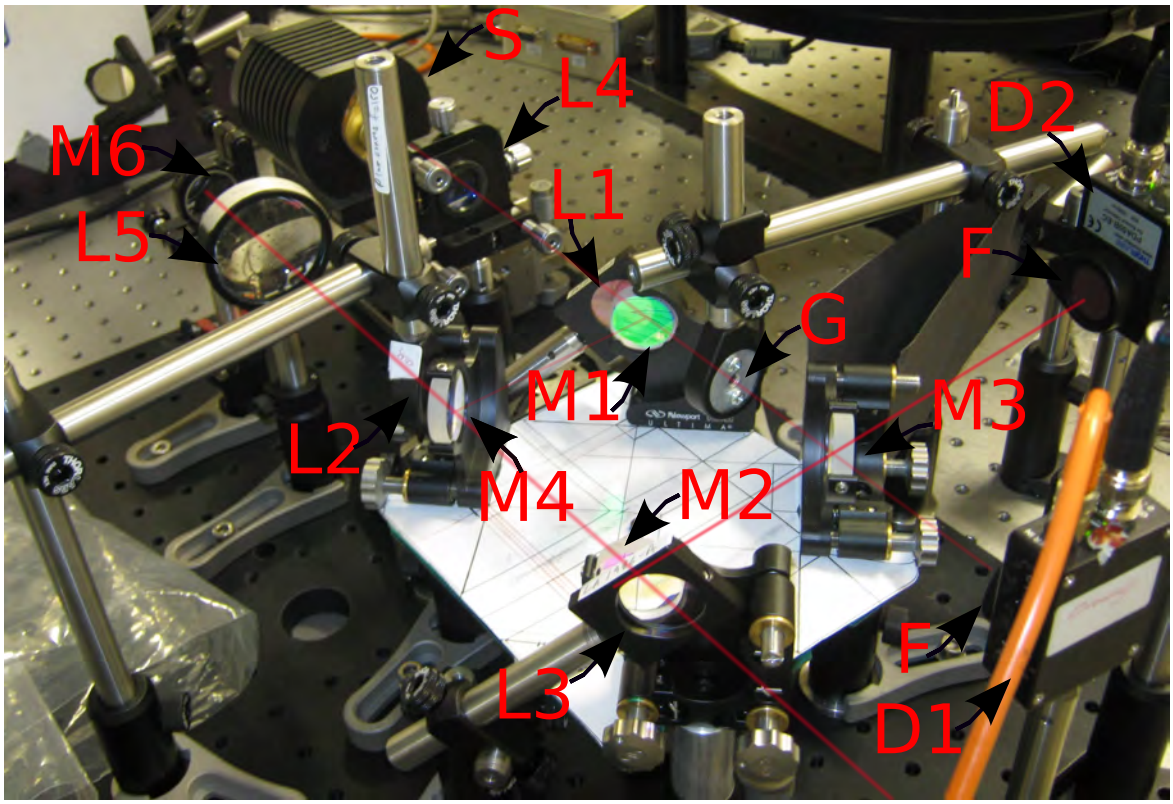

Figure 5.31: The Er^{3+}-Yb^{3+}:phosphate glass ring laser. Mirror (M1-4) are concave mirrors with a radius of curvature of 7.5 cm. F is a long pass filter at 1000 nm. Mirrors (M5-6) are planar mirrors. The mirror (M6) and lens (L5) are used to back reflect the alignment laser. (S) is the pump laser diode and (L4) is used to focus the pump beam. (L1-3) are used for astigmatism correction. (D1-2) are detectors. Finally, (G) is the gain medium.

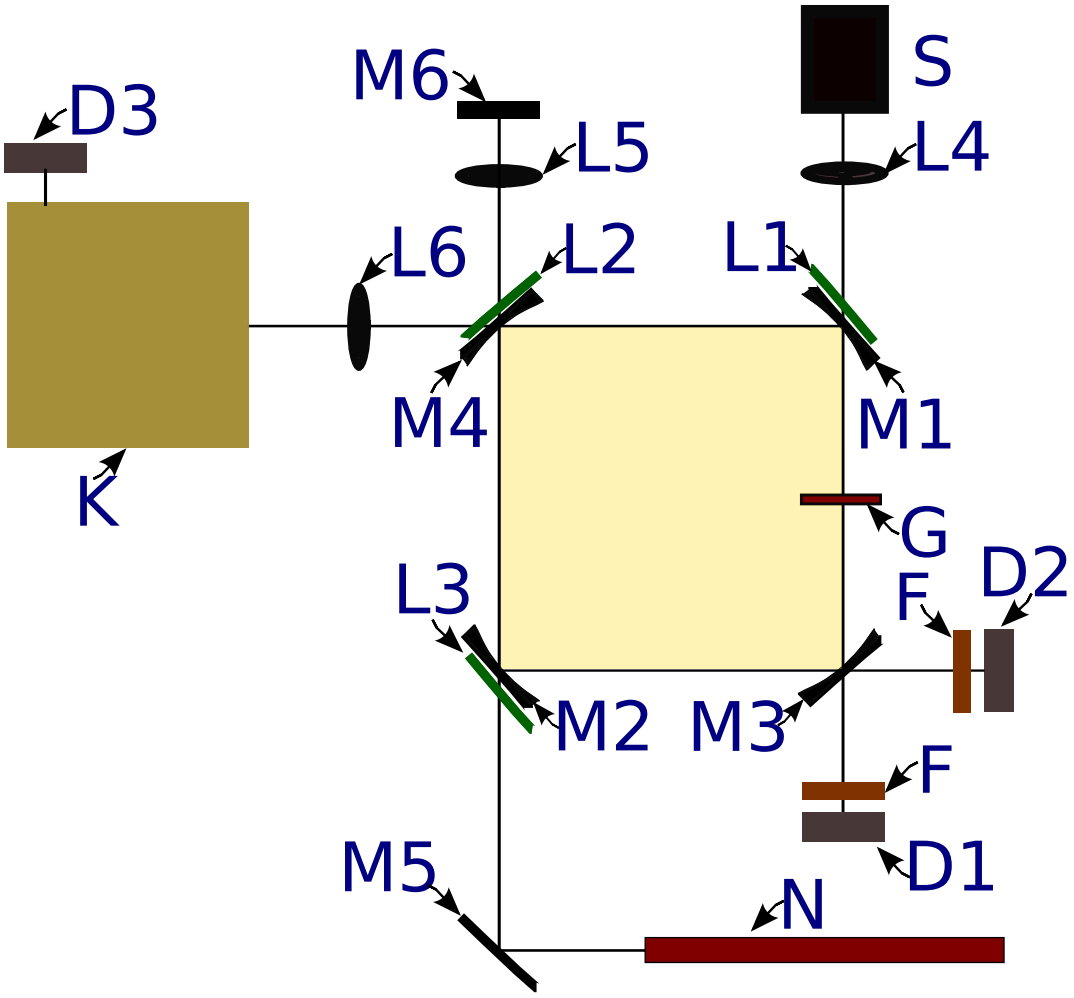

Figure 5.32: Schematic of the Er^{3+}-Yb^{3+}:phosphate glass ring laser . Mirrors (M1-4) are concave mirrors with a radius of curvature of 7.5 cm. F is a long pass filter at 1000 nm. Mirrors (M5-6) are planar mirrors. The mirror (M6) and lens (L5) are used to back reflect the alignment laser. (S) is the pump laser diode and (L4) is used to focus the pump beam. (L1-3) are used for astigmatism correction. (D1-3) are detectors. (L6) is to focus the laser into the spectrometer. (K) is the spectrometer. (N) is the red He-Ne laser. Finally, (G) is the gain medium.

5.5.2 Ring Output

Initially, it was only possible to make the ring laser lase with pulsed pumping. Figures 5.33 and 5.34 show just before and after the laser lased. The blue trace shows emission from the erbium-ytterbium glass. The red trace is the timing pulse into the pump laser controller.

Figure 5.33 shows the fluorescence emission. The amplification around the cavity

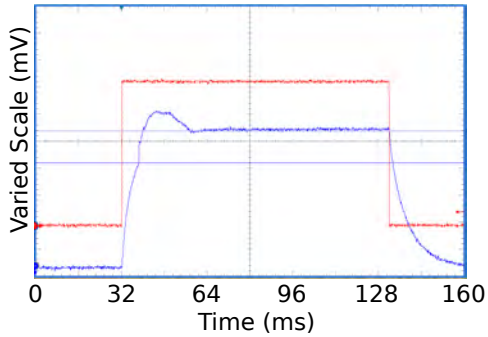

Figure 5.33: Amplification by the ring cavity is shown by the small peak in blue. The red trace is the pump.

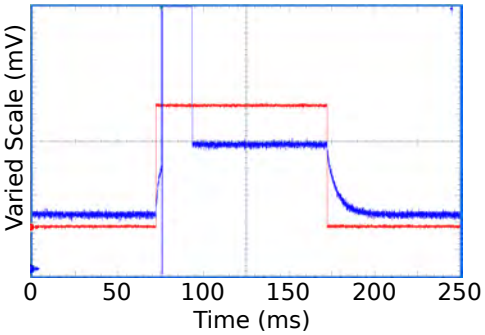

Figure 5.34: The blue trace is the Er^{3+}-Yb^{3+} ring lasing and saturating the detector. The red trace is the pump.

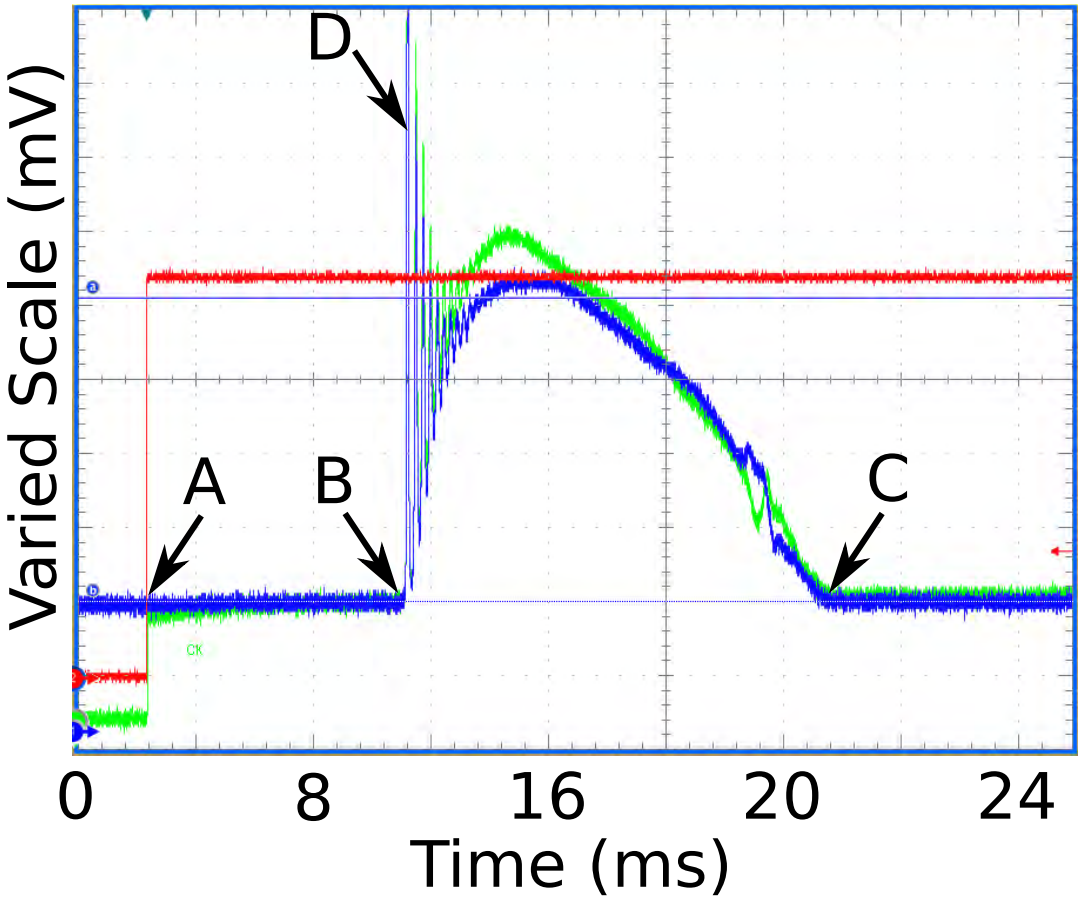

Figure 5.35: The pulsed output from the Er^{3+}-Yb^{3+} ring. Green and blue shows the clockwise and anti-clockwise beams. From (A) to (B) is the delay between the start of the pump and lasing. (D) is relaxation oscillations. (C) is the end of the Er^{3+}-Yb^{3+} pulse. The red trace is the pump duration.

and population inversion has not reached a critical point. With further alignment lasing occurs which saturates the detector (Figure 5.34). A close up of the laser pulses from the clockwise and anti-clockwise beams measured by the detectors (D1) and (D2) is shown in Figure 5.35. Once the pump is started it takes the laser a certain time to build up inversion until it lases. When it lases both beams have relaxation oscillations which dampen out eventually. It can be also be seen that in Figure 5.33, 5.34, and 5.35 before the complete duration of the pump the laser stops lasing. However, it is desirable to have the ring laser working in a continuously wave operation, which will avoid relaxation oscillation at the start of each pulse in addition to providing uninterrupted rotation measurements.

5.5.3 Continuous Wave Ring Laser Operation

For measuring rotation it is ideal to have the laser working in continuous wave mode, especially since at the start of each pulse relaxation oscillation occurs. Doing so will enable continuous rotation measurement. To do this all the controllable variables such as power, pulse duration and the temperature of the pump diode were varied, while monitoring the lasing duration. The result from varying the power is shown in Figure 5.36. The figure on the left is the peak of the relaxation oscillation, indicated in Figure 5.35 as (D). This further motivates us to pursue continuous wave lasing. The time required for the

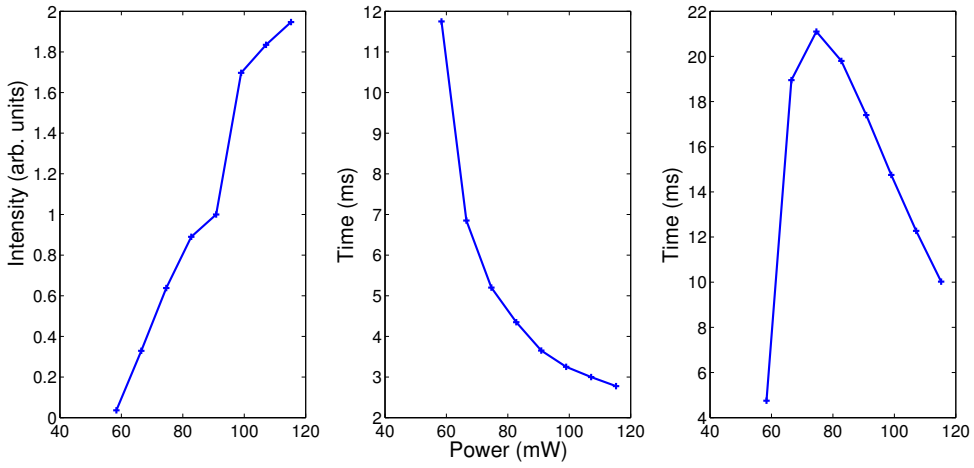

Figure 5.36: Left figure: Initial relaxation spike (D), middle: time taken for lasing to occur (A to B), right: lasing duration for varied power. The labels A to D are seen in Figure 5.35.

laser to start decreases rapidly with higher power (middle figure). This time period is shown in Figure 5.35 as A to B. The labels A to D refer to times marked in Figure 5.35. The biggest clue is given by the figure on the right, lasing duration (B to C). It shows

that there is an optimum power of 80 mW. Then the pump pulse frequency was varied. Figure 5.37 shows that as the frequency decreased the pulse duration increased. When

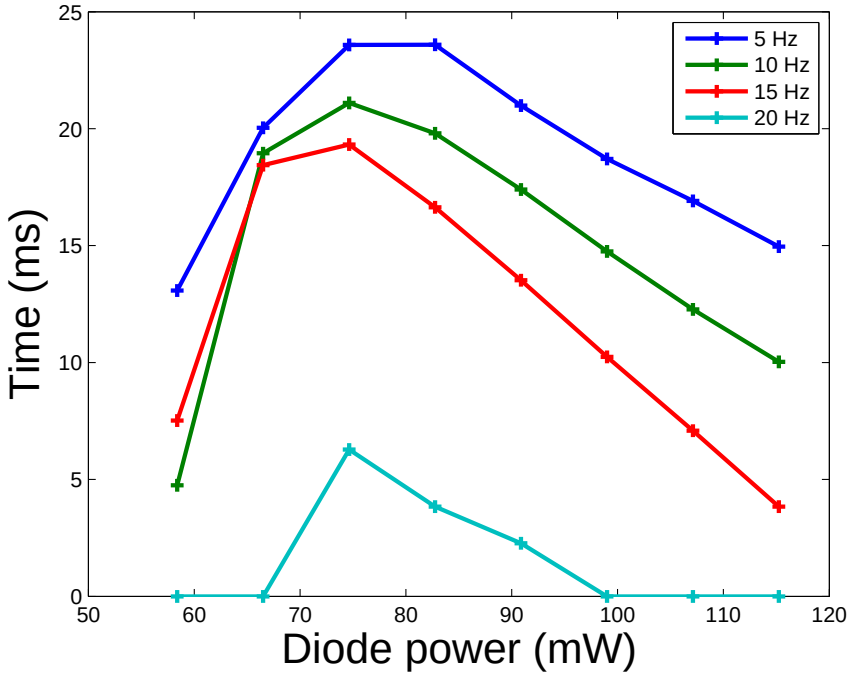

Figure 5.37: Lasing duration from (B) to (C) as indicated in Figure 5.35 for different pump rates.

the pulse frequency was 20 Hz it was only possible to start the laser at the higher powers. Also, the laser stopped working at higher power faster than at the other frequencies as seen in Figure 5.38. This effect only lasted for couple of minutes then the laser stopped working completely. For any frequency above 20 Hz the laser did not lase. This is a strong indicator that there was heating occurring in the glass. Finally, the pump temperature was varied. Up until now the temperature of the diode pump was held at 14.2 ^{0}C. For these measurements we combined the fact that the laser runs longer for lower frequencies and optimum power. It was observed that at frequencies below 5 Hz the optimum power was 72.5 mW.

To see if the observed behaviour was caused by up conversion effects an Ocean Optics USB2000 fibre fed spectrometer was placed near the gain medium and the spectrum was recorded for different pump powers. The pump pulse rate was 10 Hz and an integration time of 50 ms was set on the spectrometer. The result is shown in Figure 5.39. It shows that there is only a linear increase in up-conversion with power for all wavelengths. This rules out any additional excessive losses in the cavity. Figure 5.40 shows the lasing duration for different pump diode temperatures. Laser performance is semi-optimum at

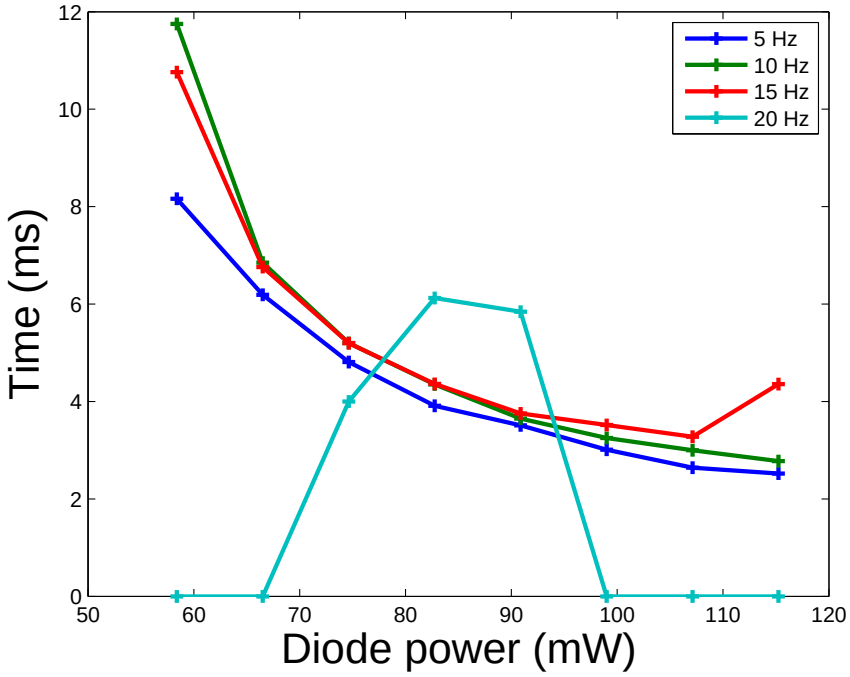

Figure 5.38: Laser start up time from (A) to (B) as indicated in Figure 5.35 for different pump rates.

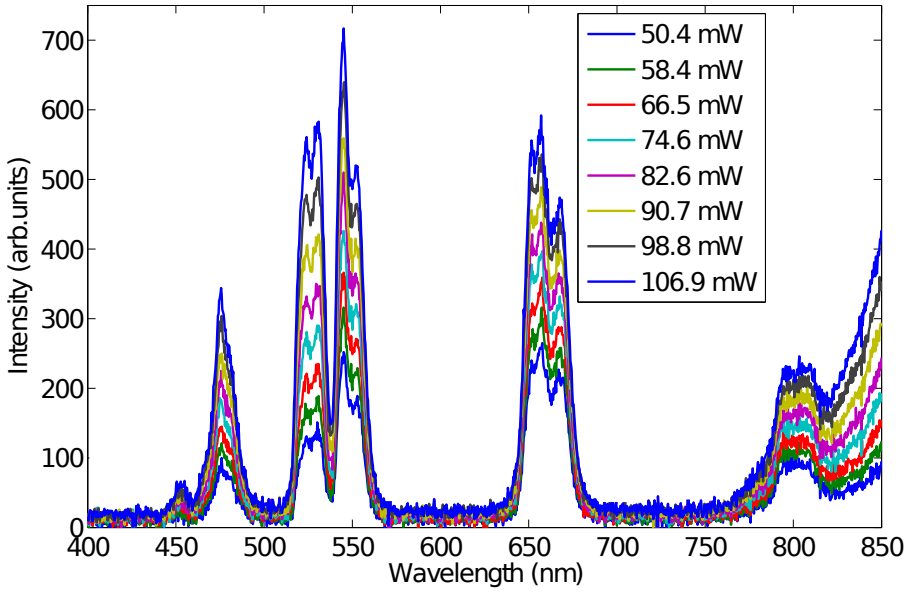

Figure 5.39: Parasitic emission from the Er^{3+}-Yb^{3+} gain medium.

11 ^{o}C. Any value lower (limited to 9 ^{o}C by the equipment) or higher causes the lasing duration to decrease until the diode temperature is near optimum temperature of 25.5 ^{o}C. At this temperature it was possible to run the ring continuous wave. When the diode

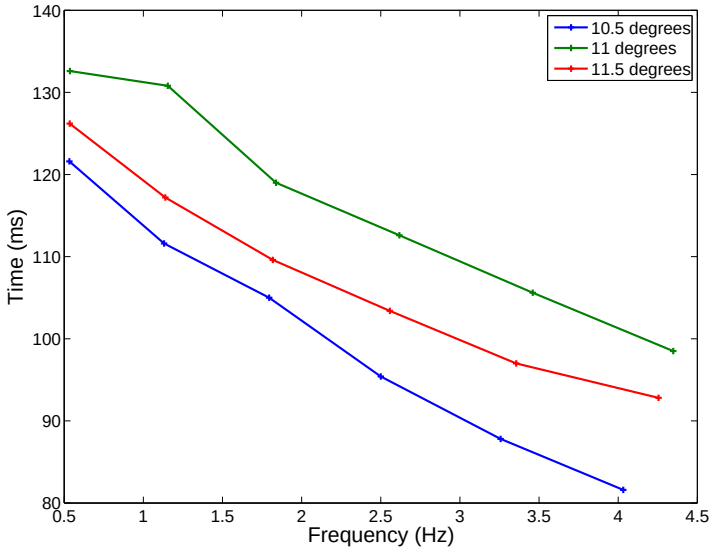

Figure 5.40: Lasing duration (B to C) as a function of pump frequency at different laser diode temperatures. The graph shows the semi-optimum temperature is 11^{o}C.

temperature was decreased or increased from 25.5 ^{o}C the ring laser's power decreased and eventually it stopped lasing. This effect is not due to changes in the pump power with temperature. For diode temperatures between 23.5 and 27.5 ^{o}C the pump power remains constant. If we look at the spectrum (Figure 5.41) of the diode at 25.5 ^{o}C there is a single

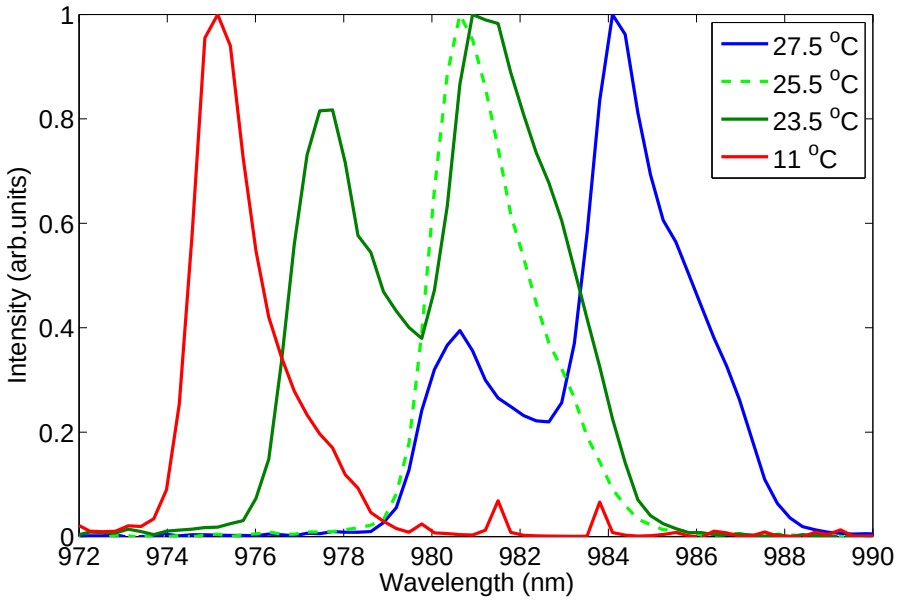

Figure 5.41: Spectrum of the laser diode pump at various temperatures.

peak. For temperatures above or below, multiple lasing wavelengths are present. This

shows greater efficiency is achieved when the pump diode has a single peak at 980.5 nm. Even though at 975 nm the diode wavelength is a single peak, it was only possible to achieve lasing through pulsed pumping. The glass was then mounted on a copper heat sink which made continuous wave operation of the laser easier. Figure 5.44 show the final set-up ready to measure rotation.

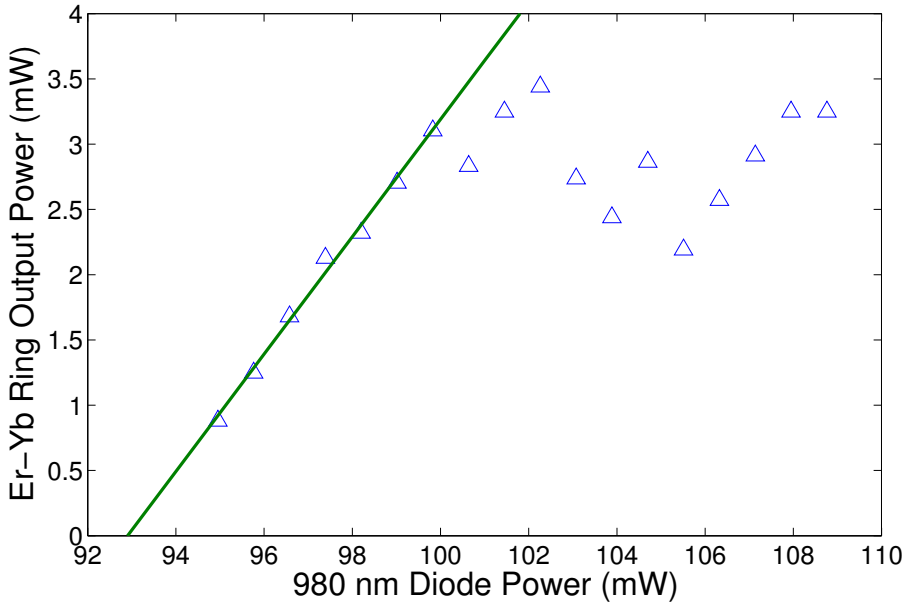

Figure 5.42: Output power of the Er^{3+}-Yb^{3+} phosphate glass ring laser. The laser becomes unstable at powers above 100 mW of pump power.

Unlike the linear erbium ytterbium laser the ring laser only works for a narrow range of pump powers. As shown in Figure 5.42 the ring lases only in the range between 93-110 mW of diode power. The lasing threshold is 93 mW. After about 100 mW the laser power fluctuates. For rotation sensing measurements, the power is kept in the region below 100 mW. The ring laser spectrum is shown in Figure 5.43. From this the inversion is inferred to be above 70 %.

5.6 Rotation Sensing Ability

The ring laser was placed on a turntable as shown in Figure 5.44. The ring was capable of rotating both ways with rotation speeds from 0 to 6.3 rad/s. The table uses stepper motors, a compromise between maximum speed achievable by the table and smooth rotation speed. Even though the table can reach 6.3 rad/s it is normally run at lower speeds
.

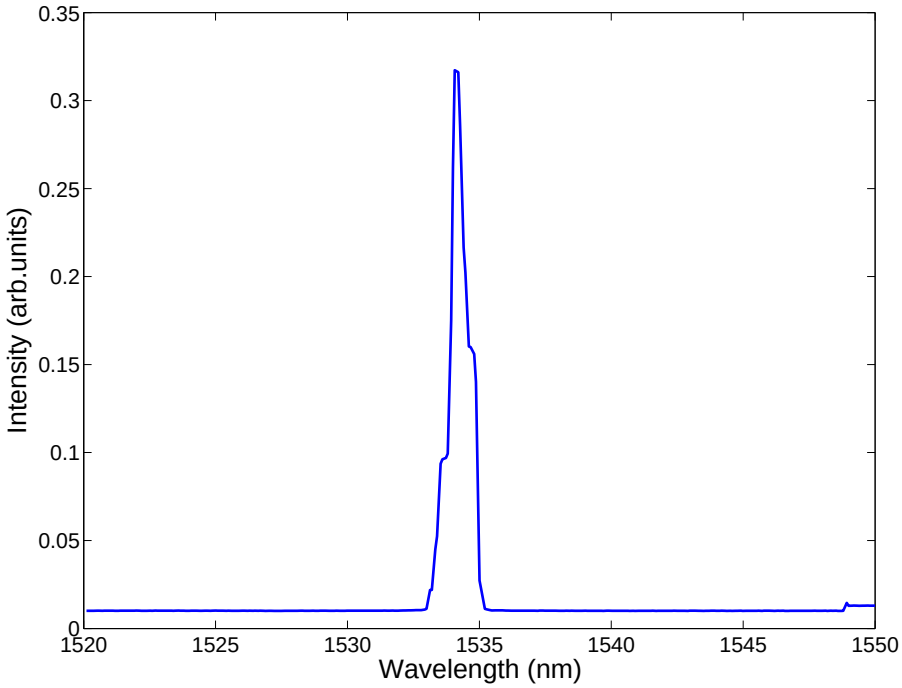

Figure 5.43: Wavelength output from the Er^{3+}-Yb^{3+} phosphate ring laser.

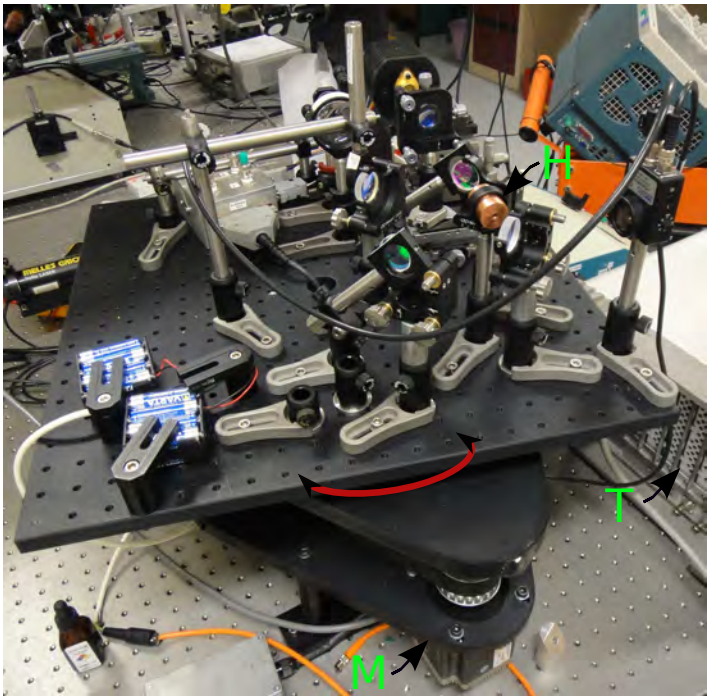

Figure 5.44: The Er^{3+}-Yb^{3+} phosphate glass ring laser gyroscope on a turntable. H is the copper heat sink. M is the steeper motor used to rotate the table. T is the radio frequency spectrum analyser.

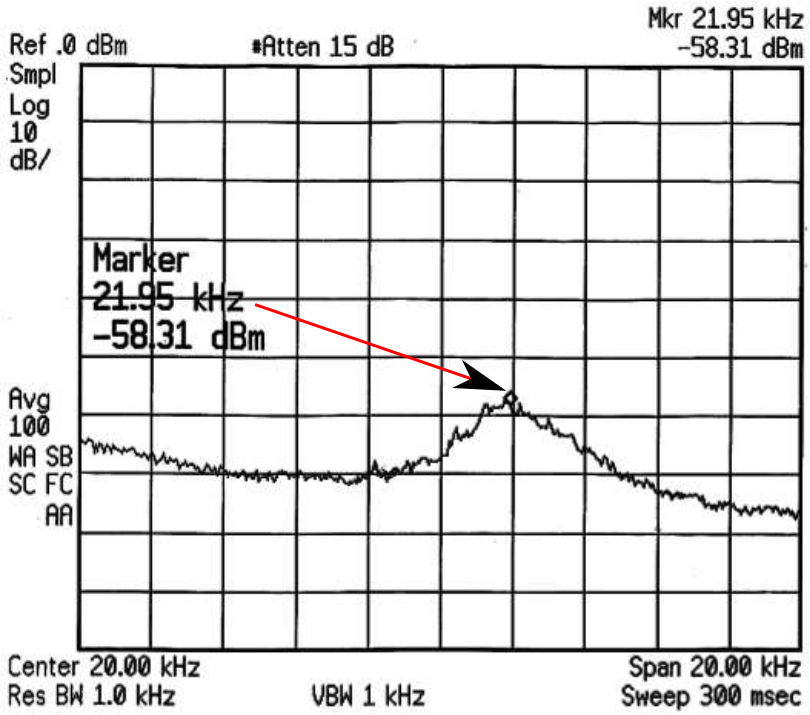

Figure 5.45: Output from an RF spectrum analyser. This measurement was taken at a rotational speed of 0.36 rad/s and has been video averaged. The peak is marked by the marker point.

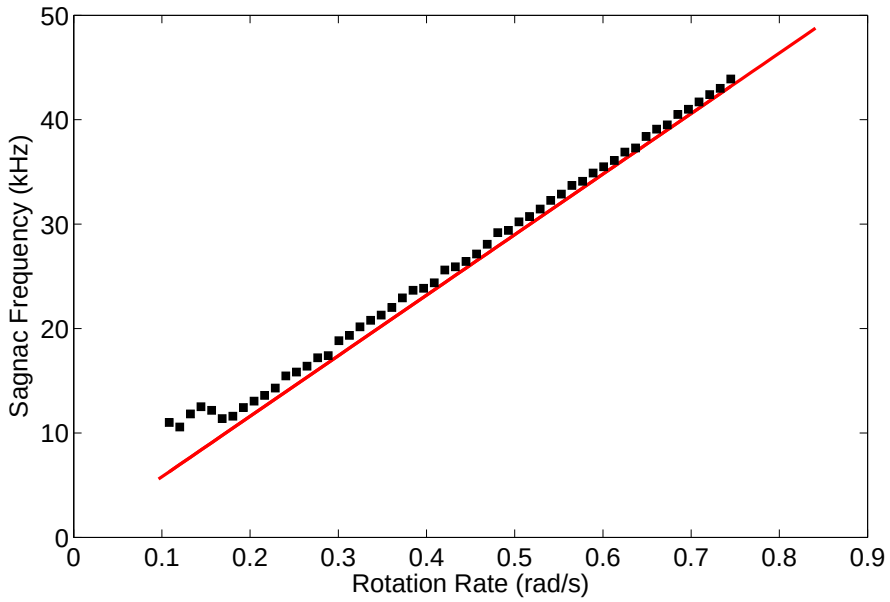

Figure 5.46: The peaks measured from the RF spectrum analyser at various rotational speeds. The Sagnac frequency plotted are peak values. For example, the marker in figure 5.45 shows one of the values.

For the neodymium ring laser it was trivial to see the beat frequency (Sagnac frequency) on clockwise and counter clockwise beams as a sinusoidal signal on the oscilloscope. This was not possible with the erbium-ytterbium ring because of the poor signal to noise ratio. Fortunately, the radio frequency spectrum analyser can detect the beat frequency from a single laser beam (monobeam) (see Figure 5.45). The output is video averaged 100 times and the peak of the signal was measured and plotted in Figure 5.46. The thick line is the theoretical line obtained from using the Sagnac formula:

$$\upsilon(\Omega) = \frac{4\widehat{\Omega}.\widehat{A}}{\lambda P} \tag{5.4}$$

where $\upsilon(\Omega)$ is the Sagnac frequency, $P = 36$ cm is the perimeter of the cavity, $A = 80$ cm^2 is area enclosed by ring, the lasing wavelength λ is 1534 nm and Ω is the rotational rate. At lower speed there is a large deviation from the theoretical line. As the rotation rate increases the measurement improves around 0.2 rad/s then slowly tends toward the theoretical line.

5.7 Comparison between the Solid State Gyroscopes

We compare the gyroscopes developed in this thesis with the published data from a Nd^{3+}:YAG ring laser. Direct comparison is possible through the difference in theoretical Sagnac frequency obtained using equation 5.4 and what was measured experimentally. Figure 5.47 shows the difference between the two phosphate gyroscopes built and the Nd^{3+}:YAG lasers built by Schwartz et al. [4].

Both the Er^{3+}-Yb^{3+} and Nd^{3+} phosphate glass SSRLs gave closer to ideal Sagnac frequency than the Nd^{3+}:YAG SSRL counterpart. The read out error is greater than 15 kHz for rotation rates between 0.1 to 0.85 rad/s for YAG, while it is less than 5 kHz for both phosphate glass based gyroscopes.

The Nd^{3+}:YAG was subsequently vibrated to decrease the effect of the gain grating [37]. This significantly improved the performance of the Nd^{3+}:YAG SSRL as shown in Figure 5.48. What is remarkable is that for low rotation rates, the performance from the Er^{3+}-Yb^{3+} and Nd^{3+} phosphate glass SSRLs described in this thesis are as good as the Nd^{3+}:YAG SSRL with the crystal vibrated. The reason for this is the use of a thin gain medium in the phosphate glass based gyroscopes (1 mm) compared to YAG (3 mm) which causes a decrease in the influence of the gain grating. This is one of the advantages of using phosphate glass: it can be doped at high concentration allowing for a thinner gain

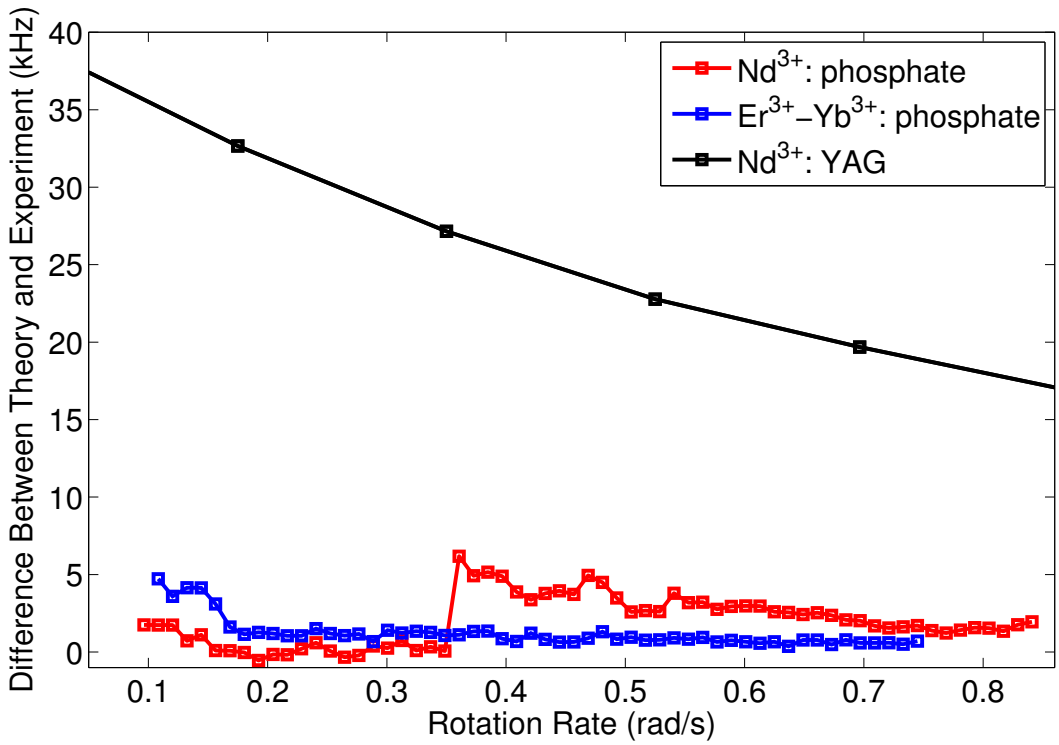

Figure 5.47: The figure shows the difference between the calculated Sagnac frequency and measured frequency. The Er^{3+}-Yb^{3+}:phosphate glass and Nd^{3+}:phosphate glass were measured in this thesis, while the Nd^{3+}:YAG data is obtained from [4]. The perimeter of the ring lasers used in this thesis was 36 cm, while the Nd^{3+}:YAG ring laser had a perimeter 22 cm. The length of the phosphate glasses were 1 mm, while the YAG crystal was 3 mm.

medium.

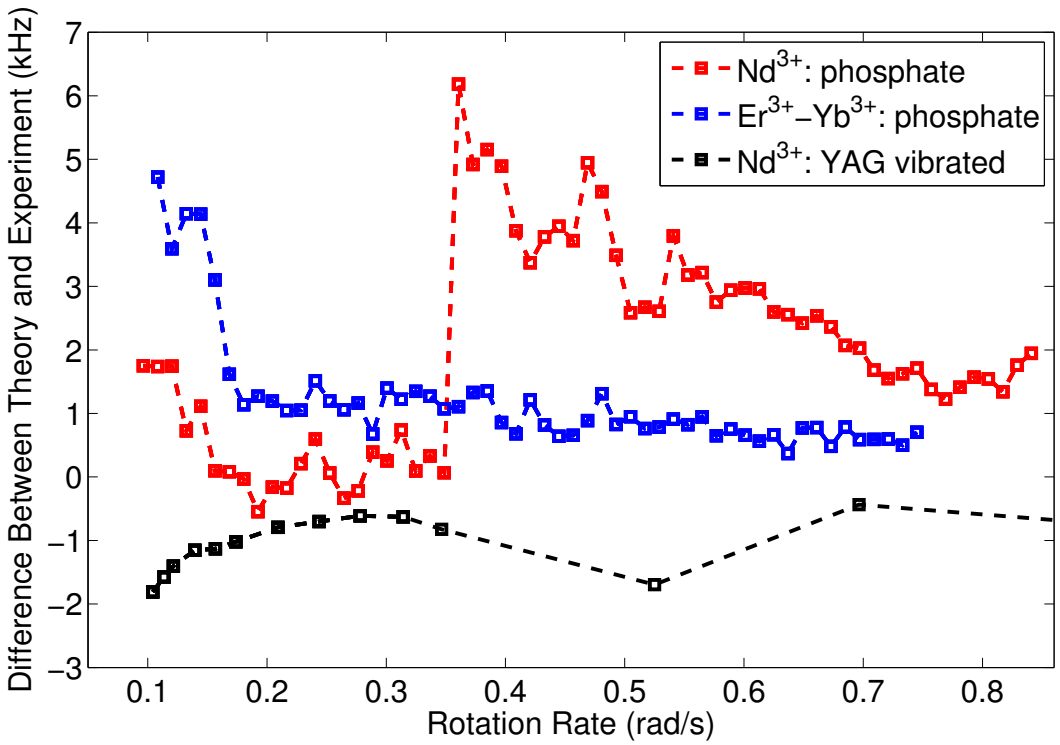

Figure 5.48: Difference between the theoretical Sagnac frequency and the experimental value for vibrated Nd^{3+}:YAG and the Er^{3+}-Yb^{3+}:phosphate glass and Nd^{3+}:phosphate glass ring laser gyroscopes. Nd^{3+}:YAG was vibrated at 168 kHz, with an amplitude of 0.47 μm. The data for Nd^{3+}:YAG was obtained from reference [4].

5.8 Conclusion

In this chapter, the construction of a laser diode pumped erbium-ytterbium co-doped phosphate glass ring laser gyroscope has been presented. Initial development focused on the construction of a linear cavity. This early design was operated in pulsed mode and exhibited pronounced relaxation oscillations due to noise in the pump laser. Ultimately, stable continuous wave laser operation could be obtained with a lasing threshold as low as 50 mW of input pump power and slope efficiency of around 10 %. Following this an L-cavity and then a ring laser were developed. The ring cavity had a perimeter of 36 cm and was operated at a lasing wavelength of 1534 nm. Due to the lower round trip gain in the ring laser the lasing threshold was somewhat higher than the linear cavity at 93 mW. Placed on a homemade turntable, this laser was subjected to external rotations to test its usefulness as a gyroscope. This is (to our knowledge) the first operation anywhere of a erbium-ytterbium phosphate glass ring laser gyroscope in continuous wave mode. The

Er^{3+}-Yb^{3+} phosphate glass gyroscope performs as well as an optimised Nd^{3+}:YAG based gyroscope. This is remarkable since the Nd^{3+}:YAG system uses high frequency (168 kHz) vibration to smooth out the gain grating. If these techniques were to be applied to the Er^{3+}-Yb^{3+} ring gyroscope superior performance would be expected. Furthermore, the vibration requirement would be significantly reduced for the Er^{3+}-Yb^{3+} ring gyroscope due to its long upper lasing lifetime.

Chapter 6

Conclusions and Future Work

One of the main results of the thesis is a successful correction of ring laser rotation rate errors caused by backscattering, hole burning, and dispersion in the gain medium. This was done by using a model to describe the behaviour of large laser gyroscopes taking into account all possible error factors. By approximation, the solutions to the differential equations which describe the coupled oscillators showed that pulling of the Sagnac frequency is caused by common mode backscatter coupling (where both backscatter components are in phase with each other) and differential mode coupling (where the backscatter vectors are in anti-phase). The differential equations were then solved numerically using a Runga Kutta method without any approximation, which agreed with the result obtained from the approximation. Using the coefficients obtained from the integration and directly measured parameters (the phase difference between the monobeams, and the monobeam modulation), correction was possible on the raw signals. The result showed an improvement in the performance of large ring lasers (PR-1 and G-0). To mimic the backscattering, a monobeam was back reflected into the cavity. This showed pushing and pulling of the Sagnac frequency for the G ring laser. Cross saturation was also directly observed.

Two solid state laser gyroscopes were built using Er^{3+}-Yb^{3+} and Nd^{3+} doped phosphate glass. These materials have never been demonstrated in a ring laser gyroscope before. A neodymium doped phosphate glass laser was initially built since this is a high gain four level laser system. As an evolutionary step toward a ring laser; linear and L-cavity lasers were built. The simple plano-concave linear cavity lased with a threshold of 180 mW and a slope efficiency of 24 % for a 1 % output coupler. An alignment technique for the ring cavity was developed including astigmatism corrections. The constructed Nd: phosphate glass ring laser successfully measured rotation. Directional switching modulation and chaotic behaviour of the ring was observed.

Using the experience from building the Nd^{3+}:phosphate lasers an Er^{3+}-Yb^{3+} gain medium was employed. Using transmission measurements from an FTIR spectrometer the absorption and emission cross section were calculated. Since the cross sections are comparable, absorption loss by the erbium ions is a major contributor in the laser cavities. Therefore it is vital to have most of the erbium ions excited. This was achieved by using a 1 mm gain medium and optimising the erbium and ytterbium concentrations. It was found that the gain medium saturated at a pump power around 127 mW, limiting the pump power used as excess pumping only increases the temperature of the gain medium. Due to the high lifetime of the upper lasing level, relaxation oscillations were observable. The constructed plano-concave linear cavities had a thresholds of 92 mW, 50 mW, 62 mW and a slope efficiencies of 23 %, 10.4 % 18 % using 2 % , 0.2 %, 0.2 % output couplers respectively. The gain medium was 1 mm thick for the laser with a 62 mW threshold which had a 1.5 mm thick gain medium. A 36 cm perimeter ring laser was then built which successfully measured rotation.

The Nd^{3+} and Er^{3+}-Yb^{3+}:phosphate laser gyroscopes gave superior performance than the published Nd^{3+}:YAG system. For rotation rates between 0.1 and 0.85 rad/s, phosphate gyroscopes give as little as 5 kHz deviation from the ideal performance while Nd^{3+}:YAG gives a 15 kHz readout error. This superior performance is caused by using a thin gain medium which decreased the strength of the gain gratings.

6.1 Future Work

Backscatter corrections have been shown to work in two large ring lasers. This method can be successfully applied to other large ring lasers.

For the neodymium based ring laser servo controlling the losses of the clockwise and counter clockwise beams will improve the range of rotational frequencies to which the device is sensitive. This method will not be effective for the Er^{3+}-Yb^{3+} ring laser since the gain is low and the range over which the losses can be changed will be limited. However, the gain of the Er^{3+}-Yb^{3+} based ring laser could be increased by using a longer gain medium and pumping the gain medium from both sides. At the moment a copper block is used as a heat sink on the Er^{3+}-Yb^{3+} glass. Running water/coolant through the heat sink will provide improved cooling, allowing for greater pump powers.

Both of the SSRLs need a solid enclosure, so all the mirrors can be mounted onto one structure, Zerodur would be ideal, but even a solid metal block would be a big

improvement. This would stop any mechanical scale factor changes. Enclosing the laser cavity into a sealed structure would stop the dust and air flowing through during the measurement improving its stability.

It would also be worth vibrating the glass to decrease the gain grating, similar to the work done by Schwartz, et al.[37] Since the lifetime is much larger the mechanical requirements would be much lower. This could be done with the Nd^{3+}:phosphate ring as well, but the vibration requirement would be similar to Nd^{3+}:YAG. Also, the gain is larger per unit length for Nd^{3+}:phosphate compared to Nd^{3+}:YAG. It is possible therefore to use a thinner gain medium which will be easier to vibrate and will minimise the gain grating.

Bibliography

[1] J. R. Wilkinson. Ring lasers. *Progress in quantum electronics*, 11:1–103, 1987.

[2] K. U. Schreiber, A. Velikoseltsev, M. Rothacher, T. Klügel, G. E. Stedman, and D. L. Wiltshire. Direct measurement of diurnal polar motion by ring laser gyroscopes. *Journal of Geophysical Research: Solid Earth*, 109(B6), 2004.

[3] A. V. Dotsenko, L. S. Kornienko, E. G. Kravtsov, N. Vladimirovich, E. G. Lariontsev, O. E. Naniĭ, and A. N. Shelaev. Use of a feedback loop for the stabilization of a beat regime in a solid-state ring laser. *Quantum Electronics*, 16:58–63, 1986.

[4] S. Schwartz, F. Gutty, G. Feugnet, É. Loil, and J-P. Pocholle. Solid-state ring laser gyro behaving like its helium-neon counterpart at low rotation rates. *Optics Letters*, 34(24):3884–3886, 2009.

[5] W. J. Kozlovsky, T. Y. Fan, and R. L. Byer. Diode pumped continous wave Nd: glass laser. *Optics Letters*, 11:120788, 1986.

[6] J. F. Philips, T. Tpfer, H. Ebendorff-Heidepriem, D. Ehrt, and R. Sauerbrey. Spectroscopic and lasing properties of Er-Yb doped fluoride phosphate glasses. *Applied Physics B*, 72:399–405, 2001.

[7] K. U. Schreiber and J-P. R. Wells. Invited review article: Large ring lasers for rotation sensing. *Review of Scientific Instruments*, 84(4):041101–041101, 2013.

[8] M. J. Weber. Science and technology of laser glass. *Journal of Non-Crystalline Solids*, 123:208–222, 1991.

[9] K. U. Schreiber, T. Klügel, J-P. R. Wells, R. B. Hurst, and A. Gebauer. How to detect the chandler and the annual wobble of the earth with a large ring laser gyroscope. *Physical Review Letters*, 107(17):173904, 2011.

[10] D. P. McLeod. *Seismic effects in ring lasers and transverse mode selection in helium-neon lasers.* PhD thesis, University of Canterbury, 2000.

[11] M. Faucheux, D. Fayoux, and J. J. Roland. The ring laser gyro. *J. Optics (Paris)*, 19:101–115, 1988.

[12] G. la Sagnac. *Comptes Rendus*, 157:708–710, 1913.

[13] W. M. Macek and D. T. M. Davies. Rotation sensing with travelling wave ring lasers. *Applied Physics Letters*, 2:67–68e, 1963.

[14] R. B. Hurst, G. E. Stedman, K. U. Schreiber, R. J. Thirkettle, R. D. Graham, N. Rabeendran, and J-P. R. Wells. Experiments with a 834 m2 ring laser interferometer. *Journal of Applied Physics*, 105:113–115, 2009.

[15] B. E. Cole. UV and plasma stable high-reflectance multilayer dielectric mirrors., June 13, 1990. EP Patent 0,372,438.

[16] K. U. Schreiber, T. Klügel, A. Velikoseltsev, W. Schlüter, G. E. Stedman, and J-P. R. Wells. The large ring laser G for continuous earth rotation monitoring. *Pure and Applied Geophysics*, 166(8-9):1485–1498, 2009.

[17] A. A. Michelson and H. G. Gale. The effect of the earth's rotation on the velocity of light, ii. *The Astrophysical Journal*, 61:140, 1925.

[18] V. Vali and R. W. Shorthill. Fiber ring interferometer. *Applied Optics*, 15(5):1099–1100, 1976.

[19] R. Bergh, H. Lefevre, and H. Shaw. An overview of fiber-optic gyroscopes. *Journal of Lightwave Technology*, 2(2):91–107, 1984.

[20] R. B. Hurst, J-P. R. Wells, and G. E. Stedman. An elementary proof of the geometrical dependence of the Sagnac effect. *Journal of Optics*, 9:838–841, 2007.

[21] W. W. Chow, J. Gea-Banacloche, L. M. Pedrotti, V. E. Sanders, W. Schleich, and M. O. Scully. The ring laser gyro. *Review of Modern Physics*, 57:61–104, 1985.

[22] F. Aronowitz. Fundamentals of the ring laser gyro. NATO Research and technology organization, 1999.

[23] A. E. Siegman. *Lasers*. University Science Books, 1986.

[24] F. Aronowitz. The laser gyro in laser applications. 1:133–200, 1971.

[25] T. Podgorski and F. Aronowitz. Langmuir flow effects in the laser gyro. *IEEE Journal of Quantum Electronics*, 4(1):11–18, 1968.

[26] K. U. Schreiber, M. Schneider, C. H. Rowe, G. E. Stedman, S. J. Cooper, W. Schlüter, and H. Seeger. The C-II ring laser project. *Physics and Chemistry of the Earth, Part A: Solid Earth and Geodesy*, 25(12):805–807, 2000.

[27] C. P. Wyss, D. N. Wright, B. T. King, D. P. McLeod, S. J. Copper, and G. E. Stedman. Collision broadening and quantum noise in a very large ring laser gyroscope. *Optics Communications*, 174:181–189, 2000.

[28] B. Ståhlberg, P. Jungner, and T. Fellman. Measurements of ^{22}Ne-^{20}Ne isotope shifts by laser-induced line narrowing in three-level systems. *Applied Spectroscopy*, 43(4):654–656, 1989.

[29] P. Walsh and G. Kemeny. Laser operation without spikes in a ruby ring. *Journal of Applied Physics*, 34:956, 1963.

[30] C. L. Tang, H. Statz, and G. DeMars. Spectral output and spiking behavior of solid-state lasers. *Journal of Applied Physics*, 34(8):2289–2295, 1963.

[31] E. L. Klochan, L. S. Kornienko, N. V. Kravtsov, E. G. Lariontsev, and A. N. Shelaev. Spectral characteristics of a YAG: Nd^{3+} solid-state continuous ring laser. *Radio Engineering and Electronic Physics.*, 19:58–64, 1974.

[32] E. L. Klochan, L. S. Kornienko, N. V. Kravtsov, E. G. Lariontsev, and A. N. Shelaev. Oscillation regimes in a rotating solid state ring laser. *Soviet Physics*, 38:669–673, 1974.

[33] N. Kravtsov, Y. Lariontsev, and A. Shelaev. Oscillation regimes of ring solid state lasers. *Laser Physics*, 3:22–62, 1993.

[34] S. Schwartz, G. Feugnet, P. Bouyer, E. Lariontsev, A. Aspect, and J-P. Pocholle. Mode-coupling control in resonant devices: application to solid-state ring lasers. *Physical Review Letters*, 97(9):093902, 2006.

[35] S. Schwarts, G. Feugne, E. Lariontsev, and P. Pocholle. Oscillation regimes of a solid-state ring laser with active beat-note stabilization: From a chaotic device to a ring-laser gyroscope. *Physics Review A*, 76:023807, 2007.

[36] T. Y. Fan and R. L. Byer. Diode laser-pumped solid-state lasers. *IEEE Journal of Quantum Electronics*, 24(6):895–912, 1988.

[37] S. Schwartz, F. Gutty, G. Feugnet, P. Bouyer, and J-P. Pocholle. Suppression of nonlinear interactions in resonant macroscopic quantum devices: The example of the solid-state ring laser gyroscope. *Physics Review Letters*, 100:183901, 2008.

[38] H. G. Danielmeyer and W. G. Nilsen. Spontaneous single-frequency output from a spatially homogeneous Nd: YAG laser. *Applied Physics Letters*, 16(3):124–126, 1970.

[39] H. Zeghlache, P. Mandel, N. B. Abraham, L. M. Hoffer, G. L. Lippi, and T. Mello. Bidirectional ring laser: Stability analysis and time dependent solutions. *Physics Review A*, 37:470–495, 1988.

[40] R. Adler. A study of locking phenomena in oscillators. *Proceedings of the IRE*, 34:351–357, 1946.

[41] L. N. Menegozzi and W. E. Lamb. Theory of a ring laser. *Physics Review A*, 8:4, 1971.

[42] G. E. Stedman. Ring-laser tests of fundamental physics and geophysics. *Reports on Progress in Physics*, 60:615–689, 1997.

[43] L. Ziyuan. *Optical Supercavity and Precision Ring Laser Measurement*. PhD thesis, University of Canterbury, 1993.

[44] Personal communication with R.B. Hurst.

[45] D.W. Allan. Time and frequency (time-domain) characterisation, estimation, and prediction of precision clocks and oscillators. *IEEE Journal of Quantum Electronics*, 6:647–650, 1987.

[46] W. Koechner. *Solid-State Laser Engineering*. Springer, 2006.

[47] E. Snitzer. Optical maser action of Nd $^{3+}$in a barium crown glass. *Physics Review letters*, 7:444–446, 1961.

[48] J. M. McMahon. Optimization of Nd:glass lasers with phosphate-laser glass. Technical report, Naval Research Lab, 1976.

[49] S. Kishida, K. Washio, S. Yoshikawa, and Y. Kato. CW oscillation in a Nd: phosphate glass laser. *Applied Physics Letters*, 34:273–275, 1979.

[50] J. M. Pellegrino, W. M. Yen, and M. J. Weber. Composition dependence of Nd^{3+} homogeneous iinewidths in glasseslase. *Journal of Applied Physics*, 51:6332–6336, 1980.

[51] T. Izumitani, H. Toratani, and H. Kuroda. Radiative and nonradiative properties of neodimium doped silicate and phosphate glasses. *Journal of Non-Crystalline Solids*, 47:87–100, 1982.

[52] V. B. Kravchenko and Yu. P. Rudnitskii. Phosphate glass (review). *Kvantovaya Elektron*, 6:661–689, 1979.

[53] J. E. Marion and M. J. Weber. Phosphate laser glasses. *European Journal of Solid State Inorganic Chemistry*, 28:271–287, 1991.

[54] W. J. Miniscalco. *Rare earth doped fiber lasers and amplifiers*. Marchel Dekker, 1993.

[55] H. Kogelnik and T. Li. Laser beam and resonator. *Applied Optics*, 5:1550–1567, 1966.

[56] W. G. Nilsen and H. G. Danielmeyer. Spontaneous single frequency output from a spatially homogeneous Nd: YAG laser. *Applied Physics Letters*, 16:124–126, 1970.

[57] S. Sunada, S. Tamura, K. Inagaki, and T. Harayama. Ring laser gyroscope without the lock in phenomenon. *Physics Review A*, 78:053822, 2008.

[58] W. Klische and C. O. Weiss. Instabilities and routes to chaos in a homogeneously broadened 1- and 2-mode ring laser. *Physical Review A*, 31:4049–4051, 1985.

[59] R. J. Mears and S. R. Baker. Erbium fibre amplifiers and lasers. *Optical and Quantum Electronics*, 24(5):517–538, 1992.

[60] P. A. Forrester and D. F. Sampson. A new laser line due to energy transfer from colour centers to erbium ions in CaF_2. *Proceedings of the Physical Society*, 88:199, 1966.

[61] V. P. Mikhailov, N. V. Kuleshov, A. A. Lagatsky, V. G. Shcherbitsky, E. Heumann, T. Jensen, A. Dienning, and G. Huber. Spectroscopy and cw laser emission at 1.54 μm from yb-codoped Er:$KY(WO_4)_2$. *CLEO/Europe Conference on Lasers and Electro-optics*, 0:259, 1996.

[62] S. Bjurshagen, P. Brynolfsson, V. Pasiskevicius, L. Parreu, M. C. Pujol, M. Pena, M. Aguilo, and F. Diaz. Crystal growth, spectroscopic characterization and eye-safe laser operation of erbium and ytterbium codoped $KLu(WO4)_2$. *Applied Optics*, 47:656–665, 2008.

[63] J. C. Souriau, R. Romero, Ch. Borel, C. Wyon, C. Li, and R. Moncorge. Comparative optical properties and cw laser performace around 1.56 μm of the (Yb^{3+},Er^{3+}) codoped Y_2SiO_2 and $SrY_4(SiO_4)_3O$ crystals. *De Physique*, 4:373–376, 1994.

[64] J. C. Souriau, R. Romero, C. Borel, C. Wyon, Li. C, and R. Moncorge. Room-tempeture diode-pumped continuous wave Y_2SiO_2 and $SrY_4(SiO_4)_3O$ crystal laser at 1554 nm,. *Applied Physics Letters*, 64:1189–1191, 1994.

[65] Wu. Ruiku, J. D. Myers, M. J. Myers, and R. F. Charles. Fluorescence lifetime and 980nm pump energy transfer dynamics in erbium and ytterbium co-doped phosphate laser glasses. In *High-Power Lasers and Applications*, pages 11–17. International Society for Optics and Photonics, 2003.

[66] X. Jun, S. Liangbi, Li. Hongjun, Z. Dan, H. Lui, and Z. Zhao. High quantum fluorescence yield of Er^{3+} at 1.5 nm in an Yb^{3+}, Ce^{3+} codoped CaF_2 crystal. *Optical Materials*, 29:932–935, 2006.

[67] C. B. Layne, W. H. Lowdermilk, and M. J. Weber. Multiphonon relaxation of rare-earth ions in oxide glasses. *Physics Review B*, 16:10–16, 1977.

[68] P. Laporta, S. Taccheo, S. Longhi, O. Svelto, and C. Svelto. Erbium ytterbium microlasers: optical properties and lasing characteristics. *Optical Materials*, 11:269–288, 1999.

[69] W. J. Miniscalco (Chapter 2). *Rare Earth Doped Fiber Lasers and Amplifiers*. CRC Press, 2001.

[70] A. Hutchinson and H. Allik. Diode array-pumped Er, Yb: Phosphate glass laser. *Applied Physics Letters*, 60:1424–1426, 1992.

[71] S. Jiang, S. J. Hamlin, J. D. Myers, and J. Lucas. High average power 1.54 μm Er^{3+}:Yb^{3+}-doped phosphate glass laser. *CLEO/Europe Conference on Lasers and Electro-optics*, 0:380–381, 1996.

[72] R. Van Leeuwen, B. Xu, L. S. Watkins, Q. Wang, and C. S. Ghosh. Low noise high power ultra-stable diode pumped Er-Yb phosphate glass laser. *Enabling phototonics technologies for defense, security and aerospace application iv (Proceeding of SPIE)*, 6975:69750k1–69750k8, 2008.

[73] S. Taccheo, P. Laporta, and C. Svelto. Widely tunable single-frequency erbium-ytterbium phosphate glass laser. *Applied Physics Letters*, 68:2621–2623, 1995.

[74] S. Taccheo, G. Sorbello, G. Laporta, P. Karlsson, and F. Laurell. 230-mw diode-pumped single frequency er:yb lasers at 1.5 μm. *IEEE Photonics Technology Letters*, 13:19–21, 2001.

[75] E. Tanguy, C. Larat, and P. J. Pocholle. Modelling of the erbium-ytterbium laser. *Optics Communications*, 153:172–183, 1998.

[76] W. J. Miniscalco and R. S. Quimby. General procedure for the analysis of Er^{3+} cross sections. *Optical Letters*, 16:256–260, 1991.

[77] A. P. Stephen, L. L. Chase, K. S Larry, L. K. Wayne, and F. K. William. Infrared cross-section measurements for crystals doped with Er^{3+}, Tm^{3+}, and Ho^{3+}. *IEEE Journal of Quantum Electronics*, 28:2619–2629, 1992.

[78] L. Zhuping, Q. Changhong, D. Shixun, J. Yasi, and Hu. Lili. Spectra and laser properties of Er^{3+}, Yb^{3+}:phosphate glasses. *Optical Materials*, 21:789–794, 2003.

[79] T. Y. Fan and A. Sanchez. Pump source requirements for end-pumped lasers. *IEEE Quantum Electronics*, 26:311–316, 1990.

[80] A. J. Alfrey. Modeling of longitudinally pumped cw Ti:sapphire laser oscillatiors. *IEEE Quantum Electronics*, 25:760–766, 1989.

[81] Intense HPD series 3100, datasheet, 2010.

[82] G. De. Geronimo, S. Taccheo, and P. Laporta. Opto-electronic feedback control for intensity noise suppression in a codoped erbium-ytterbium glass laser. *Electronic Letters*, 33:1336–1337, 1997.

[83] V. Danau, R. Polloni, C. A. Sacchi, and O. Svelto. On the decay time of regular spiking in a ruby laser. *Il Nuovo cimento*, 40:446–449, 1965.

[84] V. Daneu, C. A. Sacchi, and O. Svelto. On a ruby laser exhibiting regular spikes. *Il Nuovo cimento*, 36:1042–1044, 1965.

[85] R. Pratesi. Spiking emission from many-element lasers. *Applied Optics*, 6:1243–1253, 1967.

[86] R. Francini, F. Giovenale, U. M. Grassana, P. Laporta, and S. Taccheo. Spectroscopy of Er-Yb doped phosphate glasses. *Optical Materials*, 13:417–425, 2000.

[87] P. W. Smith. Linewidth and saturation parameters for the 6328-å transition in a He-Ne laser. *Journal of Applied Physics*, 37(5):2089–2093, 1966.

[88] W. R. Bennett Jr. The physics of gas lasers. *NASA STI/Recon Technical Report A*, 78:34450, 1977.

[89] R. B. Hurst, R. W. Dunn, K. U. Schreiber, R. J. Thirkettle, and G. K. MacDonald. Mode behaviour in ultralarge ring lasers. *Applied Optics*, 43:2337–2346, 2004.

Appendix A

Calculation of Gain Medium Parameters for Large Ring Laser

The following describes the method developed over a number of years in the ring laser group, for calculating gain curve parameters for He-Ne lasers. The calculation are performed using a spreadsheet.

The gain curve for He-Ne is composed of two isotopes. The He-Ne gas often contains equal amounts of ^{20}Ne and ^{22}Ne to decrease the mode competition. This is assumed for the rest of the calculations shown here, even thorough it can be extended to other isotope ratios. The spacing between the gain curve ^{20}Ne and ^{22}Ne is 890 MHz, the mean of the three most precisely reported value mentioned in [28]. The widths of ^{20}Ne and ^{22}Ne due to Doppler motion are 1440 MHz and 1510 MHz respectively, at 400 K with a scaling factor of $\mathrm{T}^{\frac{1}{2}}$, where T is temperature in Kelvin. The homogeneous contribution is shown in the Table A.1.

Homogeneous broadening	Temperature scaling factor	Temperature	FWHM (MHz)	Reference
Spontaneous emission	n/a	n/a	17	[87]
Ne-Ne collisions	T^{-1}	295 K	$70.5P_{Ne}$	[88]
He-Ne collisons	$T^{-\frac{2}{3}}$	295 K	$94.5P_{He}$	[88]

Table A.1: Lorentzian components of the homogeneous broadening for He-Ne gas. P_{Ne} and P_{He} are partial pressure of Neon and Helium in millibars.

The beam intensities I_1 and I_2 are normalized by the saturation intensity I_{sat} from [87] to give ρ_1 and ρ_2. ρ_o is the value below multi mode threshold defined in [89] to insure

single mode operation of the laser.

The frequency of oscillation of the beams is set by the cavity geometry (f_{opt}), with an intensity ρ_o for both beams. For each isotope of neon, gain (g) is calculated for each beam at f_{opt}, which takes into consideration hole burning. This procedure is performed using equations 30.4 -30.6 in Siegman [23], but with the modification that the saturation factor takes into account effects of saturation for each propagating beam. Total gain is calculated by adding the contribution of both isotopes. The gain is normalised by noting it is equal to loss in the cavity $(\tau f_L)^{-1}$, where τ is the ring-down time of the cavity. Finally the change of gain is calculated by varying ρ_1 and ρ_1 close to ρ_o. The gain saturation coefficients α and β used in the thesis are calculated from:

$$\alpha = \frac{\partial \ln g}{\partial \ln(1+\rho_1)}, \quad \beta = \frac{\partial \ln g}{\partial \ln(1+\rho_2)} \tag{A.1}$$

The dispersive effects are calculated using the same process of calculating gain (g), but the convolution of the Lorentzian components associated with homogeneous broadening, is replaced by the dispersion function associated with the same Lorentzian. The calculation uses a ring down time of 1 s for convenience in the spread sheet. (This requires the strength of the dispersion effect to be rescaled in the differential equations.) The dispersion coefficient ν in Chapter 3 is calculated using this process.